

Neutron scattering study of the 2D dipolar
magnet ErBr_3 and the 2D quantum spin liquid
system YbBr_3

Inauguraldissertation

zur
Erlangung der Würde eines Doktors der Philosophie
vorgelegt der
Philosophisch-Naturwissenschaftlichen Fakultät
der Universität Basel

von

Christian Wessler

2022

Genehmigt von der Philosophisch-Naturwissenschaftlichen Fakultät auf Antrag von

Prof. Dr. Michel Kenzelmann,
Prof. Dr. Christoph Bruder &
Prof. Dr. Martin Mourigal.

Basel, den 22.02.2022

Prof. Dr. Marcel Mayor, Dekan

Abstract

In recent years, a lot of effort was made to investigate materials with a honeycomb lattice, experimentally as well as theoretically. Both electronic and magnetic honeycomb systems are studied to explore their rich variety of phenomena. Graphene is a good example for an electronic system that possess Dirac fermions and exhibits topological effects like the quantum Hall effect. In particular, the topological properties of materials are regarded as promising to result in novel technological applications. Magnetic equivalents to graphene also show topological properties. Among the topological states are some of the elusive quantum spin liquids that are regarded to hold potential for building fault-tolerant quantum computers.

Here, I present the investigation of the two-dimensional van der Waals magnets ErBr_3 and YbBr_3 . The materials are isostructural and form an undistorted honeycomb lattice of magnetic ions. ErBr_3 is governed by dipolar interactions only and forms a continuously degenerate non-collinear ground-state with the spins restricted to the honeycomb plane. The ground-states correspond to specific spin structures what allows to reversibly manipulate the spin-wave dispersion between a magnetic phase with Dirac excitations and a phase with non-trivial valley Chern number. YbBr_3 , in contrast, is a collinear antiferromagnet with competing nearest and next-nearest neighbor interactions that remains only short-range correlated down to at least $T = 100$ mK. The spin-excitations show a broad continuum at the Brillouin zone boundary and are evidence for a quantum spin liquid phase near a quantum critical point. The results point towards fluctuations on the honeycomb plaquette as origin of the continuum.

Contents

1	Introduction	3
2	Neutron scattering	6
3	Motivation and theoretical background	11
4	Rare-earth trihalides ErBr_3 and YbBr_3	22
4.1	Crystal structure	22
4.2	Crystal electric field	24
4.3	Magnetic susceptibility	26
4.4	Dipolar interactions	28
4.5	Model Hamiltonian and the MF-RPA method	32
5	ErBr_3: a 2D dipolar model system	35
5.1	Magnetic structure of ErBr_3	38
5.2	Berezinsky–Kosterlitz–Thouless transition	39
5.3	Spin-waves in ErBr_3	46
5.4	Continuous degeneracy and Dirac cones	50
5.5	Topological magnetic excitations in ErBr_3	52
5.6	Discussion of the results in ErBr_3	54
5.7	ErBr_3 : Experimental details	56
6	YbBr_3: a 2D van der Waals system with partially disordered magnetic ground-state	57
6.1	Magnetic structure, diffuse scattering and correlation length	59
6.2	Inelastic neutron scattering and magnetic excitations	62
6.3	Parameters of the model Hamiltonian	64
6.4	Continuum of excitations and its distribution	67
6.5	Possible origins of the spin continuum	73
6.6	Discussion of YbBr_3	76
6.7	Outlook	79
6.8	YbBr_3 : Experimental details	82
7	Appendix	83
7.1	Instruments	83
7.2	Ewalds’s summation	87
7.3	Efficient formula for the calculation of the dipolar interactions	88
7.4	Linear spin-wave theory	91
7.5	Berry phase, Berry curvature and Chern number: relation and calculation	94
8	Acknowledgments	96
9	Bibliography	97

1 Introduction

Magnetism is an everyday-life phenomena. We encounter it everywhere, often without being aware that it is there. From simple uses like fridge magnets, door locks and toys to more complex applications like speakers, credit cards or data storages in smartphones, magnetism has become an essential part of modern society.

Naturally occurring ferromagnetism is known since the antique in the form of lodestone that was called “magnet” by the ancient Greeks [1]. Systematic research on magnetism began in the late 16th century when it was discovered that the earth itself is a magnet [2]. Two hundred years later, experiments and theoretical descriptions increased the understanding of magnetic fields by leaps and bounds. A relationship between electricity and magnetism was first found by H.C. Oersted who discovered that a compass is influenced by the proximity of a current running through a wire [3]. This observation was key to studying magnetic fields as it implies that one can create magnetic fields without the use of permanent magnets. Unsurprisingly, the following decades are full of new discoveries and ways to apply magnetism and electricity. Prominent works by A.M. Ampere [4] and M. Faraday [5] show the influence of magnetic and electric fields on one another leading to the J.C Maxwell’s theory of electromagnetism formulated in 1865 [6]. Electromagnetism describes electric and magnetic fields as aspects of the a single electromagnetic, field. However, magnetism is more than just the magnetic fields and also entails condensed matter phenomena that are not included in this theory. For example, what makes a material a ferromagnet? The answer was first given by P. Weiss in 1907 who introduced the theory of molecular fields which states that the spontaneous magnetization of magnets is due to an internal molecular field that is proportional to the average magnetization and causes the spontaneous alignment in magnets [7]. The theory is derived from phenomenological observations but can explain ordering temperatures. In ferromagnets, P. Curie observed that there is a critical temperature where magnetism suddenly vanishes [8]. A similar discovery was made by L. Néel for a different type of magnet, the antiferromagnet [9]. Although the calculated critical temperature is correct, the necessary molecular field is huge, on the order of thousands of Teslas, for ferromagnets [10]. Modern quantum mechanics present a theoretical foundation for the molecular field theory that explains the strong internal fields using the exchange interactions between ions. In particular, the Ising [11] and Heisenberg [12] model played an important role in the development of the modern understanding of magnetism which is based on the motions and interactions of electrons in atoms and to a smaller extent the nucleus itself.

In this description, magnetism is a quantum effect that originates from the motion

of the electrons in atoms that move in an orbit around the nucleus and around its own axis. The former is known as orbital angular momentum and the later is an intrinsic angular momentum called spin, together they form the magnetic moment of the atom [10]. Modern models work with the electron spins to explain the different types of magnetism and their phenomena. The phenomenological model of an internal molecular field is theoretically understood through the exchange interactions between neighboring ions in the frame of the quantum mechanical Heisenberg model [10]. This view allows for a better microscopic understanding of both a magnet's origin and its behavior

In general, one distinguishes between five types of magnetism: ferromagnetism, antiferromagnetism, ferrimagnetism, paramagnetism and diamagnetism. The first three types are ordered states where the spins are correlated and form a magnetic structure. Ferromagnetism refers to a magnetic state where the spins orderly point in the same direction and give the magnet a non-zero net magnetization. This is the magnetism found in permanent magnets. In contrast, there is no net magnetization in antiferromagnets. The spins are also neatly ordered but with alternating orientation between neighboring spins so that the magnetic moments cancel each other. Ferrimagnetism shares similarities with both ferromagnetism and antiferromagnetism. It has a non-zero net magnetization but the spins are not only oriented in the same direction. Like antiferromagnets, there are spins that point in the opposite direction but with a smaller moment, leaving a net magnetization. Paramagnetism and diamagnetism do not have an ordered magnetic structure but randomly distributed spins. Paramagnets do order in a magnetic field to a small degree since it is energetically favorable for the spins to align with the external magnetic field. The opposite behavior is found in diamagnets that repel external magnetic fields. The fields induce small currents that create fields with opposite polarization to the external magnetic fields and thereby reduce its strength. An excellent example for diamagnetism are superconductors. Currents flow without resistance in such materials, hence the induced currents are not diminished by electric resistance. And as a consequence, superconductors completely repel the external fields and exhibit perfect diamagnetism [13].

Many modern technological applications are related to magnetism and its related phenomena. One classic example is the Hall effect [27]. The current in a conductor is deflected by an external magnetic field and creates a voltage orthogonal to the current and field direction. Hall probes are used to measure the strength of magnetic fields but are also applied as position and motion sensors by detecting the movements of permanent magnets. However, there is also the quantum Hall effect that cannot be understood in a classical way and is solely a quantum mechanic phenomenon. Instead of a linear increase, plateaus appear in the Hall conductance at low

temperatures. The plateaus are a manifestation of the quantization of the conductance [15]. The effect is used in the definition of the electric resistance since it only depends on natural constants. This example illustrates that studying magnetism in condensed matter physics not only broadens our understanding of fundamental physics but also holds potential for technical applications.

A key to understand the energetic properties of magnetic systems are their magnetic excitations that are called spin waves. Spin waves are the collective precession of the spins around their magnetic ordering axis where the precession propagates through the magnetic system. One can also regard the spin waves as quasiparticles, called magnons, that move through the magnetic lattice. It is possible to derive the relevant exchange interactions from the spin waves in the material and compare them to theoretical models. Establishing models of magnetic systems allow us to understand the microscopic behavior and to make predictions about other similar materials. The next section describes a selection of interesting and possible technologically relevant phenomena focusing on magnetism in two-dimensional systems.

2 Neutron scattering

One large topic in solid state physics is the study of magnetism in all of its complex variations. The tool of choice to investigate these microscopic phenomena is often neutron scattering. Neutrons have favorable properties that make them excellent probes for not only magnetic but also atomic structures. Neutrons are created either in a reactor by nuclear fission or in a spallation source by hitting an appropriate target with protons. The neutron velocity is high directly after their creation and unsuited for neutron experiments. A moderator reduces the velocity of the neutrons by letting them collide with its nuclei until the neutrons reach thermal equilibrium with the moderator. In equilibrium, the velocities of the neutrons follow a Maxwell distribution what provides a certain velocity range that can be used for experiments. Typical moderators are heavy water and hot graphite to create cold ($E_{cold} = 0.1 - 10$ meV), thermal ($E_{therm} = 5 - 100$ meV) and hot ($E_{hot} = 100 - 500$ meV) neutrons [16]. It is common to refer to neutrons by their velocity, wave vector or energy depending on the situation by using the relations $E = \frac{mv^2}{2} = \frac{(2\pi)^2\hbar^2}{2m\lambda^2} = \frac{\hbar^2k^2}{2m}$ (E : neutron energy, m : neutron mass, v : neutron velocity, λ : neutron de Broglie wavelength, \hbar : reduced Planck-constant and \vec{k} neutron wave vector).

The de Broglie wavelength of neutrons is of similar order as the interatomic distance of solids and crystals and so neutrons are subjected to interference effects that provide information about the structure of the scattering system. The velocity dependence of the de Broglie wavelength allows to select neutrons with an appropriate wavelengths for different experiments [16].

To study the bulk of samples, it is necessary to penetrate deep into the material. The uncharged neutrons do not face a Coulomb barrier and are capable to enter deeply into matter. Hence, neutron scattering results from the nuclei of the atoms or more precisely the nuclear forces between neutron and nuclei [16]. If the energy of a neutron is similar to the excitation energy of a system, then there is a significant change in the energy of the neutron when an excitation is created or annihilated. This is the case for moderated neutrons and their change in energy is measurable which allows to investigate excitations [16]. In regard to magnetic systems, it is essential to remember that neutrons have a magnetic moment or spin. The neutron spin can interact with the unpaired electrons of magnetic atoms. From these interactions, it is possible to deduce the arrangement of the spins but also measure time-dependent spin correlations of the scattering system [16].

Summarized, neutrons provide an excellent tool to investigate matter since they have appropriate wavelengths as well as energies, interact with magnetic moments and are able to penetrate matter deeply.

Neutron scattering experiments make use of the momentum and energy conservation of the neutrons. Let us assume that the change in momentum of a scattered neutron is $\Delta\vec{p}$ and expressed in terms of the wave vector, then the conservation laws follow as $\Delta\vec{p}/\hbar = \vec{k}_i - \vec{k}_f = \vec{Q}$ and $\Delta E = \frac{\hbar^2}{2m}(k_i^2 - k_f^2) = E$. The change in momentum and energy are represented by the scattering vector \vec{Q} and energy transfer E , respectively.

Expressing the two conservation laws in terms of wavevectors provides a natural coordinate system for neutron scattering, the reciprocal space. The three vectors \vec{k}_i , \vec{k}_f and \vec{Q} form the scattering triangle in reciprocal space as shown in Fig. 1. With the definition of the scattering triangle and reciprocal space, one can introduce the Bragg's law in neutron scattering. Consider that $\vec{\tau} = ha^* + kb^* + lc^*$ (h, k, l are integers) is a reciprocal lattice vector connecting two ions in reciprocal space and $|\vec{k}_i| = |\vec{k}_f| = k$. Then the scattering triangle is isosceles with the angle θ between the two vectors of equal length (see Fig. 1a). The scattering vector is chosen to be equal to a reciprocal lattice vector with length $|\vec{\tau}| = 2k \sin(\frac{1}{2}\theta)$ (see Fig. 1b). There is always a crystal plane orthogonal to $\vec{\tau}$ because of the periodicity of the crystal and its length can be expressed as $|\vec{\tau}| = n\frac{2\pi}{d}$ where d is the spacing between crystal planes. Bragg's law $n\lambda = 2d \sin(\frac{1}{2}\theta)$ follows by combining the equations and expressing the wave vector through the wavelength. This also means that Bragg diffraction happens without energy transfer and the scattering is from the whole crystal [16].

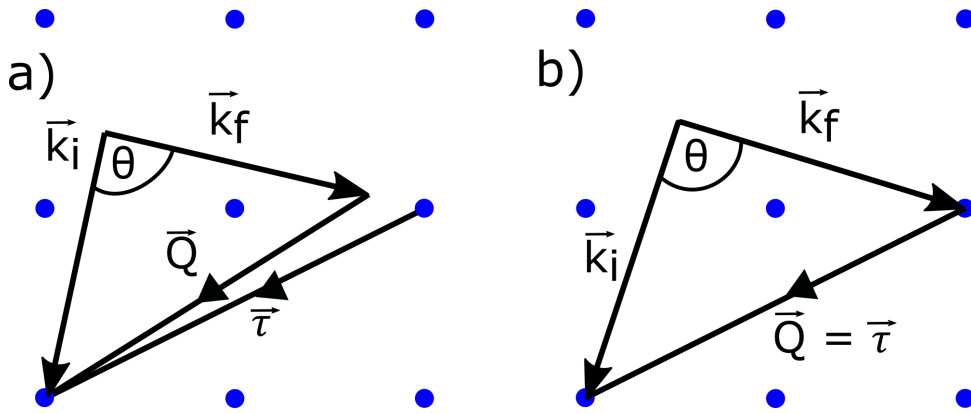


Fig. 1 | Illustration of the scattering triangle and Bragg's law. The scattering triangle is shown with **a**, $\vec{Q} \neq \vec{\tau}$: the Bragg condition is not fulfilled; **b**, $\vec{Q} = \vec{\tau}$: Bragg scattering occurs.

The (first) Brillouin zone is defined as all points closer to the origin of the lattice than to all other points. The importance of the BZ is derived from Bloch's theorem which states that the behavior of waves is the same in all BZs due to the periodicity of the crystal [17]. Additionally, it is a practical way to define and understand high-symmetry points of the crystal. The reciprocal lattice can be split into BZs that cover

the whole lattice without gaps, what is referred to as extended BZ. Similarly, the real space lattice can be represented by Wigner-Seitz cells in a similar fashion.

To do neutron experiments, it is necessary to orientate the crystal in reciprocal space so that the scattering vector correctly coincides with the corresponding points of the crystal lattice. The crystal orientation is done by finding and identifying nuclear Bragg peaks and determining the orientation of the crystal in space. Then the crystal plane that one wants to study is matched to the plane of the scattering triangle, called scattering plane. Typically, the scattering plane is horizontal matching the experimental instrumentation. The last step is to rotate the crystal to match the Bragg peaks to the scattering vector. What is measured in a neutron scattering experiment is the partial differential cross-section (pdCS)

$$\frac{d^2\sigma}{d\Omega dE'} = \frac{\# \text{ scattered neutron into } d\Omega \text{ with final energy } E'}{\Phi d\Omega dE'}$$

where $d\Omega$ is a small solid angle, E' is the energy range $E + dE$ and Φ is the flux of the incident neutrons..

Hence, it is necessary to interpret the measured pdCS with a theoretical model for the scattering. The master formula for neutron scattering that describes the pdCS which is given by [18]

$$\left(\frac{d^2\sigma}{d\Omega dE'}\right)_{\vec{k}_i \rightarrow \vec{k}_f} = \frac{1}{N} \frac{k_f}{k_i} \left(\frac{m}{2\pi\hbar^2}\right)^2 \sum_{\lambda_0 \sigma_0} \rho_{\lambda_0} \rho_{\sigma_0} \cdot \sum_{\lambda_f \sigma_f} |\langle \vec{k}_f \sigma_f \lambda_f | V | \vec{k}_0 \sigma_0 \lambda_0 \rangle|^2 \delta(E + E_{\lambda_0} - E_{\lambda_f})$$

where N is the number of neutrons, m the neutron mass. λ is the state of the sample and σ is the polarization state. i and f indicate the states before and after the scattering event and the subscript 0 indicates the average over initial states. ρ is the probability of states to occur and V is the interaction potential between the sample and neutrons. The master formula is quite general and does not make assumptions about the potential V [18]. The transitions between the initial and final states are described by Fermi's golden rule

$$W_{\vec{k}_i, \lambda_i, \sigma_i \rightarrow \vec{k}_f, \lambda_f, \sigma_f} = \frac{2\pi}{\hbar} \rho_{\vec{k}_f \sigma_f(E_f)} |\langle \vec{k}_f \lambda_f \sigma_f | V | \vec{k}_i \lambda_i \sigma_i \rangle|^2.$$

The nuclear scattering pdCS follows then as

$$\begin{aligned} \left(\frac{d^2\sigma}{d\Omega dE'}\right)_{coh} &= \frac{\sigma_{coh} k_f}{4\pi k_i} \frac{1}{2\pi\hbar} \sum_{jj'} \int_{-\infty}^{\infty} \langle e^{-i\vec{\kappa}\cdot\vec{R}_{j'}(0)} e^{i\vec{\kappa}\cdot\vec{R}_j(t)} \rangle e^{-iEt} dt \\ \left(\frac{d^2\sigma}{d\Omega dE'}\right)_{inc} &= \frac{\sigma_{inc} k_f}{4\pi k_i} \frac{1}{2\pi\hbar} \sum_j \int_{-\infty}^{\infty} \langle e^{-i\vec{\kappa}\cdot\vec{R}_j(0)} e^{i\vec{\kappa}\cdot\vec{R}_j(t)} \rangle e^{-iEt} dt \end{aligned}$$

where $\vec{\kappa} = \vec{k}_i - \vec{k}_f$ and $\vec{R}_j(t)$ is the time-dependent Heisenberg operator to the position vector \vec{R}_j pointing to the j -th ion. $\sigma_{coh} = 4\pi(\bar{b})^2$ and $\sigma_{inc} = 4\pi\{\bar{b}^2 - (\bar{b})^2\}$ with the nucleus-dependent scattering length b . $(\bar{b})^2$ is the average over uncorrelated nuclei if $j \neq j'$ and \bar{b}^2 is the average if $j = j'$. The average allows to consider different isotopes of the nuclei that may scatter the neutrons differently. The scattering length determines how strongly a neutron is scattered or absorbed by a nucleus. σ_{coh} represents the coherent scattering, σ_{inc} the incoherent scattering and only the former includes interference effects. This means that the coherent scattering contains information about the collective excitations of the system.

In contrast to the nuclear scattering, the magnetic scattering depends on the spin of the ions and their polarization. The elastic contribution of the magnetic scattering is given by

$$\left(\frac{d\sigma}{d\Omega}\right)_{el} = \frac{2\pi^3}{Nv_0} \sum_{\vec{\tau}} \delta(\vec{\kappa} - \vec{\tau}) |\vec{\kappa} \times \{\langle F(\vec{\kappa}) \rangle \times \hat{\kappa}\}|^2$$

where $\vec{\tau}$ is the reciprocal lattice vector of the magnetic structure with the magnetic ordering vector \vec{Q}_0 . $\hat{\kappa} = \vec{\kappa}/|\vec{\kappa}|$ is the unit scattering vector.

$F(\vec{\kappa}) = \gamma r_0 \sum_d f_d(\vec{\kappa}) \langle \vec{S}_d \rangle e^{i\vec{\kappa}\cdot\vec{r}_d} e^{-W_d(\vec{\kappa})}$ is the magnetic structure factor where the sum runs over the d different magnetic ions. γ is the gyromagnetic ratio, r_0 the classical electron radius. $f(\vec{\kappa}) = \int \rho(\vec{r}) e^{i\vec{\kappa}\cdot\vec{r}} d^3r$ is the atomic form factor and $\rho(\vec{r})$ the magnetic electron density of the ion. $\langle \vec{S}_d \rangle$ is the spin expectation value of the magnetic moment of ion d . Often, one is interested in the neutron scattering with energy transfer, the inelastic neutron scattering (INS). Both single particle excitations (e.g. from the CEF) and collective excitations like spin-waves contribute to the INS. The magnetic partial differential cross-section for a crystalline solid with long-range order [18] is expressed by

$$\begin{aligned} \frac{d^2\sigma}{d\Omega dE'} &= \frac{(\gamma r_0)^2 k_f}{4\pi\mu_B^2 k_i} e^{-2W(\vec{\kappa})} (1 - e^{-E/(k_B T)})^{-1} \\ &\quad \sum_{\alpha,\beta=x,y,z} \{\delta_{\alpha\beta} - \hat{\kappa}_\alpha \hat{\kappa}_\beta\} \Im \chi_{\alpha\beta}(\vec{\kappa}, E) \end{aligned}$$

where μ_B is the Bohr magneton and $W(\vec{\kappa})$ is the Debye-Waller factor that includes the attenuation caused by the thermal motion of the atoms. $\{\delta_{\alpha\beta} - \hat{\kappa}_\alpha \hat{\kappa}_\beta\}$ are the polarization factors. $\bar{\chi}(\vec{\kappa}, E)$ is the generalized susceptibility given by

$$\chi_{\alpha\beta}(\vec{\kappa}, E) = \pi \mu_B^2 |f(\vec{\kappa})|^2 (1 - e^{-E/(k_B T)})^{-1} \sum_l e^{i\vec{\kappa} \cdot \vec{r}_l} \frac{1}{2\pi\hbar} \int_{-\infty}^{\infty} \langle S_{0,\alpha}(0) S_{l,\beta}(t) \rangle e^{-iEt/\hbar} dt$$

$\langle S_{0,\alpha}(0) S_{l,\beta}(t) \rangle$ is the expectation value of the time-dependent spin-operators that contain the information about the correlations.

3 Motivation and theoretical background

In 2004, Novoselov and Geim discovered the 2D material graphene [19, 20]. The revolutionary part about this discovery is that they succeeded in separating a monolayer of graphene without the need for supporting structures. Free-standing monolayers were assumed to be unstable and to naturally form curved structures like nanotubes [21]. Surprisingly, it is a simple idea that allows to obtain a monolayer of graphene even if the actual implementation is difficult. In principal, one can picture that bulk graphite is repeatedly peeled with adhesive tape to separate increasingly thinner flakes of graphene in a process called micromechanical cleaving [21]. But it is difficult to find the separated monolayer flakes of graphene. The graphene flakes of different thickness are randomly distributed atop a huge area, typically 1 cm², and cannot be identified efficiently with modern techniques to study atomically thin materials [21]. Only by chance would it be possible to find a piece of graphene between the numerous thicker flakes. However, there is an additional trick required that helps to find the separated monolayer flakes. But it was noticed that an optical microscope can observe graphene if it is placed on top of a SiO₂ wafer of an appropriate thickness due to a slight optical contrast to the empty wafer [21]. From this point onward, the search of other 2D materials began with quite a lot of success. Furthermore, there is more to graphene than just its two-dimensionality. Rich physics were found in graphene that motivated a lot of research work on two-dimensional materials.

A selection of intriguing aspects of graphene is presented here to convey an impression of the impact of the discovery of graphene. Condensed matter physics is, in general, described in terms of the Schrödinger equation but this is not the case for graphene. Here, the Hamiltonian (Eq. 1) is Dirac-like to accommodate the physics of the electrons

$$\mathcal{H}_{Dirac} = \hbar v_F \bar{\sigma} \cdot \vec{k} \quad (1)$$

where v_F is the Fermi-velocity that plays the role of the speed of light and $\bar{\sigma}$ is the two-dimensional Pauli matrix [21]. In 1933, Schrödinger and Dirac received the Nobel prize for their contributions to quantum theory [23].

Schrödinger assumed that matter could be described as both particles and waves. Based on this assumption, he formulated the Schrödinger equation that allows to adequately calculate the energy levels of electrons in atoms. Dirac unified quantum theory with special relativity [24] that describes the relationship between time and space [25]. The Dirac equation considers a fully relativistic quantum theory. A material described by the Dirac equation, like graphene, can feature Dirac fermions. This type of quasiparticle (collective excitations that can be described as particles)

corresponds to electrons without mass (or equivalently, neutrinos that gained the electric charge e) and obey the Fermi-Dirac statistic [21]. The Dirac nature of these quasiparticles leads to relativistic electron waves in the honeycomb lattice and provides a means to study quantum relativistic phenomena in a material. Hence, quantum electrodynamics can be studied without the need for high-energy physics equipment by probing the electronic properties of graphene [21]. The hallmark of the Dirac physics in the electronic bands of graphene is the Dirac cone that is formed by the crossing of two bands and has a linear dispersion close to the crossing point.

Graphene also shows a peculiar zero-field conductivity that does not go to zero even in the limit of vanishing charge carriers. The conductivity retains a value similar to the conductivity quantum e^2/h [21] where conductivity quantum refers to the smallest value of the quantized conductivity. In general, one would expect that such a conductivity leads to a metal-insulator transition but this is not observed in graphene down to liquid-helium temperature.

Furthermore, graphene exhibits the famous quantum Hall effect (QHE) for which discovery von Klitzing was awarded the Nobel prize in 1985 [26]. The classical Hall effect is the appearance of a voltage difference in an electrical conductor under a static magnetic field with a current running through the conductor [27] as shown in Fig. 2a. Voltage, current and magnetic field are perpendicular to each other. In other words, the charge carriers are deflected transverse from the path of the current by the magnetic field via the Lorentz force. QHE refers to the quantum mechanical equivalent to the classical Hall effect where the Hall conductance is quantized in levels of multiples of e^2/h (see Fig. 2b).

The quantization can be understood in several ways. One possibility is to regard it as the result from the discrete Landau levels that correspond to the quantized cyclotron orbits of charged particles in an uniform magnetic field [28]. Another way is to use topological considerations. Mathematically, topology refers to the study of geometric objects that can be continuously transformed into each other without tearing or making holes. For example, a mug with handle can be continuously transformed into a torus in contrast to a sphere as shown in Fig. 3. One needs to make a hole in the sphere to create the handle of the mug and this cannot be done with a continuous transformation. In condensed matter, the Hamiltonians of quantum systems are called topologically equivalent if they can be continuously transformed into each other. Topological systems are classified by their integer Chern number. A system is topologically trivial if the Chern number is zero and different topological phases are distinguished by their respective Chern numbers. The Chern number is a topological invariant that does not change under continuous deformations. This means that a topological phase with a non-zero Chern number is protected against external

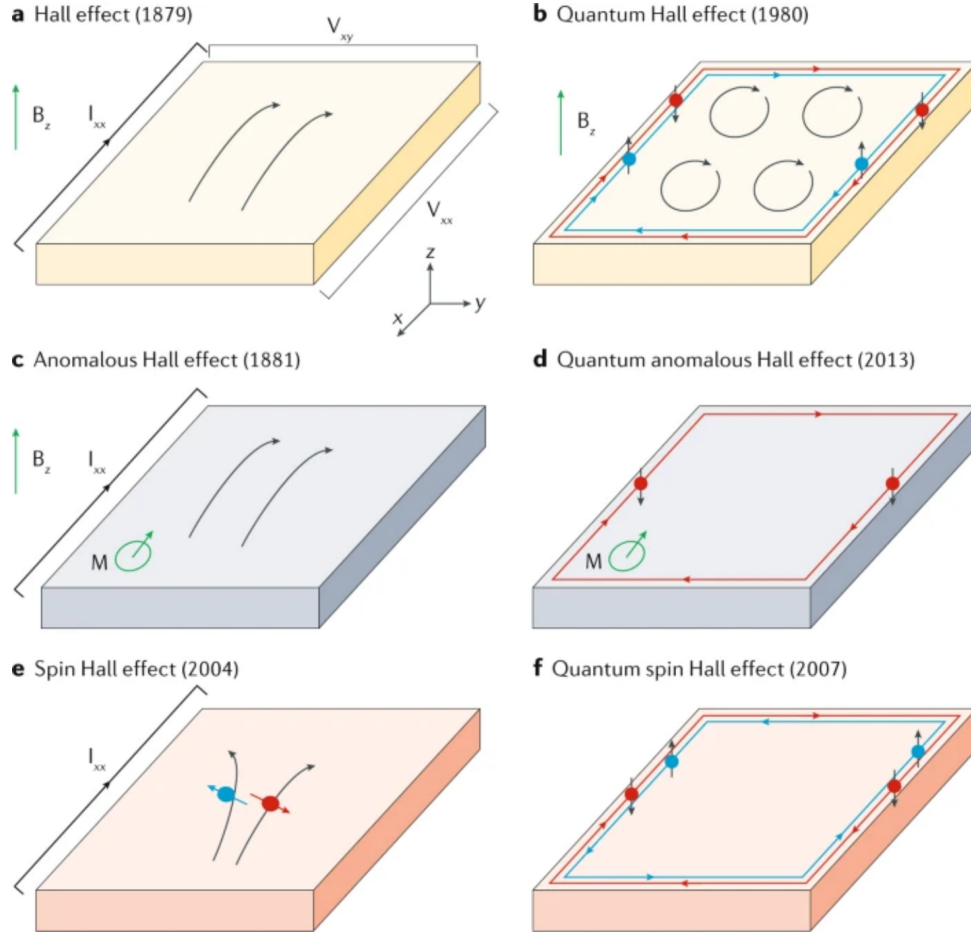


Fig. 2 | Schematics of the classical and quantum Hall effects. **a**, classical Hall effect; **b**, quantum Hall effect; **c**, anomalous Hall effect; **d**, quantum anomalous Hall effect; **e**, spin Hall effect; **f**, quantum spin Hall effect. The Figure was taken from Ref. [40].

perturbations. It changes only if the perturbation is large enough to push the system into another topological phase with a different Chern number. The Chern number C is defined as the integral of the Berry curvature $\vec{\Omega}(\vec{k})$ over the whole Brillouin zone divided by 2π

$$C = -\frac{1}{2\pi} \int_{BZ} \vec{\Omega}(\vec{k}) dS = -\frac{1}{2\pi} \int_{BZ} \vec{\partial} \times \vec{A}(\vec{k}) dS$$

where $\vec{A}(\vec{k}) \equiv \langle \Psi(\vec{k}) | \partial_{\vec{k}} \Psi(\vec{k}) \rangle$ is the Berry connection and $|\Psi(\vec{k})\rangle$ is the state of the system at \vec{k} [29, 30]. The Berry connection also allows to calculate the Berry phase that is picked up by the wave function during the adiabatic movement along a closed path C in momentum space \vec{k}

$$\gamma = i \oint_C \vec{A}(\vec{k}) d\vec{k}.$$

The QHE is linked to topology by the Berry curvature that reproduces the Hall conductance by multiplying it with $h/2\pi$ [31]. The average Hall conductance was shown to be a topological invariant, a Chern number [32]. Hence, each plateau corresponds to a Chern number and the transition between plateaus means to change the Chern number as illustrated in Fig. 3.

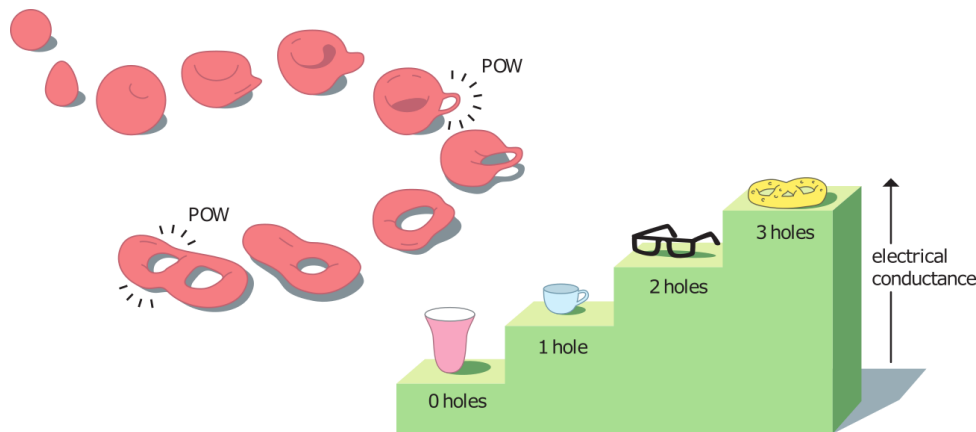


Illustration: ©Johan Jarnestad/The Royal Swedish Academy of Sciences

Fig. 3 | Illustration of topology and its relation to the QHE. The left side shows the transformation of a sphere to a mug and beyond. The transformation is continuous until holes need to be made (“POW”) and the Chern number changes. The right side presents the step-wise evolution of the Hall conductance related to different Chern numbers. The Figure was taken from Ref. [33]; © Johan Jarnestad/The Royal Swedish Academy of Sciences.

Experimentally, the so-called half-integer QHE is observed in graphene that has a shift of $1/2$ in the conductance levels with respect to the integer QHE [35] where the levels appear at integer multiples of e^2/h . The shift of the half-integer QHE is caused by the additional phase shift gained through the Berry phase in graphene [21]. Ultraclean, suspended graphene samples exhibit the fractional quantum Hall effect (FQHE) [36]. Here, the conductance levels are not separated by integer values of e^2/h but, as the name implies, fractions of it. Laughlin, Störmer and Tsui were awarded the Nobel prize for their discovery of this new form of quantum fluid with fractionally charged excitations [37]. Systems that exhibit quantum effects on a macroscopic range are called quantum liquids. Another example for quantum liquid systems are superconductors [38]. In the fractional quantum Hall state, electrons form composite quasiparticles with the magnetic flux quanta under application of a magnetic field. The quasiparticles are bosons that carry a fraction of the full charge e [37].

A technologically interesting phenomena in quantum Hall states is the existence of edge states without dissipation (see Fig. 2b, d, f) [39, 40]. The edge states are a result of the electrons that bounce off the edges and form skipping orbits in contrast to electrons in the bulk of the system that form closed cyclotron orbits [40]. Con-

sequently, the center of the two-dimensional material is insulating since there is no charge transport through the bulk. Only the edges are conducting in the QHE state. An important detail is that the edge states of the QHE exist even if there is no applied field [40].

Another type of QHE, the quantum spin Hall effect (QSHE), carries spin-polarized edge currents where spins of opposite polarization move in opposite directions. Enhancement of the spin-orbit coupling of graphene leads to the presence of the QSHE (see Fig. 2f) [39, 41, 42]. Both properties, no dissipation and spin-polarization, are interesting for technological applications in the spintronics [43] that use not only electric currents but also the electron spins to carry information.

An interesting question is whether there is a magnetic equivalent to graphene [44]. Indeed, there are materials that form honeycomb layers out of magnetic ions [45]. Graphene is a van der Waals material where the monolayers are stacked atop of each other and held together only by the van der Waals force. Therefore, it is a straightforward idea to look for similar magnetic materials. Such magnetic van der Waals systems not only have a honeycomb structure formed by their magnetic ions but also show a number of similar phenomena as observed in graphene. For example, a 2D honeycomb ferromagnet shows Dirac cones in its spin-wave dispersion [46]. More general, Dirac excitations can be present in 2D honeycomb lattices with non-interacting particles independent of their nature, fermionic or bosonic [45]. Bosonic Dirac excitations or Dirac magnons are massless like their fermionic counter parts but do not follow the Pauli-exclusion principle.

Among the magnetic Dirac materials are CoTiO_3 [47] and CrCl_3 [48]. CoTiO_3 is described by dominant nearest-neighbor XY ferromagnetic exchange and antiferromagnetic interlayer second-neighbor exchange with a strong easy-plane anisotropy [47]. There are Dirac cones observed in the spin-wave excitations as shown in Fig. 4. This system is a good example for a three-dimensional quantum XY magnet to study interacting Dirac magnons. Dirac cones are also found in CrCl_3 that has a similar magnetic structure to CoTiO_3 . The intralayer coupling is ferromagnetic and the interlayer coupling antiferromagnetic but with a relatively weaker interlayer coupling and easy-plane anisotropy compared to CoTiO_3 . Therefore, CrCl_3 is a quasi-two-dimensional ferromagnet with massless Dirac magnons [48]. In CrBr_3 , the observed magnon spectrum was not well understood for decades but could be explained with interacting Dirac magnons [45]. The two-dimensional honeycomb ferromagnet is also predicted to exhibit the magnonic quantum Hall effect [49]. Spin-waves replace the electrons in this case and an applied magnetic field creates a transverse Hall current of magnons as shown in Fig. 5. Spin-orbit coupling can induce the quantization of the Hall conductance together with the formation of Landau levels and the

cyclotron motion of the magnons. Otherwise, an extrinsic electric field gradient can also induce the quantization.

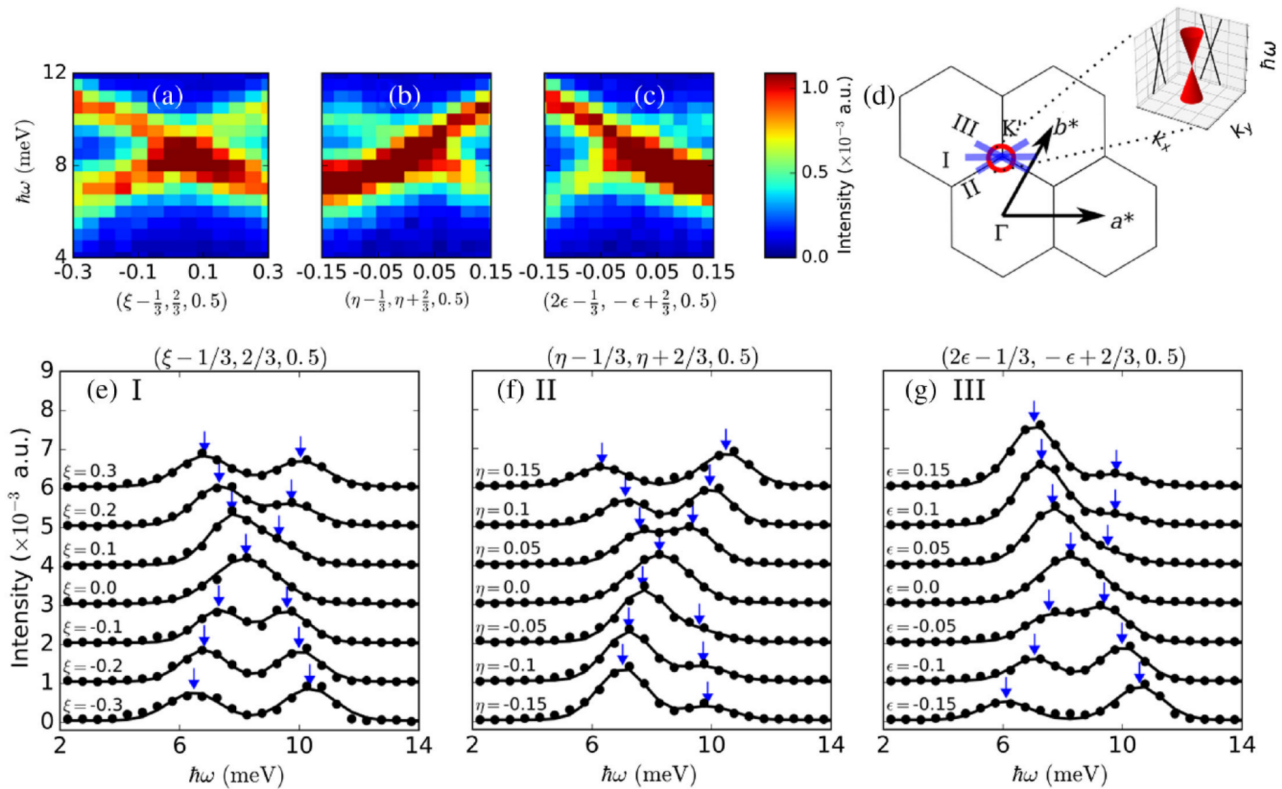


Fig. 4 | Magnon spectrum around a Dirac cone. **a-c** present different cuts through the Dirac cone at $(-1/3, 2/3, 1/2)$ as shown in **d**. **e-g** present the measured intensity versus energy at fixed momentum extracted from **a-c**, respectively. The Figure was taken from Ref. [47].

Similarly, the magnonic equivalent to the QSHE is predicted to exist in the honeycomb antiferromagnetic with spin-orbit coupling [50]. The Dzyaloshinskii-Moriya interactions can act as the spin-orbit coupling and can induce the quantization in the magnon Hall effect [49, 50]. Edge states are expected for the magnonic equivalents to the different QHE [49, 50] and hold similar potential for technological applications to their electronic counterparts. There are approaches to build devices that use transport of spin-waves, the so-called magnonics technology, to replace electronic devices [51].

The fractional quantum Hall state is proposed to have an interesting magnetic equivalent. It is suggested that it corresponds to the concept of the resonating valence bonds [52]. Anderson proposed the resonating valence bond state as the ground-state of the triangular lattice [53]. To picture this state, one can first think of pairs of entangled spins, or so-called valence bonds, that cover the whole lattice with an arbitrary pairing between neighboring spins. The resonating valence bond state follows as the superposition of many different pairings of entangled spins as shown in

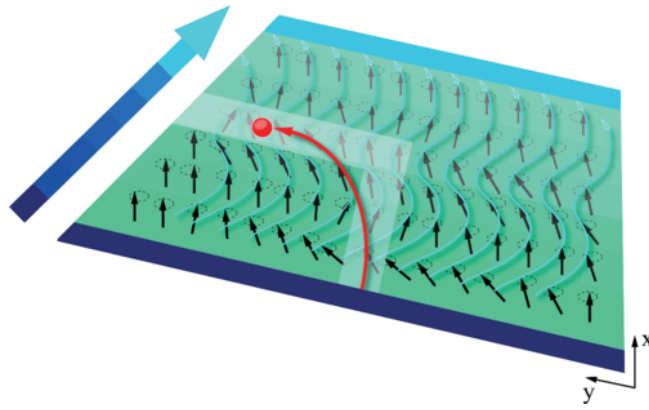


Fig. 5 | Schematics of the magnetic quantum Hall effects. A magnetic field along the x direction creates a transverse magnon Hall current (red dot) along the x direction. The quantization of the Hall conductance can be induced by intrinsic spin orbit interactions and lead to the cyclotron motion of the magnons [49]. The Figure was taken from Ref. [49].

Fig. 6a. The valence bond can also form between spins that are not nearest neighbors and lead to an entanglement with longer range [54].

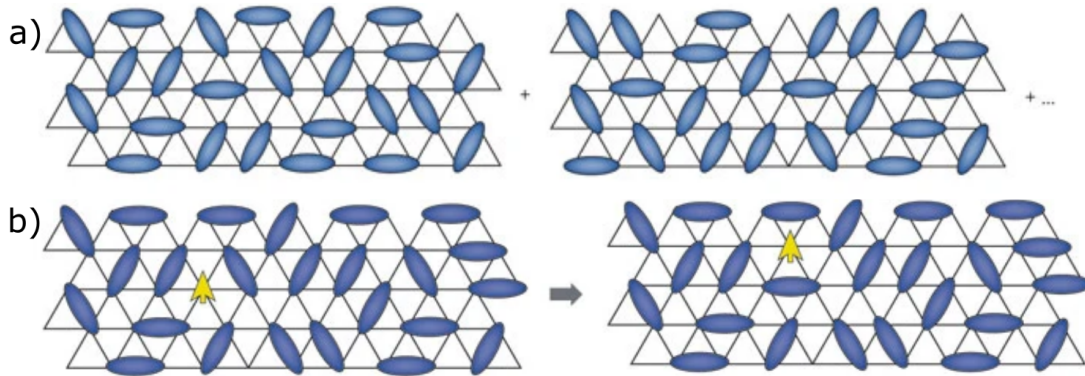


Fig. 6 | Illustration of the resonating valence bond state. **a**, Superposition of many different distribution of entangled spin pairs (blue ovals) between nearest neighbors. **b**, Fractional excitations appear in this 2D quantum spin liquid as unpaired spins that can move by locally adjusting the valence bonds. The fractional excitations are called spinons. The Figure was taken from Ref. [54].

The initial interest in this state arose from the idea that the insulating phase of La_2CuO_4 is the resonating valence bond state and could be made into a high-temperature superconductor with sufficient doping [55]. Besides the idea to find novel superconducting materials, the resonating valence bonds state receives attention for another reason. It is a type of quantum spin liquid (QSL) state and there are ideas to create topological quantum computers based on QSL that are fault-tolerant [56].

Quantum spin liquids are defined as states with long-range quantum entanglement between local degrees of freedom [57, 58]. This means that it is not possible to specify the spins on each site individually and, as consequence, there cannot be a magnetically ordered ground-state even at a temperature of absolute zero. However,

the absence of long-range magnetic order is not adequate to be used as definition for the quantum spin liquid state since it is experimentally impossible to measure the magnetic order at absolute zero. Another definition, found in literature, is that a quantum spin liquid is a state with fractional excitations [59]. An example for a fractional excitation is the spinon which is a spin-1/2 excitation (see Fig. 6b) and can be regarded as half of a magnon.

In one dimension, quantum spin liquids are known and well described in the form of the spin-1/2 quantum antiferromagnetic chain [60] and the spin-1 quantum antiferromagnetic chain [61]. Fractional excitations appear in the spin-1/2 chain as domain walls after a spin was flipped by, for example, a neutron during an experiment. The domain walls are spinons carrying a spin 1/2 and can move along the chain. A continuum of excitations is formed by the spinons as shown in Fig. 7. In contrast, the spin-1 antiferromagnetic chain corresponds to a gapped quantum spin liquid where there is an energy gap to the excitations called Haldane gap [61]. Haldane received the Nobel prize in 2016 for the theoretical discoveries of topological phase transitions and topological phases of matter what included his work on this type of spin chain [61]. In this chain, each spin-1 is formed by two spin-1/2 constituents that create a spin singlet with their respective neighboring spin-1/2. This leaves two unpaired spin-1/2 at the edges of the spin chain that create edge-states. The entanglement spectrum is a single spin-1/2 doublet [62] and the edge spins are topologically protected [63].

However, quantum spin liquids are still elusive in two dimensions. One reason, why it is more difficult to find quantum spin liquid states in two dimensions, is related to the Mermin-Wagner theorem [64]. The theorem states that there are no phase transitions to magnetic order in one or two dimensions for magnetic systems with isotropic and short-range correlations at finite temperatures. Hence, in one dimension, there is no phase transition to a magnetically long-range ordered state. But there is a phase transition to an XY quasi-long-range ordered state in two dimensions. The phase is only quasi-long-range correlated since the correlation length is described by a power law instead of an exponential function. The two-dimensional phase transition is called Berezinsky-Kosterlitz-Thouless (BKT) transition [65, 66] and its discovery was awarded the Nobel prize in 2016 [33]. The phase transition happens in the XY model where the spins are confined to the plane and rotate in the plane. To understand what happens at the BKT transition, it is intuitive to start at the magnetically ordered phase at $T = 0$ K and then increase the temperature. At finite temperatures, topological defects appear in the fully ordered magnetic structure in the form of bound vortex-antivortex pairs which further increase in number with rising temperature. At the transition temperature, the vortex-antivortex pairs unbind and become mobile what is called the BKT transition (see Fig. 8) [67]. Thin He films

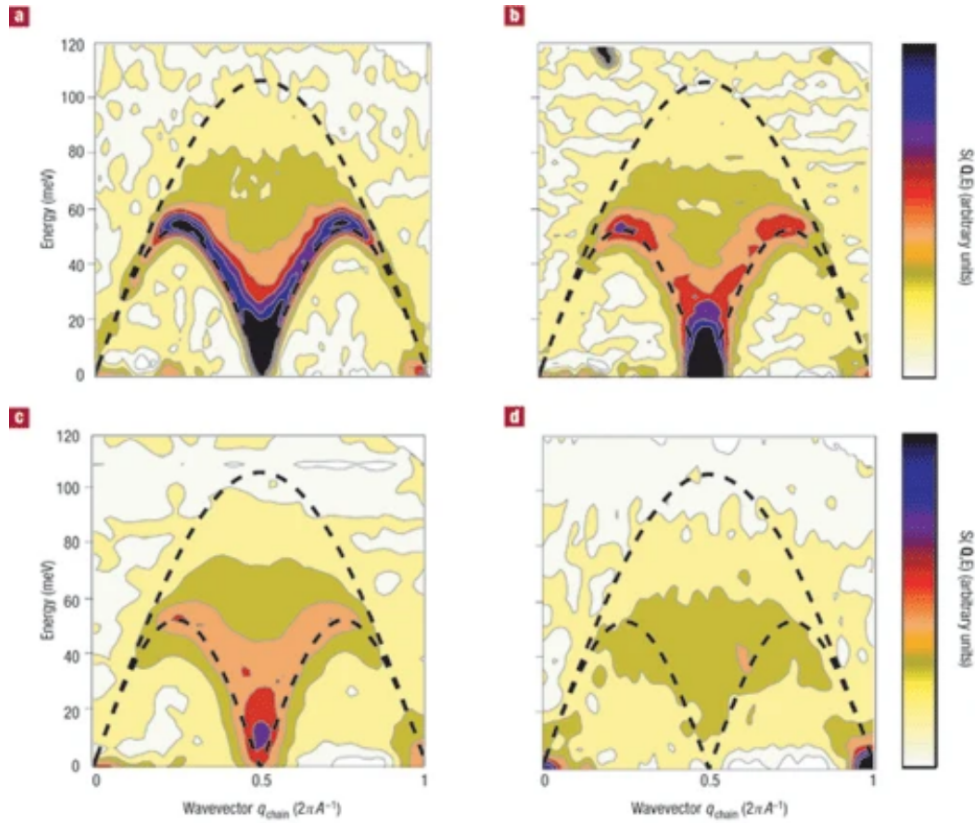


Fig. 7 | Spinon continuum in KCuF_3 . The spin-wave excitations are shown for the temperatures **a**, $T = 6$ K, **b**, $T = 50$ K, **c**, $T = 150$ K, **d**, $T = 300$ K. The black lines indicate the calculated region where the multi-spinon continuum appears for $T = 0$ K. The Figure was taken from Ref. [60].

are an example where the BKT transition was found and their Hamiltonian can be mapped to the XY model [67, 68].

In general, disordered states are expected to appear in frustrated magnetic materials. Magnetic frustration refers to the inability of the system to align all spins in their preferred direction simultaneously. There are three mechanisms how frustration appears in a material. The first is geometric frustration that originates from the lattice of magnetic ions. Examples are the triangular and kagome antiferromagnets where the magnetic ions sit in the corners of equilateral triangles. The triangular lattice has the triangles sharing their sides whereas the triangles share corners on the kagome lattice. If one spin points up and another down, then the third spin cannot simultaneously satisfy the antiferromagnetic order to both of the other spins and this leads to the frustration as shown in Fig. 9a. Geometric frustration is not relevant for the honeycomb lattice but frustration can also arise from the competition between the interactions of spins on different lattice sites. For example, if the nearest and next-nearest neighbor spins both favor antiferromagnetic alignment, all three spins cannot be satisfied at the same time (see Fig. 9b). This exchange frustration can be present in honeycomb materials and is a hint in the search for quantum spin liquid states in

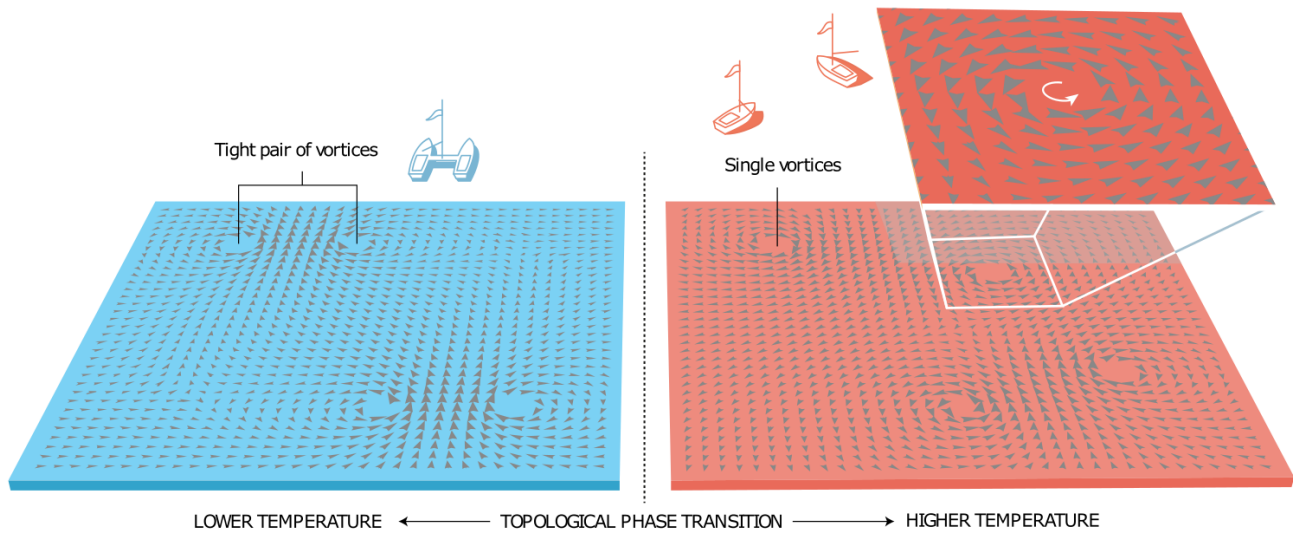


Illustration: ©Johan Jarnestad/The Royal Swedish Academy of Sciences

Fig. 8 | Illustration of the Berezinsky-Kosterlitz-Thouless transition. Below the critical temperature, bound vortex-antivortex pairs appear as topological defects of the magnetically ordered system and unbind into mobile (anti-)vortices at the critical temperature. The Figure was taken from Ref. [33]; © Johan Jarnestad/The Royal Swedish Academy of Sciences.

such systems.

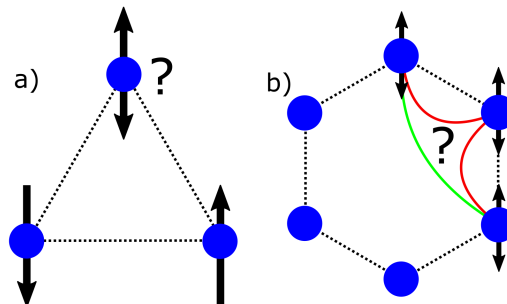


Fig. 9 | Schematic of frustration in magnets. **a**, Geometric frustration: the spins on the equilateral triangle cannot form an antiferromagnetic order between all three spins at the same time. **b**, Exchange frustration: the antiferromagnetic exchange interactions between nearest (red) and next-nearest neighbors (green) cannot be satisfied simultaneously.

There are promising candidate materials to contain a two-dimensional quantum spin liquid phase but an unequivocal determination of a quantum spin liquid ground-state remains to be seen. Particular interest is placed on materials with a honeycomb structure due to the exactly solvable Kitaev model that is based on anisotropic exchange interactions [69]. Prominent examples for Kitaev materials are Na_2IrO_3 [70] and $\alpha\text{-RuCl}_3$ [71].

All things considered, the honeycomb lattice of magnetic ions is a playground for fundamental research that may also result in novel technological applications. This makes the study of such

materials an exciting endeavor. In this thesis, I investigate two systems that are magnetic equivalents of graphene, ErBr_3 and YbBr_3 . Of particular interest are the ground-states and their possible topological properties. Disordered quantum spin liquid phases are possible. The same is true for quasi-long range ordered phases associated with a Berezinsky-Kosterlitz-Thouless transition.

4 Rare-earth trihalides ErBr₃ and YbBr₃

The thesis presents the investigation of the magnetic ground-state and excitations in the rare-earth tri-halides ErBr₃ and YbBr₃ by elastic and inelastic neutron scattering. I first introduce the methods and results common for both systems. Afterwards, the specific methods and results for the respective materials are presented.

4.1 Crystal structure

ErBr₃ and YbBr₃ belong to a part of the rare-earth trihalide family, RBr₃ (R = Yb, Er, Dy, Tm, Tb), that crystallizes with the BiI₃ layer structure in the rhombohedral space group $R\bar{3}$ (148) (see Fig. 11). They are van der Waals (vdW) systems with honeycomb layers stacked along the *c*-axis. Their unit cell consists of six rare earth R³⁺ ions surrounded by 18 Br⁻ ions with lattice parameters dependent on the specific rare-earth ion as shown in Table 1. The rare earth ions occupy the site (6c) at (0, 0, ±*z*), (0, 0, ±*z*) + (2/3, 1/3, 1/3), and (0, 0, ±*z*) + (1/3, 2/3, 2/3), with *z* = 1/6. Two-dimensional undistorted honeycomb planes are formed by the rare-earth ions perpendicular to the *c*-axis where the crystallographic positions of the rare-earth ions have C₃ point symmetry. The Br⁻ ions are arranged in a hexagonal densest packing around the rare-earth ions.

	<i>a</i> [Å]	<i>b</i> [Å]	<i>c</i> [Å]
ErBr ₃	7.005	7.005	18.89
YbBr ₃	6.97179(18)	6.97179(18)	19.1037(7)

Table 1 | Lattice parameters.

ErBr₃ lattice parameters were measured at *T* = 1.5 K [72].

YbBr₃ lattice parameters were measured at room temperature.

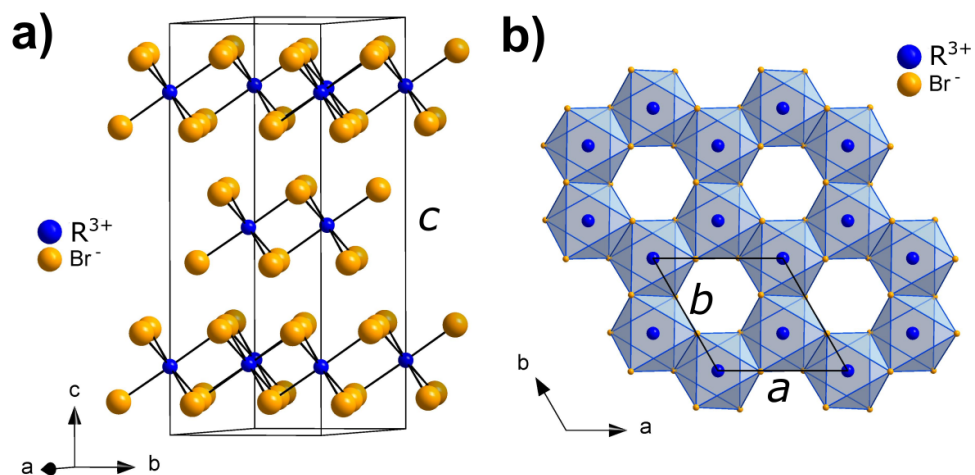


Fig. 10 | Crystal structure of ErBr₃ and YbBr₃. **a**, View along [210] on the unit cell. **b**, Honeycomb layer formed by the rare-earth ions.

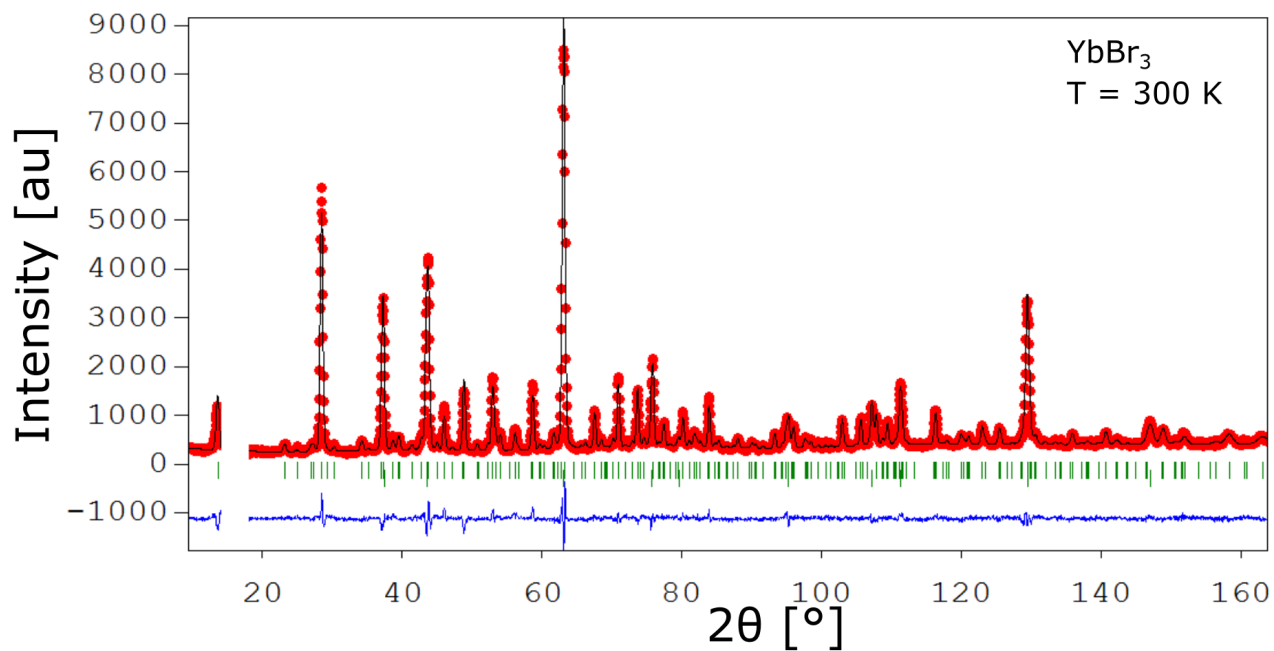


Fig. 11 | Neutron powder diffraction pattern of YbBr₃. The diffraction pattern is shown together with the fit made in Fullprof [73].

4.2 Crystal electric field

The crystalline electric field or crystal field (CEF) is produced by the potential of the charged ions in the crystal. A considerable magnetic anisotropy can originate from the CEF. Hence, it is important to understand its influence on the magnetic ground-state. It is difficult to describe the CEF since it is a many-body phenomenon that arises from the whole crystal system. Commonly, the CEF is described by modeling the electrostatic potential with spin operators that transform like the potential operators [74]. The Stevens operators O_n^m are used here to parameterize the CEF [75] together with the CEF-parameters B_n^m . The C_3 point group symmetry of the rare-earth site restricts the non-zero B_l^m parameters [76] and results in the following CEF-Hamiltonian

$$\begin{aligned} \mathcal{H}_{CEF} = & B_2^0 O_2^0 + \\ & B_4^0 O_4^0 + B_4^{+3} O_4^{+3} + B_4^{-3} O_4^{-3} + \\ & B_6^0 O_6^0 + B_6^{+3} O_6^{+3} + B_6^{-3} O_6^{-3} + B_6^{+6} O_6^{+6} + B_6^{-6} O_6^{-6} \end{aligned} \quad (2)$$

Er³⁺ and Yb³⁺ are both Kramers ions with $J = 15/2$ and $J = 7/2$ multiplets, respectively, that split into eight and four Kramer's doublets due to the CEF. Inelastic neutron scattering of the CEF was measured in ErBr₃ and YbBr₃. By a least-square fit to the inelastic neutron scattering data, the CEF-parameters were obtained for the two compounds. Table 2 shows the CEF-parameters.

The observed and calculated neutron intensities of the CEF in ErBr₃ are presented in Fig. 12. Three peaks were found at $E \sim 1.5$ meV, 3.0 meV and 6.2 meV at a temperature of $T = 1.5$ K. Each peak represents the transition from the lowest CEF level to one of the seven excited CEF levels that belong to the $^4I_{15/2}$ multiplet. Not all transitions between the CEF-levels have necessarily a non-zero intensity and therefore it is not always possible to observe all Kramers doublets for a specific temperature. The calculated neutron intensities and levels reproduce the measured CEF well with the CEF-parameters in Table 2. Ground-state expectation values for the spin-operators follow from the CEF-parameters as $\langle J_{\perp} \rangle = 3.14$ and $\langle J_{\parallel} \rangle = 0.33$ where the subscript indicates spin orientations measured relative to the c-axis. Hence, there is a strong easy-plane anisotropy present in ErBr₃ with $\langle J_{\perp} \rangle / \langle J_{\parallel} \rangle \sim 10$. The magnetic moment of ErBr₃ is $4.7 \mu_B$ at $T = 80$ mK obtained from neutron diffraction [72].

Fig. 12 presents the comparison between observed and calculated neutron intensities in YbBr₃. The lowest excited doublet is observed at ~ 15 meV followed by excitations at 25 meV and 29 meV. Hence, YbBr₃ ground-state doublet can be regarded as an effective $S = 1/2$ state since it is well separated from the first excited level. The calculations reproduce the measured CEF well with the parameters in Table 2

although the shoulder at ~ 18 meV is not fully understood. Ground-state expectation values for the spin-operators follow from the CEF-parameters as $\langle J_{\perp} \rangle = 1.2$ and $\langle J_{\parallel} \rangle = 0.8$ where the subscript indicates spin orientations measured relative to the c -axis. There is an easy-plane anisotropy present in YbBr₃ with $\langle J_{\perp} \rangle / \langle J_{\parallel} \rangle \sim 1.5$. The magnetic moment of YbBr₃ is found to be $\approx 2 \mu_B$.

Summarized, the obtained CEF-parameters describe the respective rare-earth trihalides well and both systems feature an easy-plane anisotropy. Particularly, ErBr₃ shows a strong easy-plane anisotropy. The anisotropy can also be expressed by effective g factors that replace the g Landé factors [77]. For ErBr₃, the easy-plane anisotropy in results for a doublet ground-state in $g_x = g_y = 9.4$ and $g_z = 0.1$. YbBr₃ has an anisotropy that is represented for a doublet ground-state by $g_x = g_y = 4$ and $g_z = 2.667$.

[meV]	B_2^0	B_4^0	B_4^3	B_4^{-3}	B_6^0	B_6^3	B_6^{-3}	B_6^6	B_6^{-6}
ErBr ₃	-7.35	6.1	0.01	9.2	0.45	6.17	14.8	32.8	17.4
YbBr ₃	-6.49	-0.51	58.53	52.12	6.01	48.11	56.30	33.21	41.12

Table 2 | CEF paramters obtained from INS.

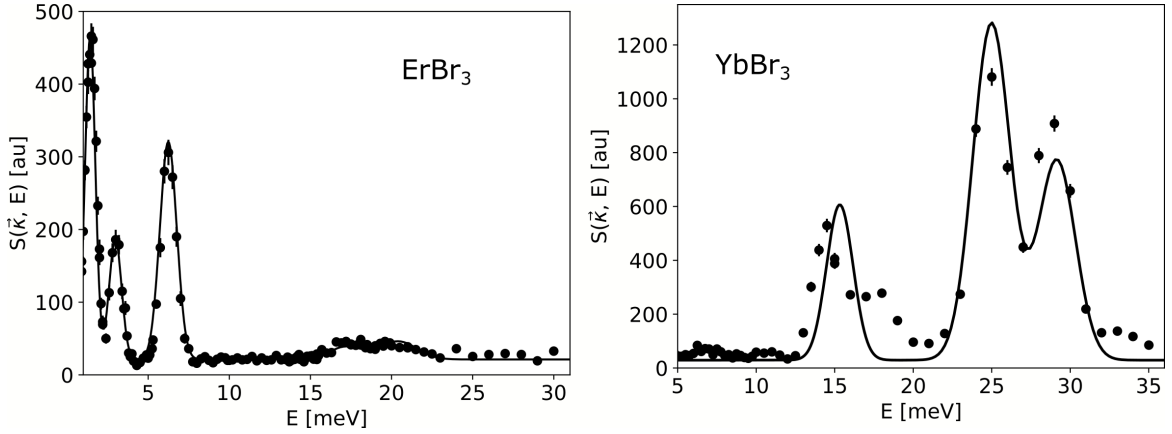


Fig. 12 | Crystal electric field in ErBr₃ and YbBr₃. Crystal electric field (CEF) excitations measured by inelastic neutron scattering taken at $T = 1.5$ K. The solid line is the calculated intensity for the CEF-parameters given in Table 2. Error bars are standard deviations.

4.3 Magnetic susceptibility

The magnetic susceptibility was measured for ErBr₃ and YbBr₃ single-crystal samples with magnetic fields applied parallel to the crystallographic *a*- and *c*-axis corresponding to fields parallel and perpendicular to the honeycomb planes, respectively. Fig. 13 presents the measured magnetic susceptibilities for the two rare-earth trihalides. There is a strong easy-plane anisotropy observable in the magnetic susceptibility of ErBr₃ with $\chi_a = \chi_b \sim 3\chi_c$ at $T = 1.5$ K (see Fig. 13a). YbBr₃ also shows an easy-plane anisotropy below $T = 10$ K with $\chi^a = \chi^b \sim 1.3\chi^c$ (see Fig 13b). The inset of Fig. 13b presents the low-temperature regime where there is a broad peak in the susceptibility at $T = 2.75$ K for both the in- and out-of-plane component. However, there is no evidence for magnetic long-range order down to at least $T = 100$ mK as shown later. Simulations of the Van-Vleck magnetic susceptibility are included in Fig. 13 for both materials. The measurement was fitted by a least-square fit with CEF-parameters as variables. The single-ion susceptibility is

$$\chi_{\alpha\beta}^0 = \sum_{pp'}^{E_p \neq E_{p'}} \frac{\langle p | S_\alpha | p' \rangle \langle p' | S_\beta | p \rangle}{E_{p'} - E_p - i\hbar\epsilon} (n_p - n_{p'}) + (k_B T)^{-1} \sum_{pp'}^{E_p = E_{p'}} \langle p | S_\alpha | p' \rangle \langle p' | S_\beta | p \rangle n_p \quad (3)$$

where $E_p, E_{p'}$ are the energies to the states p, p' , ϵ is the finite line-width or resolution, k_B is the Boltzmann constant and $n_p, n_{p'}$ are the Boltzmann factors of the states p, p' . In the limit $\epsilon \rightarrow 0$, the single-ion susceptibility is equal to the Van-Vleck susceptibility. Eigenstates and eigenvalues are obtained from the diagonalization for the CEF-Hamiltonian given by the CEF-parameters of the two rare-earth trihalides. The obtained CEF-parameters are shown in table 3. However, both measurements show that ErBr₃ and YbBr₃ show an easy-plane anisotropy.

[meV]	B_2^0	B_4^0	B_4^3	B_4^{-3}	B_6^0	B_6^3	B_6^{-3}	B_6^6	B_6^{-6}
ErBr ₃	-7.80	6.69	6.78	12.29	0.42	7.59	22.22	8.453	32.63
YbBr ₃	-5.14	-0.59	57.43	51.31	6.09	50.21	55.56	33.9	42.4

Table 3 | CEF parameters determined from the magnetic susceptibility.

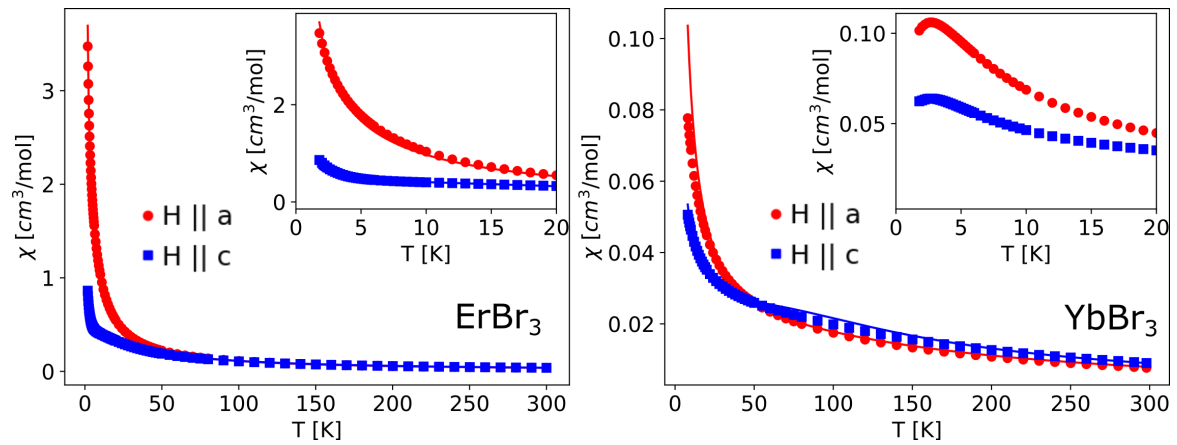


Fig. 13 | Magnetic susceptibility. The magnetic susceptibility of ErBr₃ and YbBr₃ is shown together with the simulation of the Van-Vleck susceptibility calculated with the CEF-parameters in Table 3. The inset shows the low-temperature regime of the magnetic susceptibility of YbBr₃. Measurements performed by K. Krämer at the university of Bern.

4.4 Dipolar interactions

Dipolar interactions (DI) are always present in materials but, in general, are weak compared to other interactions. Their contribution is often negligibly small and not considered in theoretical models. However, there are also systems where DI play a considerable role and are required to explain the behavior of the system. ErBr₃ has a large magnetic moment and it is necessary to confirm if the DI play a significant role in this system.

Dipole-dipole interactions between the magnetic ions are long-range as well as anisotropic. The dipolar interaction tensor $\overline{\overline{D}}$ is given by

$$D_{ij}^{\alpha\beta} = 3 \frac{r_{ij}^{\alpha} r_{ij}^{\beta}}{|\vec{r}_{ij}|^5} - \frac{\delta^{\alpha\beta}}{|\vec{r}_{ij}|^3}. \quad (4)$$

where α, β are the tensor or vector components, i, j run over all ions of the system, $\vec{r}_{ij} = \vec{r}_j - \vec{r}_i$ is the vector connecting the i th and j th ion and δ is the Kronecker-delta. The dipolar Hamiltonian is written as

$$\mathcal{H} = -\frac{\mu_0 (g\mu_B)^2}{8\pi} \sum_{ij} \sum_{\alpha\beta} D_{ij}^{\alpha\beta} S_i^{\alpha} S_j^{\beta} \quad (5)$$

where μ_0 is the vacuum permeability and \vec{S}_i is the spin operator of the i th ion. In MF theory, the classical ground-state is determined by the largest eigenvalue of the Fourier-transform of the interaction tensor [79, 80, 81]. The corresponding eigenvector represents the spin arrangement. Hence, the calculation of the lattice sum of the Fourier-transform of the dipolar interactions provides information about the magnetic order. But this lattice sum is difficult to calculate and there are different approaches to do this. The brute force approach is to calculate the sum over a sufficiently large lattice of dipole moments so that the sum converges to a satisfactory degree. However, this method is extremely computation intensive and large sample lattices need to be considered to reach a required precision. So, an efficient way to calculate the lattice sum of the DI, or more precisely the Fourier transform of the DI, is required and, luckily, available in the form of the so-called Ewald's method [78]. Ewald's summation is a mathematical trick to transform slowly converging sums into rapidly converging ones. A description of this method is presented in Section 7.2. Instead of calculating the DI in real space, it is advantageous to directly calculate the Fourier-transformed DI since they can be directly applied in latter calculations of the spin-wave excitations (see section 4.5). A difficulty is that the honeycomb lattice is a non-Bravais lattice consisting of two interlaced triangular sublattices. In bipartite lattices, it is necessary to not only calculate the interactions in the sublattices

but also the interactions between the sublattices. Section 7.3 provides details of the calculations of the Fourier-transformed DI.

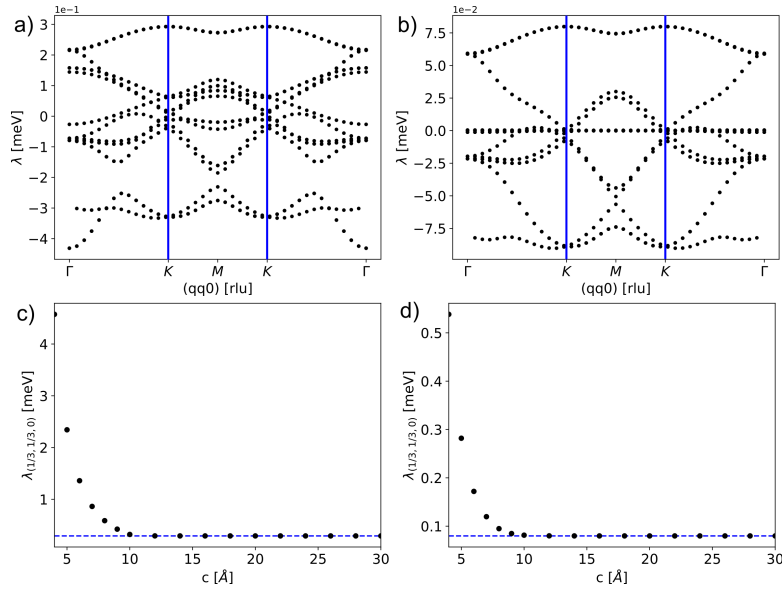


Fig. 14 | Magnetic ordering and interlayer interactions governed by dipolar interactions. The dispersion of the eigenvalues of the Fourier-transform of the dipolar interactions tensor is presented using **a**, the free ion magnetic moment of Er³⁺ and **b**, the calculated magnetic moment reduced by the CEF anisotropy of ErBr₃. Both dispersions show maxima at $\vec{Q}_0 = (1/3, 1/3, 0)$ and at $(2/3, 2/3, 0)$ that is equivalent to $(-1/3, -1/3, 0)$. The dependence of the largest eigenvalue on the lattice parameter c is shown using **c**, the free ion magnetic moment of Er³⁺ and **d**, the calculated magnetic moment reduced by the CEF anisotropy of ErBr₃. ErBr₃ with $c = 18.89 \text{ \AA}$ is well in the 2D limit [83].

Fig. 14a presents the dispersion of the Fourier transform of the dipolar interactions along $\vec{k} = (q, q, 0)$ calculated for the ErBr₃ crystal with six Er-ions in the chemical cell as shown in Fig. 11a. \vec{k} of the largest eigenvalue is identical to the magnetic propagation vector $\vec{Q}_0 = (1/3, 1/3, 0)$. Therefore, the magnetic ground-state, that was observed by neutron diffraction [72], is in agreement with mean-field theory as well as the calculations by Rozenbaum [82] for magnetic dipoles on the bipartite honeycomb lattice. Within mean-field theory [81], the critical temperature of the magnetic phase transition is $T_{MF} = \max\{\lambda_{\vec{Q}_0}/k_B\}/3 \sim 0.3 \text{ K}$ which is similar to the magnetic ordering temperature in ErBr₃ observed by neutron diffraction [72]. Noteworthy is that Heisenberg interactions are not able to reproduce the magnetic propagation vector $\vec{Q}_0 = (1/3, 1/3, 0)$ even if up to the third-nearest neighbor interactions are included [77]. In addition, the interlayer dependence due to dipole-dipole interactions can be investigated by calculating the ground-state energy as a function of the lattice parameter c [83]. Fig. 14b shows that the interlayer interactions are negligible for lattice parameters $c > 10 \text{ \AA}$ since the dipolar energy is constant. Therefore, ErBr₃ is well within the 2D limit with $c = 18.89 \text{ \AA}$ and an interlayer spacing of $c/3 = 6.3 \text{ \AA}$. This result is confirmed by the observation of a magnetic rod of scattering that extends along the c -axis in ErBr₃ as shown in Fig. 15.

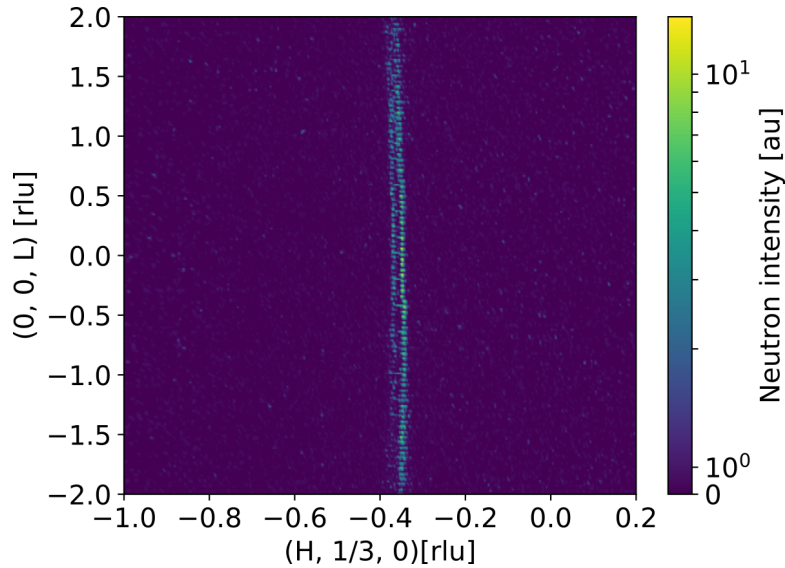


Fig. 15 | Magnetic scattering in the plane $(H, 1/3, L)$ -plane of ErBr_3 . The elastic neutron scattering shows the rod of the magnetic scattering at $(1/3, 1/3, L)$ over several Brillouin zones in L . The measurements were taken at $T = 30$ mK.

Similar conclusions can be obtained for YbBr_3 as shown in Fig. 16a where the dispersion of the eigenvalues along the direction $(H, H, 0)$ has a maximum at $(1/3, 1/3, 0)$ and $(2/3, 2/3, 0)$. However, measurements of the neutron diffraction in YbBr_3 show a magnetic ordering vector $\vec{Q}_0 = (0, 0, 0)$ as shown in Fig. 33. The introduction of antiferromagnetic Heisenberg interactions strongly modifies the dispersion of the eigenvalues and results in the maxima of the eigenvalue of the Fourier-transform of the exchange tensor to appear at the Γ points (see Fig. 16b). The spin structure is obtained by the eigenvector of the largest eigenvalue and corresponds to a Néel ordered state. Without easy-plane anisotropy, the dipolar interactions align the moments parallel to the c -axis [84, 85]. But the easy-plane anisotropy $g_z/g_x = 0.667$ leads to spins orientations orthogonal to the c -axis. These calculations indicate that a sufficiently strong anisotropy is required to counteract the influence of the dipolar interactions.

One could think that the long-range dipolar interactions may lead to an interlayer coupling in YbBr_3 that affects the two-dimensional ordering. As in ErBr_3 , the large interlayer spacing ensures that there are no interactions between the honeycomb planes. For interlayer spacings between Yb planes with $c \gtrsim 10$ Å, the dipolar energy becomes independent from the interlayer spacing as shown in Fig. 17a. Therefore, YbBr_3 is in the 2D limit and interlayer interactions can be neglected and the calculations for a single honeycomb layer reproduces the correct magnetic ordering vector in YbBr_3 (see Fig. 17b).

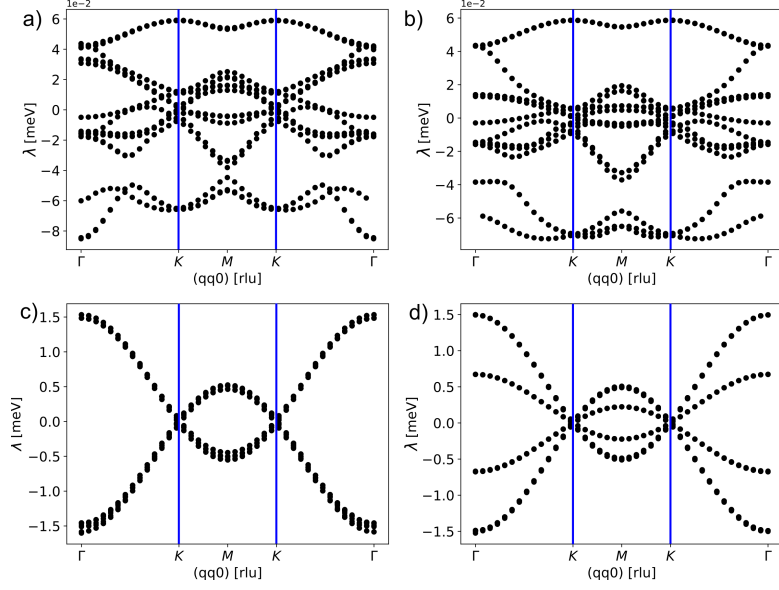


Fig. 16 | Magnetic ordering vector. The eigenvalues of the interactions tensor are plotted along the $(q, q, 0)$ direction. There are six magnetic rare-earth ions in the unit cell of YbBr₃ with R-3 crystal structure. Only dipolar interactions are considered for **a**, the free ion magnetic moment of Yb³⁺ and **b**, the calculated magnetic moment reduced by the CEF anisotropy of YbBr₃. The maxima of the eigenvalues are found at the K points and the magnetic ordering vector is $\vec{Q}_0 = (1/3, 1/3, 0)$. Heisenberg exchange interactions are added to the interaction tensor and the dispersions are shown for **c**, the free ion magnetic moment of Yb³⁺ and **d**, the calculated magnetic moment reduced by the CEF anisotropy of YbBr₃. The maxima of the eigenvalues are found at the Γ points and the magnetic ordering vector is $\vec{Q}_0 = (0, 0, 0)$ when antiferromagnetic exchange interactions are added. In the Figure, the nearest-neighbor Heisenberg exchange is $J = -0.5$ meV.

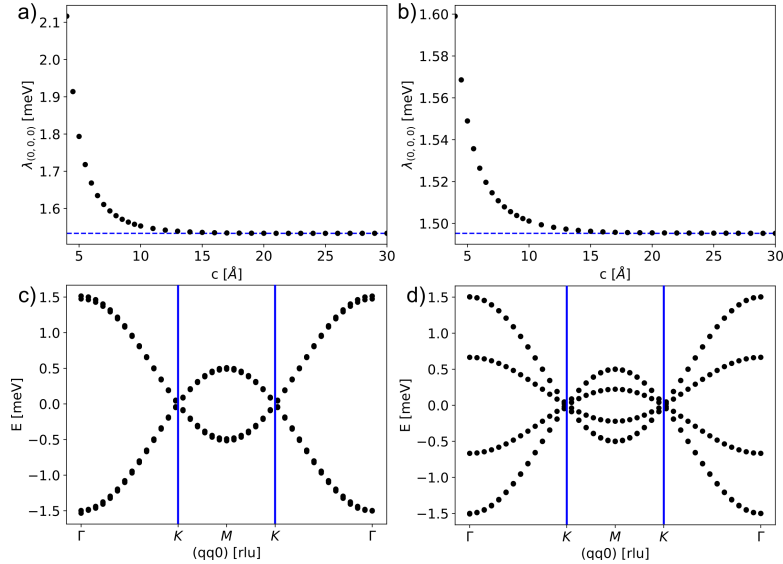


Fig. 17 | Interlayer interactions and monolayer magnetic ordering. Value of the largest eigenvalue as function of the interlayer separation c calculated for **a**, the free ion magnetic moment of Yb³⁺ and **b**, the calculated magnetic moment reduced by the CEF anisotropy of YbBr₃. The eigenvalue monotonously decreases towards the value at infinite distance that is effectively reached at about $c \gtrsim 15$ Å. **c** and **d** are the same as Fig. 16c and d but calculated for a single layer of YbBr₃.

4.5 Model Hamiltonian and the MF-RPA method

This section introduces the mean-field random-phase approximation (MF-RPA) that is utilized to calculate the dispersion and intensity of the spin-wave excitations. The dynamic susceptibility $\chi(\vec{\kappa}, \mathbf{E})$ is calculated in the mean-field approximation that is related to the Fourier-transform of the spin correlation function by the fluctuation-dissipation theorem [86]. In the MF-RPA theory, single-ion interactions, like crystal-field and mean-field Hamiltonians, are treated exactly and the RPA is used to approximate the interactions between magnetic ions [86].

The general Hamiltonian used in this thesis is given by

$$\begin{aligned}\mathcal{H} &= -\frac{1}{2} \sum_{ij} \sum_{\alpha\beta} [g_\alpha^2 J_\alpha(i, j) + g_\alpha g_\beta D_{\alpha\beta}(i, j)] S_i^\alpha S_j^\beta \\ &= -\frac{1}{2} \sum_{ij} \sum_{\alpha\beta} \overline{\overline{\mathcal{J}}}_{\alpha\beta}(i, j) S_i^\alpha S_j^\beta\end{aligned}\quad (6)$$

where g are the Landé- g factors, $\overline{\overline{\mathcal{J}}}(i, j)$ and $\overline{\overline{D}}(i, j)$ are the exchange interactions and dipolar interactions between the i th and j th ion, respectively. The interaction parameters are expressed in meV. $\alpha, \beta = x, y, z$ indicate the tensor components in Cartesian coordinates.

In the MF-RPA, the dynamic susceptibility is given by

$$\overline{\overline{\chi}}(\vec{\kappa}, E) = \{\overline{\overline{1}} - \overline{\overline{\chi}}^0(E) \overline{\overline{\mathcal{J}}}(\vec{\kappa})\}^{-1} \overline{\overline{\chi}}^0(E) \quad (7)$$

where $\overline{\overline{1}}$ is the unit matrix and $\overline{\overline{\mathcal{J}}}(\vec{\kappa})$ is the interaction tensor. $\overline{\overline{\chi}}_0$ is the single ion susceptibility calculated using

$$\begin{aligned}\chi_{\alpha\beta}^0(E) &= \sum_{pp'}^{E_p \neq E_{p'}} \frac{\langle p | S_\alpha | p' \rangle \langle p' | S_\beta | p \rangle}{E_{p'} - E_p - E - i\hbar\epsilon} (n_p - n_{p'}) \\ &+ \frac{1}{k_B T} \sum_{pp'}^{E_p = E_{p'}} \langle p | S_\alpha | p' \rangle \langle p' | S_\beta | p \rangle \frac{\epsilon}{\epsilon + E} n_p\end{aligned}\quad (8)$$

where ϵ is the damping. The eigenvalues and eigenvectors required to calculate the static susceptibility are obtained from the diagonalization of the MF Hamiltonian. The MF-Hamiltonian is found as

$$\begin{aligned}
\mathcal{H} &= \sum_i (\mathcal{H}_{CEF}(i)) - \frac{1}{2} \sum_{i \neq j} \overline{\overline{\mathcal{J}}}(ij) (\vec{S}_i \vec{S}_j) \\
&= \sum_i (\mathcal{H}_{CEF}(i)) - \frac{1}{2} \sum_{i \neq j} \overline{\overline{\mathcal{J}}}(ij) ((\vec{S}_i - \langle \vec{S}_i \rangle) (\vec{S}_j - \langle \vec{S}_j \rangle)) \\
&\quad + \vec{S}_i \langle \vec{S}_j \rangle + \vec{S}_j \langle \vec{S}_i \rangle - \langle \vec{S}_i \rangle \langle \vec{S}_j \rangle \\
&\stackrel{MF}{\approx} \sum_i (\mathcal{H}_{CEF}(i) - (\vec{S}_i - \frac{1}{2} \langle \vec{S}_i \rangle) \sum_j \overline{\overline{\mathcal{J}}}(ij) \langle \vec{S}_j \rangle) \\
&= \sum_i \mathcal{H}_{MF}(i) \\
\mathcal{H}_{MF}(i) &= \mathcal{H}_{CEF}(i) - (\vec{S}_i - \frac{1}{2} \langle \vec{S}_i \rangle) \sum_j \overline{\overline{\mathcal{J}}}(ij) \langle \vec{S}_j \rangle
\end{aligned} \tag{9}$$

It is required for equation Eq. 7 to hold that all magnetic ions are equivalent with the same orientation of spins. This is the case for a ferromagnet but not for an antiferromagnet or other complex spin structures. The rotation into a local coordinate frame allows to treat the ions as equivalent that locally appear in a ferromagnetic order. The transformation $\overline{\overline{U}}_i$ from the local to the laboratory coordinate system [46] is given by

$$\overline{\overline{U}}_i = \begin{pmatrix} \cos \theta_i \cos \phi_i & \cos \theta_i \sin \phi_i & -\sin \theta_i \\ -\sin \phi_i & \cos \phi_i & 0 \\ \sin \theta_i \cos \phi_i & \sin \theta_i \sin \phi_i & \cos \theta_i \end{pmatrix} \tag{10}$$

where θ_i and ϕ_i define the spherical coordinates of the i th spin. The MF-RPA calculations are done in the local coordinate system and the dynamic susceptibility is finally rotated back into the laboratory coordinate system. And in the last step, the polarization factor is included to correctly calculate the neutron scattering cross-section.

There are different methods to include the anisotropy into the MF-RPA that produce the same results. First, one can directly put the single-ion anisotropy into the mean-field Hamiltonian in Eq. 9 as \mathcal{H}_{CEF} that is also rotated into the local frame. This method requires to use the full spin S in the calculation and a self-consistent determination of the expectation value of the spin operator $\langle \vec{S} \rangle$ [86]. The full consideration of the CEF is not trivial as the rotation into the local frame is not straightforward and also is more computation intensive.

If the anisotropy is quite simple, like an easy-plane anisotropy, it is more efficient to replace the full CEF anisotropy with an effective term. The anisotropy is included in the g -factors and one neglects \mathcal{H}_{CEF} in Eq. 9. In Eq. 6, the g -factors are not isotropic

anymore and reflect the anisotropy caused by the CEF [77]. This method has been used to describe the spin-wave dispersion in ErBr₃ and YbBr₃.

5 ErBr₃: a 2D dipolar model system

Commonly, dipolar interactions (DI) are neglected since their energy scale is usually smaller than exchange interactions in most materials. However, DI are intrinsic interactions in all solids and there are cases where they are required to model the physics of the system. The effect of the DI is not trivial to understand as the interactions are naturally direction dependent as well as long-range. Frustration between magnetic spins is a consequence since, in general, not all interactions are satisfied simultaneously. So, it is not apparent if purely dipolar ordered magnetic systems are stable. The three-dimensional cubic dipole lattices were investigated and found to support long-range magnetic order [87]. Face- and body-centered cubic lattices display ferromagnetic order whereas the simple cubic lattice features a collinear antiferromagnetic ground-state. It was also shown that the triangular lattice exhibits ferromagnetic long-range ordering [88] and that square and honeycomb dipolar lattices have classical ground-states which are continuously degenerate [89, 82]. Additionally, the kagome lattice is naturally frustrated by its geometry and does not have a classical ground-state where the length of all spins is constant but is predicted to form a ferrimagnetic ground-state if dominated by dipolar interactions [90]. The long-range nature of the DI prevents the use of the Mermin-Wagner theorem that states the absence of long-range order for isotropic short-range Heisenberg interactions in two-dimensions [64].

The Mermin-Wagner theorem forbids long-range magnetic order in two dimensions at finite temperature but it does not exclude a phase transition to a low temperature phase without true long-range order [64, 67]. The Berezinsky-Kosterlitz-Thouless (BKT) transition is described in the 2D XY model

$$\mathcal{H}_{XY} = -J \sum_{ij} \cos(\theta_i - \theta_j) \quad (11)$$

where $J > 0$ are the Heisenberg interactions, i, j are the indices of the nearest neighbor lattice sites. $\theta_i - \theta_j$ is the angle between the i th and j th spin [65, 66]. Below the critical temperature T_{BKT} , pairs of bound vortices and anti-vortices exist as topological defects in the ferromagnetic spin structure. With increasing temperature, the number of vortex-antivortex pairs rises and the pairs unbind at the transition temperature T_{BKT} . Characteristic for the BKT transition are the different decays of the spin pair correlation functions on each side of the transition temperature. In the low temperature phase, the correlation function decays as a power law with a correlation length that is first linear and approaches the critical temperature as $\sqrt{|(T/T_{BKT}) - 1|}$ leading to quasi-long-range ordered ground-state [67]. Above

T_{BKT} , the correlation function is an exponential. In the BKT theory, the corresponding correlation length also decays as an exponential function [67]. The BKT phase has been found in different types of 2D systems that have the same symmetry and are described by the XY model including super fluid helium films [91], superconductor thin films [92] and van der Waals systems [93].

Topology is the mathematical study of quantities that are invariant under continuous deformation and also a rising topic in solid state physics [94]. In condensed matter physics, the reason for the interest in topology is that it protects states against perturbation. Furthermore, there are topological phenomena that hold potential for technological applications like the spin quantum Hall effect [94, 95]. Another prospective type of system are topological insulators [96] or their magnetic equivalents [97]. Topological insulators have surface- or edge-states, in 3D or 2D respectively, that carry spin-polarized currents where the direction of the current is determined by the spin-polarization [95]. Spin-polarised devices are highly interesting as a new technology to replace electronics that are purely based on electric charge to transport information. The current technology approaches its physical limitations in the miniaturization of transistors and integrated circuits due to Joule heating and dissipation. Spintronics is based on the idea to use spin-polarized currents to transport information and has already found application in the form of spin valves that improved the capacity of hard disk drives [98, 43]. Besides electrons, there is also the approach to use another type of (quasi-)particle, the magnon, to process and store information. The so-called magnonics technology is based on the transport of spin-waves and has a potentially lower energy consumption as well as smaller size than electronic devices. Advantageous is also that magnon-based devices can be easily tuned by external magnetic fields [51, 99]. Magnetic topological insulators possess robust surface/edge spin-waves with unidirectional propagation. Due to these topological properties magnonic applications become possible [100]. One road towards non-trivial topological edge-states are the spin-orbit interactions which open a gap in the magnon Dirac cones and allow the formation of the edge-state in the gap [101, 102] like it is proposed for CrI₃ [29]. Edge states were demonstrated in a ferromagnetic topological insulator that exhibits the magnon-Hall effect [103, 104]. Here, the antisymmetric Dzyaloshinskii-Moriya (DM) interactions act as the spin-orbit coupling in the magnetic crystals [105]. Another way to obtain topological edge-states are pseudo-dipolar interactions that were theoretically predicted to act similar to the DM interactions [106, 107]. Artificial nano-structures with DI were already investigated [108] and are an interesting possibility to create topological systems [109, 110].

This section of my thesis details the analysis of the magnetic ground-state and ex-

citations in the van der Waals honeycomb magnet ErBr₃ that features a BKT transition towards a continuously degenerate non-collinear 2D-order below $T \approx 280$ mK. Dipolar interactions and crystalline electric field anisotropy are shown to be sufficient to explain the magnetic ground-state and excitations. The dispersion of spin-wave excitations was measured by inelastic neutron scattering and is simulated with the mean-field random-phase approximation (MF-RPA). It provides insight in the relation between the dispersion of the spin excitations and continuously degenerate ground-state. Within the MF-RPA, magnetic Dirac cones were found at the corners of the Brillouin zone.

5.1 Magnetic structure of ErBr₃

Previous experiments determined the magnetic structure of ErBr₃ from powder neutron diffraction [72]. The complex non-collinear order is expressed by the magnetic ordering vector $\vec{Q}_0 = (1/3, 1/3, 0)$ that requires a magnetic unit cell three times larger than the crystallographic unit cell to describe the magnetic ordering. The same magnetic ordering was obtained from the analysis of the Fourier-transform of the DI tensor in Section 4.4. In Fig. 18a, both unit cells are shown where the magnetic unit cell is rotated by 30° and enlarged with $\sqrt{3}a \times \sqrt{3}a \times c$. The two intercalated trigonal sublattices, that form the honeycomb lattice, house Er³⁺ ions with 120° anti-ferromagnetic order and opposite chirality (see Fig. 18a). Remarkable is the infinite degeneracy of the magnetic ground-state with regard to in-plane rotations of the magnetic moments [72]. The ordered moments can be rotated by an arbitrary angle Ψ where the two sublattices rotate in opposite directions as shown in Fig. 18b. Only two-dimensional magnetic order is found in ErBr₃ from its onset at $T = 280$ mK down to 50 mK as shown below. The ordered magnetic moments have a magnitude of $\mu = 4.7 \mu_B$ at $T = 50$ mK [72].

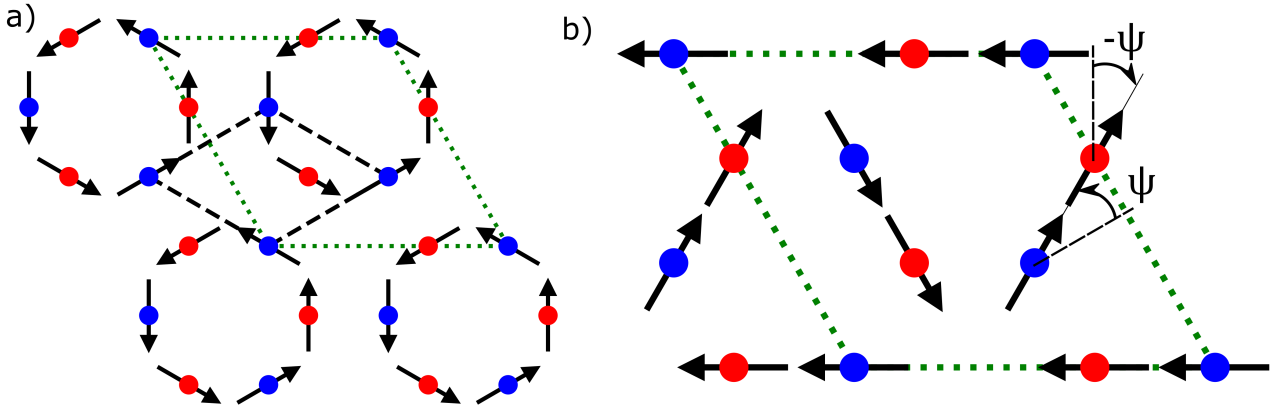


Fig. 18 | Continuously degenerate magnetic ground-state of ErBr₃. **a**, Honeycomb layer of Er³⁺ ions at $z = 1/6$ (black arrows) for $\Psi = 0$. The two trigonal sublattices of the honeycomb are shown as blue and red spheres. The crystallographic and magnetic unit cells are drawn as black and green lines, respectively. **b**, The classical magnetic ground-state is continuously degenerate and the magnetic moments can be rotated in opposite directions by varying the angle Ψ . In the Figure $\Psi = \pi/6$.

5.2 Berezinsky–Kosterlitz–Thouless transition

The two-dimensional order as well as the continuous degeneracy of the ground-state creates a resemblance of ErBr₃'s magnetic properties to the XY model in Eq. 11. Hence, it is possible that a Berezinsky–Kosterlitz–Thouless (BKT) transition exists in this material.

A BKT transition can be identified by the different types of decays in the spin correlation function $\langle \vec{S}_i \vec{S}_j \rangle$ below and above the phase transition

$$\langle \vec{S}_i \vec{S}_j \rangle \sim |\vec{r}|^{-\eta(T)} \quad T \leq T_{BKT}; \quad (12)$$

$$\langle \vec{S}_i \vec{S}_j \rangle \sim \exp(-|\vec{r}|/\xi(T)) \quad T > T_{BKT}. \quad (13)$$

where \vec{r} is the vector between ions i, j . η is a temperature dependent exponent and ξ is the correlation length above T_{BKT} . η and ξ have a specific temperature dependence [67]:

$$\eta(T) = \begin{cases} CT & T \ll T_{BKT}. \\ 1/4 & T = T_{BKT}. \end{cases} \quad (14)$$

$$\xi(T) \sim \exp(b/\sqrt{T/T_{BKT} - 1}) \quad T > T_{BKT}. \quad (15)$$

where C and b are non-universal constants [67, 112].

The lineshape of the magnetic diffuse neutron cross-section is given by the two-dimensional Fourier transform of Eq. 12 and 13 for their respective temperature ranges. Below the BKT transition, Eq. 12 is Fourier-transformed in polar coordinates and results in

$$\begin{aligned} S(\vec{\kappa}) &= \frac{1}{\sqrt{2\pi}L} \int_0^\infty \int_0^{2\pi} r^{-\eta} \exp(i\vec{\kappa}r \cos(\theta)) \exp(-\frac{r^2}{2L^2}) r dr d\theta \\ &= \frac{\sqrt{2\pi}}{L} \int_0^\infty r^{1-\eta} \exp(-\frac{r^2}{2L^2}) B_{J_0}(\vec{\kappa}r) dr \\ &= \sqrt{2\pi} (2L^2)^{-\frac{\eta}{2}} L \Gamma(1 - \frac{\eta}{2}) \mathcal{L}(\frac{\eta}{2} - 1; -\frac{(\kappa L)^2}{2}) \end{aligned} \quad (16)$$

where L is the coherence length of the neutrons which can be regarded as the instrumental resolution. B_{J_0} is the Bessel function of the first kind $J_n(z)$ and \mathcal{L} is the Laguerre polynomial $L_n(z)$. Above the BKT transition, the two-dimensional Fourier transform of Eq. 13 results in an integral without known solution

$$\begin{aligned}
S(\vec{\kappa}) &= \frac{1}{\sqrt{2\pi}L} \int_0^\infty \int_0^{2\pi} \exp\left(-\frac{r}{\xi}\right) \exp(i\kappa r \cos(\theta)) \exp\left(-\frac{r^2}{2L^2}\right) r dr d\theta \\
&= \frac{\sqrt{2\pi}}{L} \int_0^\infty \exp\left(-\frac{r}{\xi}\right) \exp\left(-\frac{r^2}{2L^2}\right) B_{J_0}(\kappa r) r dr.
\end{aligned} \tag{17}$$

Below T_{BKT} , the experimental setup used a collimation of 20° before the analyzer and 80° before the detector, resulting in a resolution $L \approx 260 \text{ \AA}$. Above T_{BKT} , the collimator before the analyzer was changed to 80° resulting in a instrumental resolution $L \approx 200 \text{ \AA}$ for the measurements.

Fig. 19 shows a magnetic peak of ErBr₃ at $\vec{\kappa} = (1/3, 1/3, 0)$ for selected temperatures together with fits of the functions in Eq. 16 and 17. Below $T \approx 270 \text{ mK}$, Eq. 16 describes the magnetic peaks better than Eq. 17. In contrast, the exponential function is a better description above $\sim 270 \text{ mK}$.

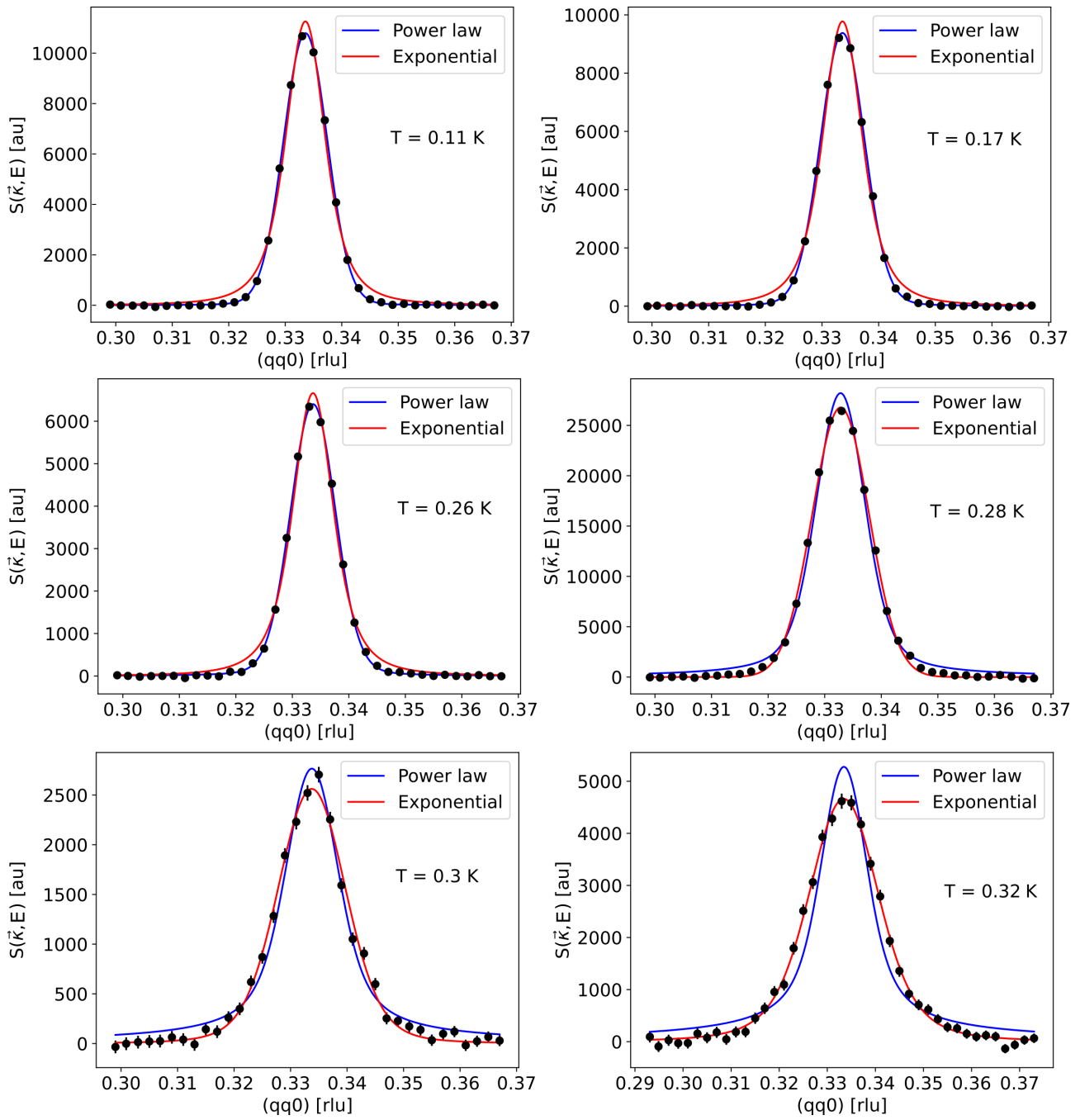


Fig. 19 |Magnetic Bragg peak of ErBr_3 . The $(1/3, 1/3, 0)$ magnetic Bragg peak is shown for different temperatures together with fits of functions in Eq. 16 and 17. The background was measured at $T = 800$ mK and subtracted.

The goodness-of-fit reflects this observation that the appropriate function changes at a critical temperature. Below the critical temperature, the power law describes the magnetic scattering well. Whereas the exponential function is far from a good representation in comparison but becomes steadily better while approaching the critical temperature, as shown in Fig. 19. At about 290 mK, the exponential function Eq. 17 reached a value of $\chi^2 \approx 1$ and well describes the measurement as it is expected above the critical temperature. It is difficult to extract the transition temperature from χ^2 since Eq. 14 is not defined above the critical temperature and Eq. 15 has a divergence at the critical temperature.

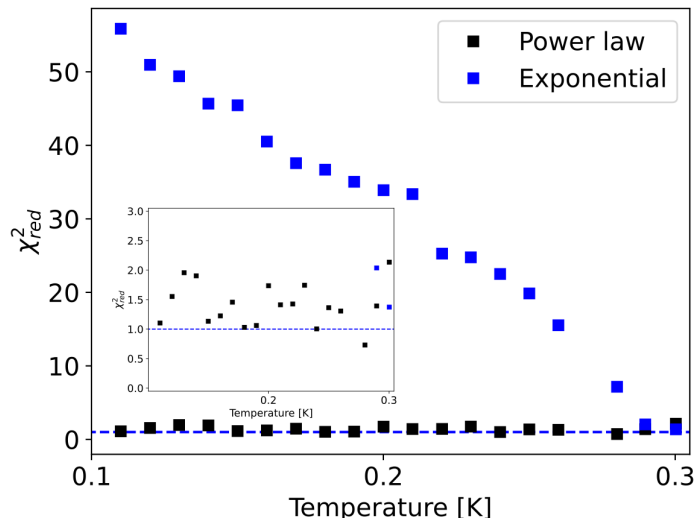


Fig. 20 | Goodness of fit: Power law and exponential. Goodness-of-fit χ_{red}^2 plotted as function of temperature for the power law and exponential function. The inset shows the χ_{red}^2 of the power law function.

Fig. 21a presents the temperature dependent correlation lengths extracted from fits with the function in Eq. 16. The phase transition happens where $\eta(T_{BKT}) = 1/4$ [67]. The critical temperature is $T_{BKT} \approx 270-280$ mK. $\eta(T)$ also shows a linear behavior with decreasing temperature away from T_{BKT} as shown in Eq. 14. The phase transition manifests also in the sudden change in instrumental resolution shown in Fig. 21b. The resolution should be temperature independent and have a constant value. The non-physical drop signifies that the critical temperature was crossed and the function in Eq. 16 is not appropriate anymore at temperatures higher than T_{BKT} . Evidence for the BKT transition is also found in the temperature dependence of the correlation length above T_{BKT} and presented in Fig. 22. From a fit with Eq. 15 for $\xi(T)$ one obtains $b = 1.394 \pm 0.076$ which is close to the value calculated by Kosterlitz for the XY-model with $b \approx 1.5$ [112].

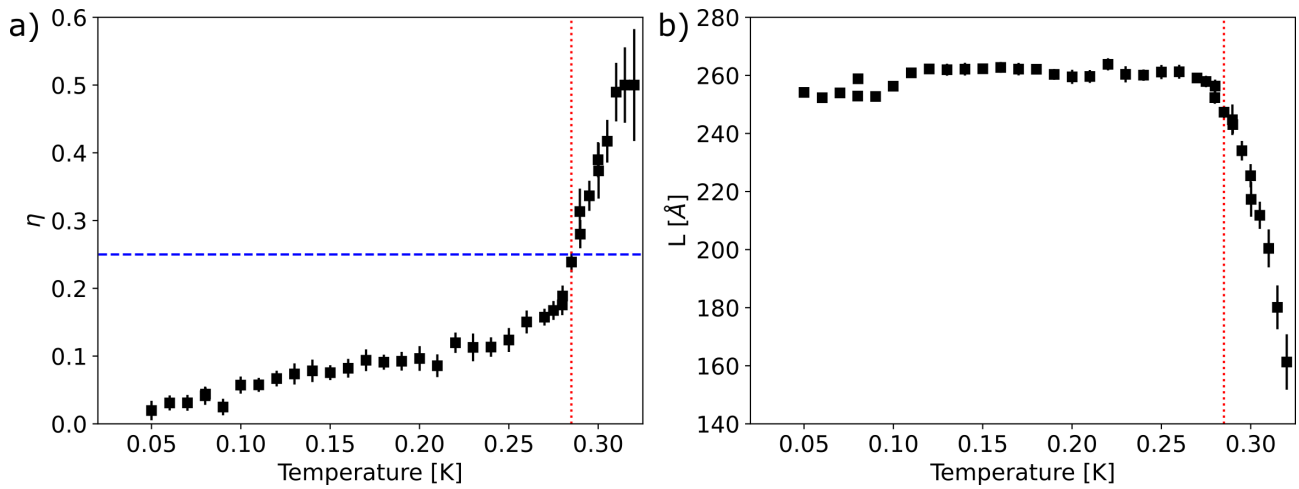


Fig. 21 | BKT-transition in ErBr₃: Power law function. **a**, Exponent η of the spin-correlation function as function of temperature. The critical value $\eta_{BKT} = 1/4$ is indicated by the blue line [67]. **b**, Instrumental resolution L as function of temperature. At the critical temperature, there is a sharp fall in L which indicates that the model does not describe the data properly above T_{BKT} . The red line indicates the critical temperature T_{BKT} .

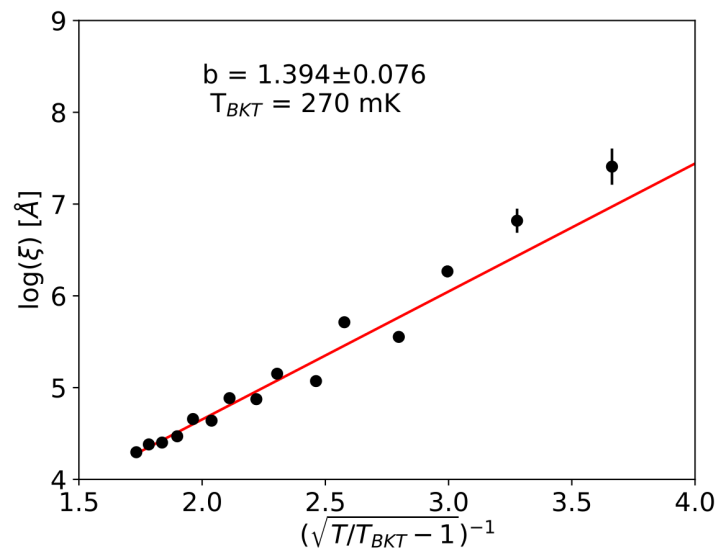


Fig. 22 | Correlation length ξ above T_{BKT} . Logarithm of the correlation length ξ as function of the inverse square-root of reduced temperature with $T_{BKT} = 270$ -280 mK. The red line is a fit with Eq. 15.

The BKT transition manifests also in the specific heat in the form of a peak that corresponds to the entropy release of the unbinding of vortex pairs. The temperature of the peak in the specific heat is about $\sim 20\%$ higher than T_{BKT} with $T \approx 330$ mK as shown in Fig. 23, The higher temperature is in agreement with predictions for the XY model that expected the peak in specific heat at a temperature 10-40% higher than T_{BKT} [67, 113]. At the critical temperature, the vortex-antivortex pairs start to unbind and release entropy that contributes to the specific heat. The highest density of these pairs that unbind is at a temperature higher than the transition temperature leading to a peak in the specific heat above T_{BKT} .

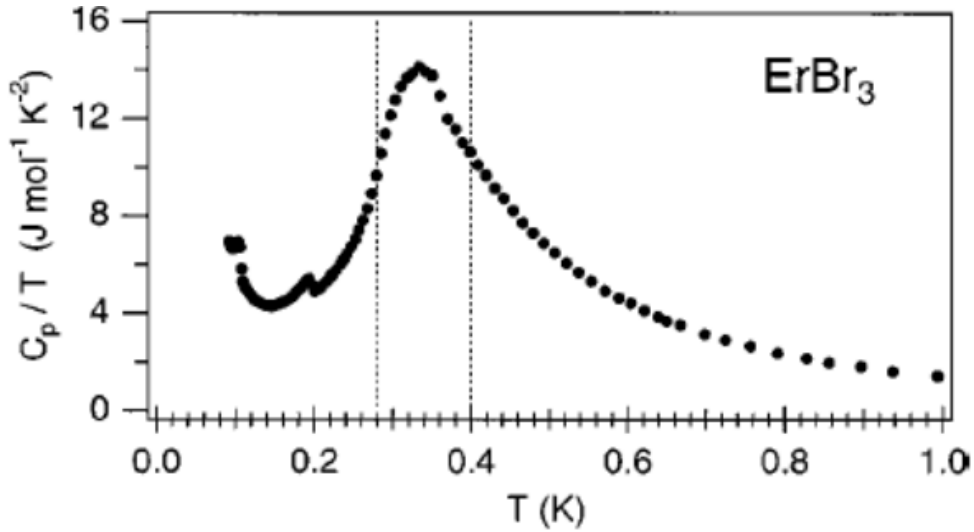


Fig. 23 | Specific heat of ErBr₃. There is a peak in C_p at the temperature of $T \approx 330$ mK. The Figure is adapted from Ref. [72].

Mertens *at al.* have calculated the spin-spin correlation function that corresponds to a gas of free vortices and its integrated intensity $I(q)$ above the critical temperature is given by [114, 115]

$$I(q) = \frac{S^2}{4\pi} \frac{\xi^2}{(1 + (q\xi)^2)^{-\frac{3}{2}}} \quad (18)$$

where q is the position of the central peak and ξ^2 is proportional to the inverse vortex density n^{-1} . Fig. 24 presents the inverse intensity of the peak obtained by fitting the magnetic scattering with Eq. 24. A fit of ξ^{-2} is shown together with the inverse intensity where ξ was assumed to follow Eq. 15. There is a good agreement with the theoretical prediction and the parameter $b = 1.28 \pm 0.07$ is comparable to the previously obtained value (see Fig. 22).

Another prediction for a BKT transition is the discontinuous jump of the spin stiffness constant at the critical temperature T_{BKT} [67]. Regrettably, the instrumental

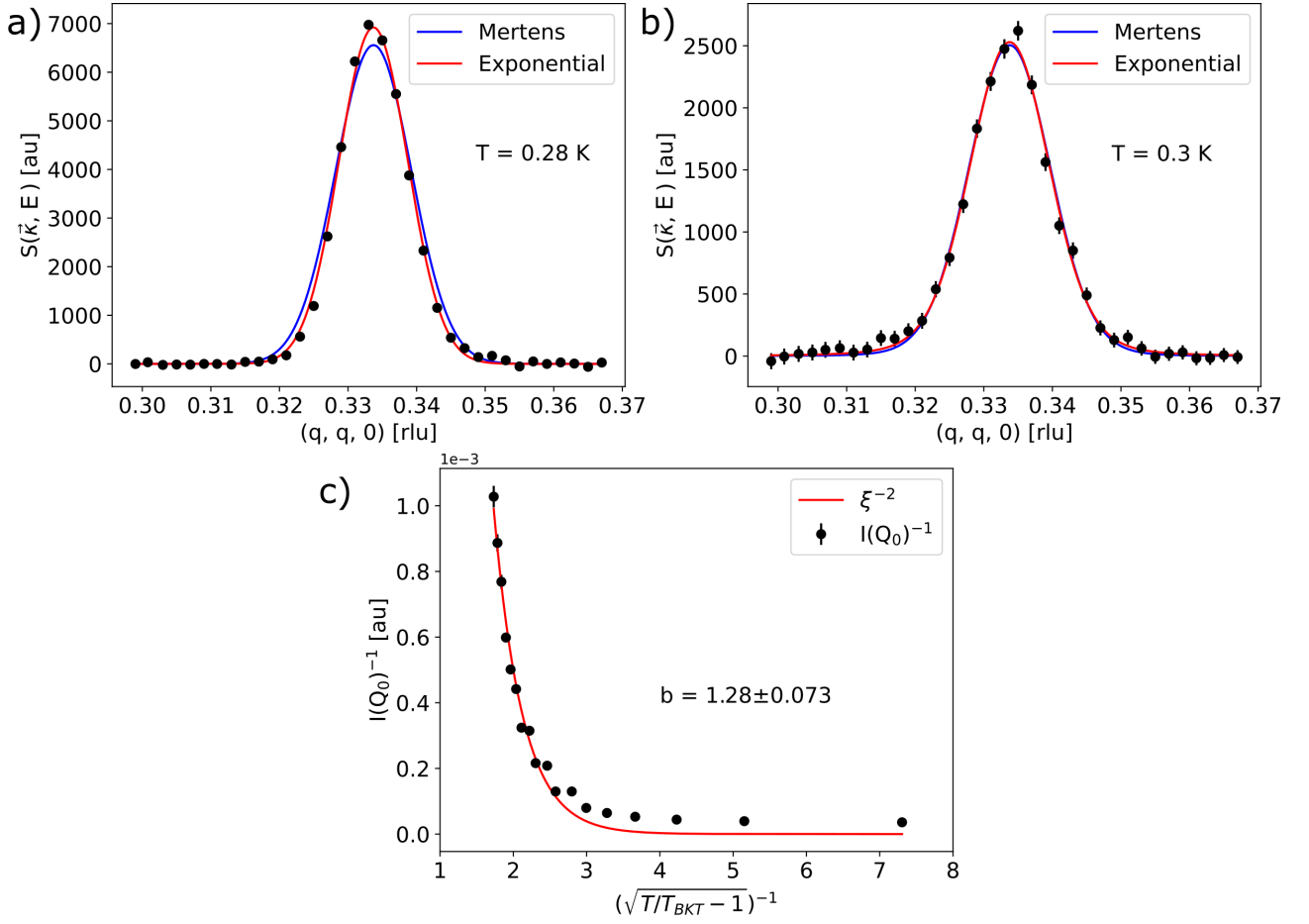


Fig. 24 | Temperature dependence of the neutron peak intensity above T_{BKT} . The magnetic peak is shown together with fits of Eq. 17 and 18 at temperatures **a**, $T = 280$ mK; **b**, $T = 300$ mK.

The intensity $I(Q_0)$ is obtained at the peak position from Eq. 18 and presented in **c**. The parameters used in Eq. 18 were obtained by fitting the neutron scattering with Eq. 18. $(\xi)^{-2}$ is plotted as comparison where the correlation length ξ was obtained from a fit to Eq. 15

resolution of the triple-axis neutron spectrometer is not sufficient to observe the jump in the spin stiffness in the spin-wave dispersion as shown in the following section.

5.3 Spin-waves in ErBr₃

The spin-wave excitations in ErBr₃ were measured with inelastic neutron scattering at $T = 80$ mK. The mean-field random-phase approximation (MF-RPA) method is applied to extract the exchange interactions from the spin-wave dispersion. Section 4.5 introduces the MF-RPA method as well as the Hamiltonian (Eq. 6) that only includes dipolar interactions which are sufficient to explain the magnetic ground-state. From the CEF measurement (see Fig. 12), the first excited CEF-level is at a much higher energy of 1.5 meV compared to the strength of dipolar interactions with ~ 0.02 meV at $\vec{k} = (1/3, 1/3, 0)$ and therefore ErBr₃ can be approximated by a $S = 1/2$ doublet. Naturally, the easy-plane anisotropy has to be taken into account, here, in the form of anisotropic g -factors as detailed in Section 4.5. The g -factors for ErBr₃ are found to be $g_x = g_y = 9.4$ and $g_z = 0.1$ from the CEF parameters.

Fig. 25a presents the measured inelastic neutron scattering of ErBr₃ along the high-symmetry direction $(0, q, 0)$, taken at $T = 80$ mK, together with the results from the MF-RPA calculations with dipolar interactions. In the experiment, the energy resolution was $70 \mu\text{eV}$, hence the low-energy excitation below $E < 0.1$ meV are hidden by the incoherent scattering at the elastic position [111]. The MF-RPA contains only one global scaling parameter to adjust the intensity to the observed scattering since the other parameters are determined by the experiments. The lattice parameters and magnetic moment of Er³⁺ were determined by neutron diffraction [72]. The experimental resolution was determined from the incoherent scattering. Fig. 25b compares the extracted spin-wave dispersion with the MF-RPA simulation throughout one full Brillouin zone. The extracted position of the dispersion matches well with the simulation.

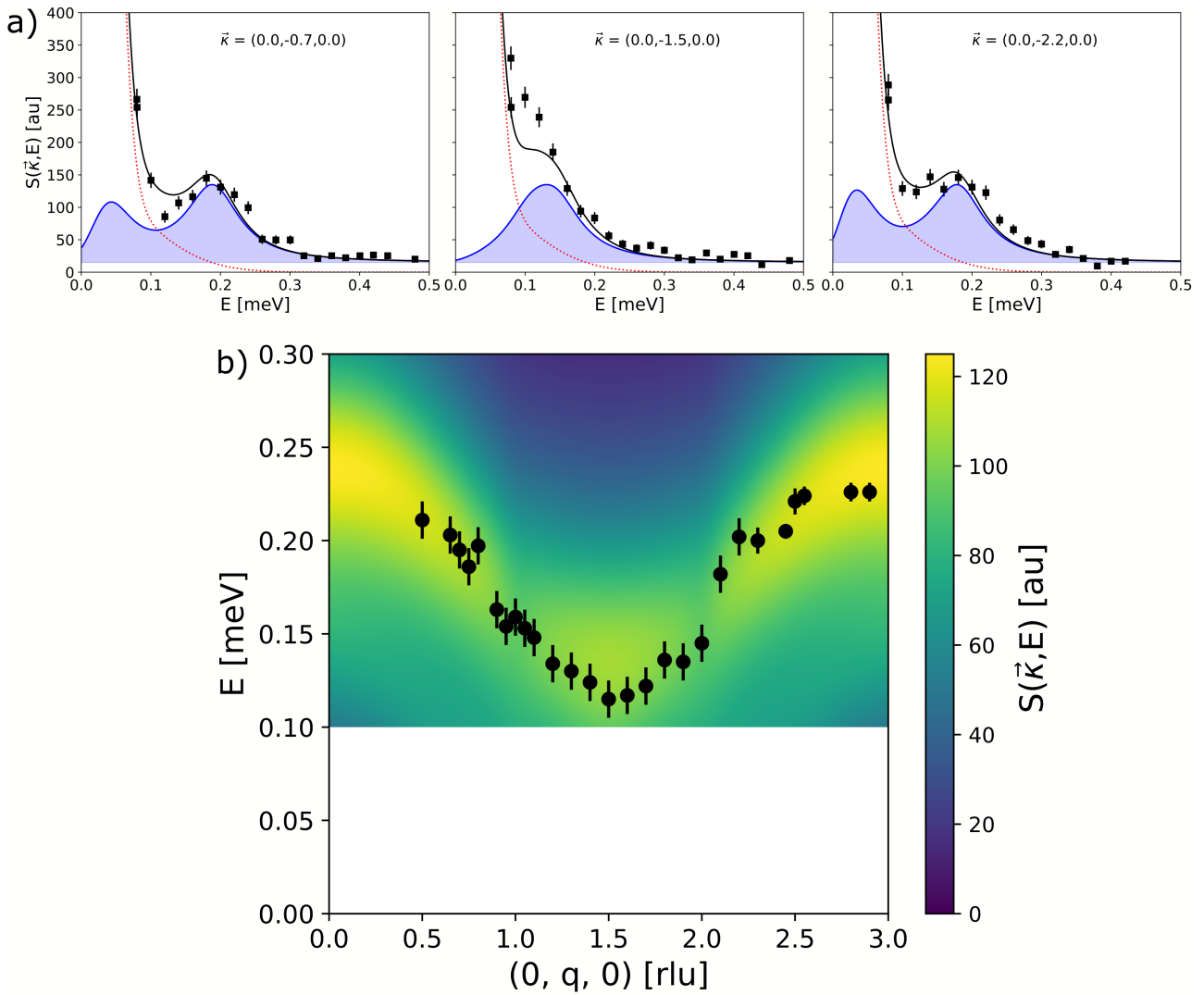


Fig. 25 | Inelastic neutron scattering along $(0, q, 0)$. **a**, Representative INS measurements of the spin-wave excitations in ErBr₃ compared with the result of MF-RPA (blue lines). The incoherent scattering is indicated by red lines. **b**, False color plot of $S(\vec{k}, E)$ along $\vec{k} = (0, q, 0)$. In the calculations, we used a linewidth $\epsilon = 0.07$ meV in the single-ion susceptibility to approximate the energy resolution of the spectrometer. The points represent the spin-wave dispersion measured in ErBr₃. Magnetic excitations below $E = 0.1$ meV were not accessible in the experiment.

A selection of different INS measurements along high symmetry directions together with MF-RPA simulations is shown in Fig. 26, including the high-symmetry points Γ , M and K . Similar to the previously investigated reciprocal positions, measurement and simulation are in good agreement over the whole extended Brillouin zone. Fig. 26c presents an overview of the extended Brillouin zone with the measurement points in reciprocal space as well as directions of the simulations. Altogether, the simulations and measurement are in good agreement with each other.

Only a single excitation is observable in the measurements. However, there are six spin-wave branches expected in ErBr₃ since the magnetic unit cell consists of six magnetic ions. As the magnetic ground-state is degenerate, the spin-wave disper-

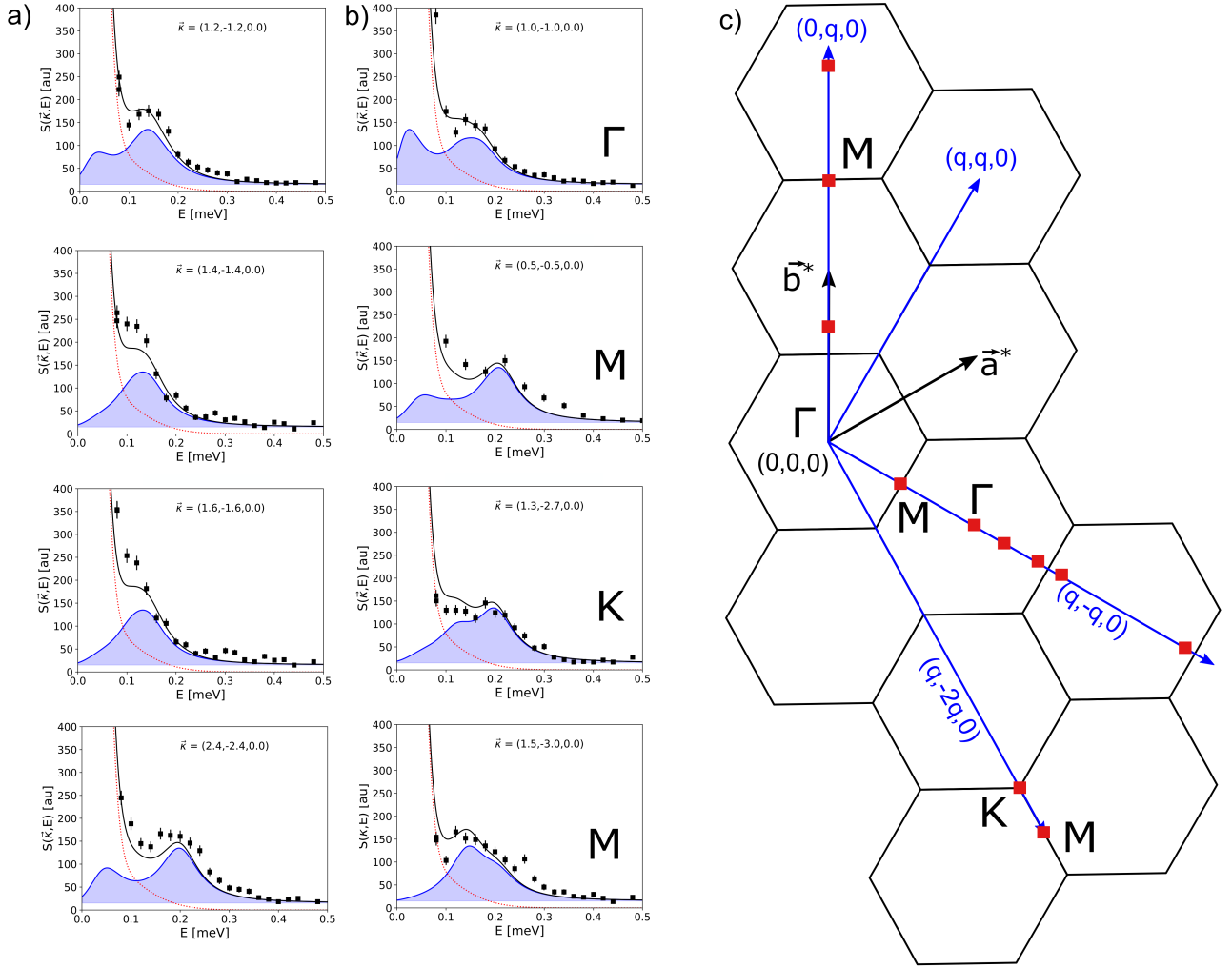


Fig. 26 | Inelastic neutron scattering in the extended Brillouin zone. **a**, Representative energy scans along the $(q, -q, 0)$ direction together with simulations of the inelastic neutron scattering extended cross-section shown as blue lines. The incoherent scattering is shown as red lines. **b**, As in **a** for Γ , M and K . **c**, Extended magnetic Brillouin zone showing the different scan directions of the measurements and simulations. The red squares indicate the positions in reciprocal space of the scans shown in Fig. 25a and Fig. 26.

sions were calculated along $(0, q, 0)$ for $\Psi = 0^\circ$ and 30° , see Fig. 27a and b. The resolution was set to $\epsilon = 0.001$ meV. Spin-wave branches in ErBr₃ are very close in energy so that resolving the single branches requires a resolution not available with triple-axis instruments. All six spin-wave branches are observable for both angles and it is apparent that the experimental resolution was not sufficient to resolve the separate branches. The optical branches around $E = 0.2$ meV form the spin-wave excitations observed in the INS measurement as shown in Fig. 25b. The acoustic and first optical branch change noticeably with Ψ whereas the dispersion of the higher branches remains largely unaffected by the variation of Ψ .

Fig. 28 presents the spin-wave stiffness W of the acoustic branch as a function of the angle Ψ . The spin-wave stiffness is the slope of the spin-wave dispersion close to the

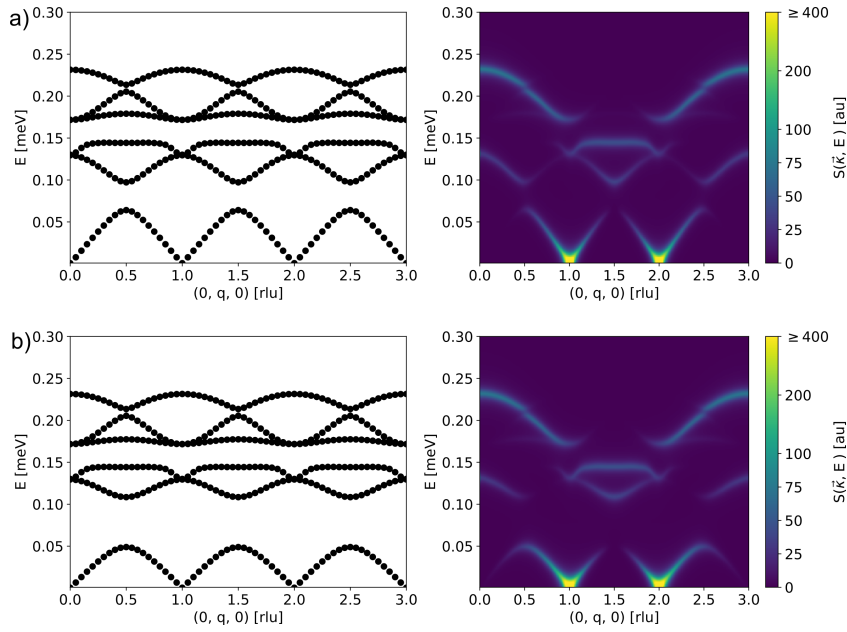


Fig. 27 | Spin-wave dispersion and excitations along $(0, q, 0)$. Dispersion of the spin wave excitations calculated with MF-RPA along $\vec{k} = (0, q, 0)$ for the easy-plane honeycomb lattice with dipolar interactions for **a**, $\Psi = 0^\circ$ and **b**, $\Psi = 30^\circ$. The color plots give the intensity of the inelastic neutron cross-section $S(\vec{k}, E)$.

Γ point [116]

$$\lim_{\vec{q} \rightarrow 0} E(\vec{q}) = W(\vec{q})\vec{q}.$$

From the calculations, it is observed that the spin-wave stiffness becomes soft at $n \times 30^\circ$ (n an integer). The six-fold symmetry present in the spin-wave stiffness agrees with previous theoretical calculations for the dipolar honeycomb antiferromagnet [117]. This creates an in-plane anisotropy that breaks the continuous symmetry of the ground-state [116].

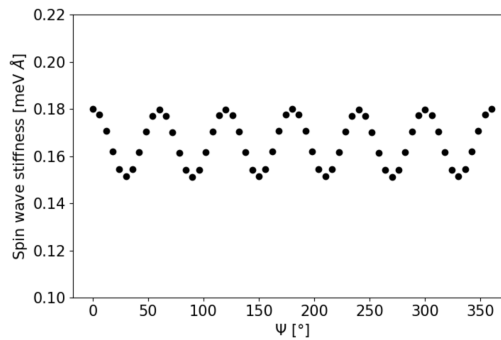


Fig. 28 | Spin-wave stiffness. Dependence of the spin-wave stiffness of the acoustic branch close to Γ as a function of Ψ .

5.4 Continuous degeneracy and Dirac cones

The previous section 5.3 established a model to describe the spin-waves in ErBr₃ and validated the results by comparison with the observed inelastic neutron scattering. It also became apparent that the excitations are located below $E \sim 0.25$ meV and are not resolved in their entirety. Previously, the high-symmetry direction $(0, q, 0)$ was simulated for different Ψ and the dispersion of the spin-waves were shown to be influenced by the magnetic structure of the Er-ions although the ground-states are all equivalent. However, the difference is quite small and mostly appears for the acoustic and first optical branch. The question is now, whether this remains true along another high-symmetry direction.

Fig. 29a presents the spin-wave simulations along $(q, q, 0)$ together with the respective spin structures defined by the angle Ψ . Similar to the previous direction $(0, q, 0)$, the degenerate ground-states produce different spin-wave dispersions. There is a 60° symmetry in the dispersion of the magnetic excitations but the respective spin structures are different. Particularly interesting are the K points where a Dirac cone appears in the spin-wave dispersion of the two lowest branches for $\Psi = 0$ and $\pi/3$ (see Fig. 29a top and bottom). Both angles correspond to a ring-like vortex structure but with opposite chiralities. The Dirac cone is replaced by an anti-crossing between acoustic and first optical branch if Ψ deviates from $n \times \pi/3$ ($n = 0, 1, 2, \dots$). Continuously increasing the value of Ψ from 0 also increases the gap size between the two lowest branches until $\Psi = \pi/6$. For higher values of Ψ , the energy gap decreases until a Dirac cone is formed at $\Psi = \pi/3$ (see Fig. 29b). Fig. 29c presents the spin-wave dispersion at the K point around the energy of the Dirac point $E \approx 0.083$ meV. In the vicinity of the K point, the dispersion of the magnetic excitations is linear when the acoustic and optical branch cross and form a Dirac cone .

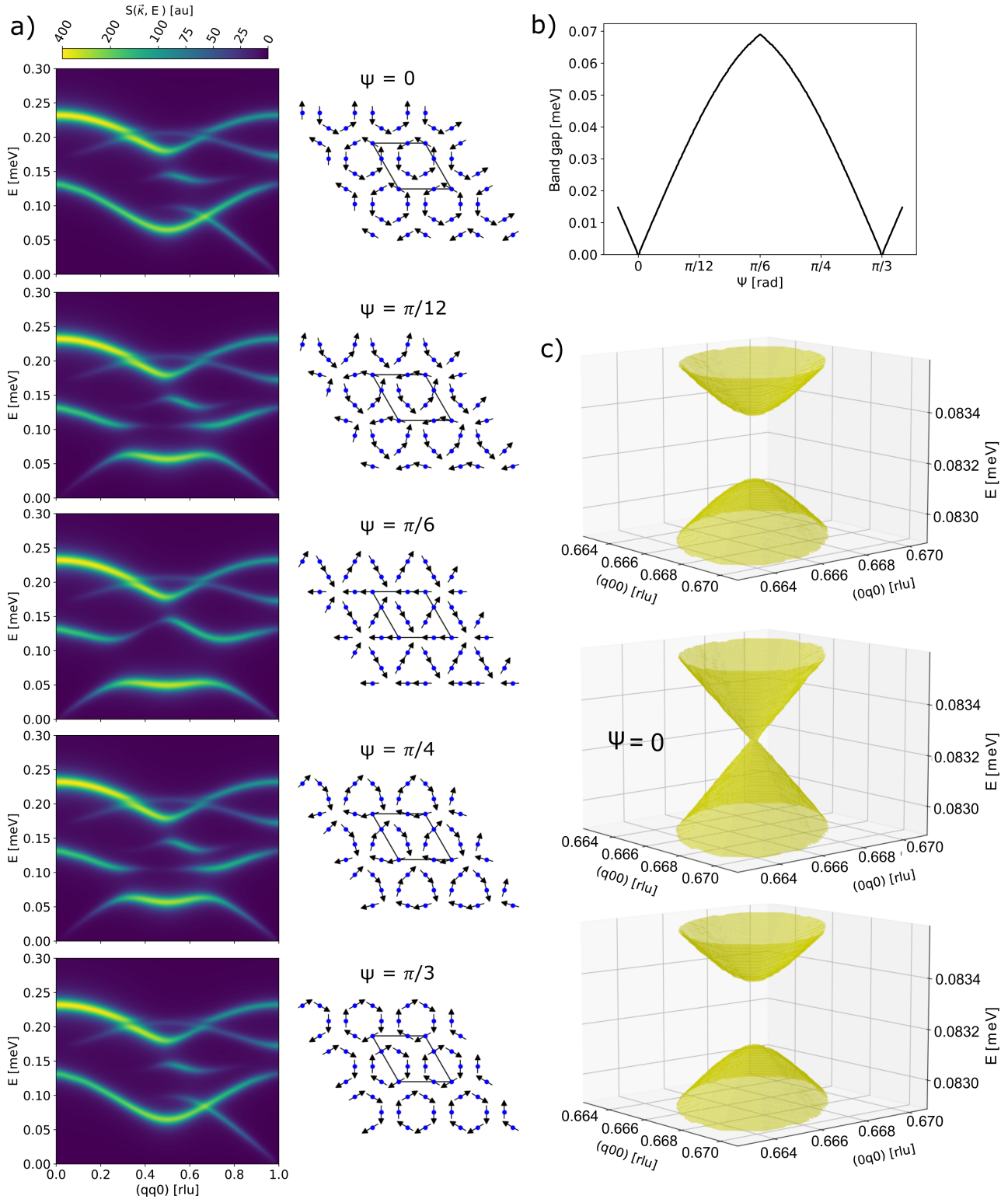


Fig. 29 | Dirac cones along $(q, q, 0)$ direction. **a**, Simulation of $S(\vec{k}, E)$ along $\vec{k} = (q, q, 0)$ for selected Ψ . Note the opening of a gap at $\vec{k} = (2/3, 2/3, 0)$ between the acoustic and the lowest optical mode at $E \approx 0.083$ meV when Ψ is varied. **b**, Dependence of the magnon band gap as a function of Ψ at $\vec{k} = (2/3, 2/3, 0)$. **c**, Calculation of the spin-wave dispersion close to the Dirac point for $\Psi = -5.6 \times 10^{-4}\pi$, 0 , and $+5.6 \times 10^{-4}\pi$, respectively.

5.5 Topological magnetic excitations in ErBr₃

The observation of Dirac cones in the simulations presented in the previous section are similar to the dispersion of the electronic bands in graphene [118, 119, 120]. Dirac cones are symmetry protected and have a Berry phase of $|\pi|$ in graphene [118]. Hence, the Berry phase γ of the spin-wave dispersion of ErBr₃ is calculated in the frame of the MF-RPA. Section 7.5 introduces the concepts of Berry phase, Berry curvature and Chern number as well as the method to calculate them.

The Berry phase is calculated to be $\gamma = \pm\pi$ when the spin structure allows the formation of Dirac cones. Fig. 30a shows the Berry phase at the Dirac points. The sign of γ alternates between neighboring cones in the Brillouin zone. With a non-trivial Berry phase in ErBr₃, it is natural to investigate the Berry curvature $\Omega(\vec{Q})$ and calculate the Chern number C . Topologically non-trivial systems are identified by non-trivial Chern numbers $C \neq 0$ and the Chern number can be calculated from the Berry curvature [121]. The Berry curvature of the acoustic branch in the whole Brillouin zone is shown in Fig. 30b for $\Psi = 5^\circ$. $\Omega(\vec{Q})$ is non-zero around the K - and K' -points. At these two distinct corner points, the Berry curvature has the same magnitude but opposite sign. Note that the Berry curvature diverges for $\Psi \rightarrow 0$. Overall, the Berry curvature decreases in magnitude and broadens with increasing Ψ until it vanishes at $\Psi = \pi/6$. With a further increase of Ψ , the Berry curvature reemerges but with opposite sign till it diverges again at $\Psi = \pi/3$. The evolution of $\Omega(\vec{Q})$ is illustrated in Fig 31. Hence, there is an interplay between the Berry curvature, spin gap and angle Ψ . The Chern number C is equal to zero when the Berry curvature is integrated over the whole Brillouin zone [111]. However, each K/K' point contributes $\pm 1/2$, respectively, to the Chern number C at $\Psi \approx 0^\circ$.

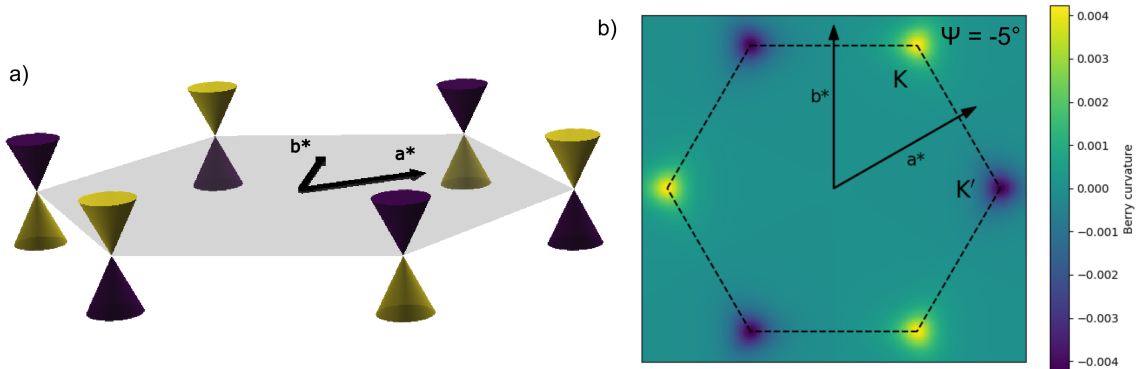


Fig. 30 | Berry phase and curvature in ErBr₃. **a**, The Berry phase associated with the Dirac cone ($\Psi = 0^\circ$) is either $+\pi$ (represented in yellow) or $-\pi$ (blue). **b**, The Berry curvature $\Omega(\vec{Q})$ in ErBr₃ is calculated for the acoustic magnon branch and $\Psi = -5^\circ$. The Brillouin zone is outlined with dashed lines. The calculation used a $N \times N$ grid with $N = 200$.

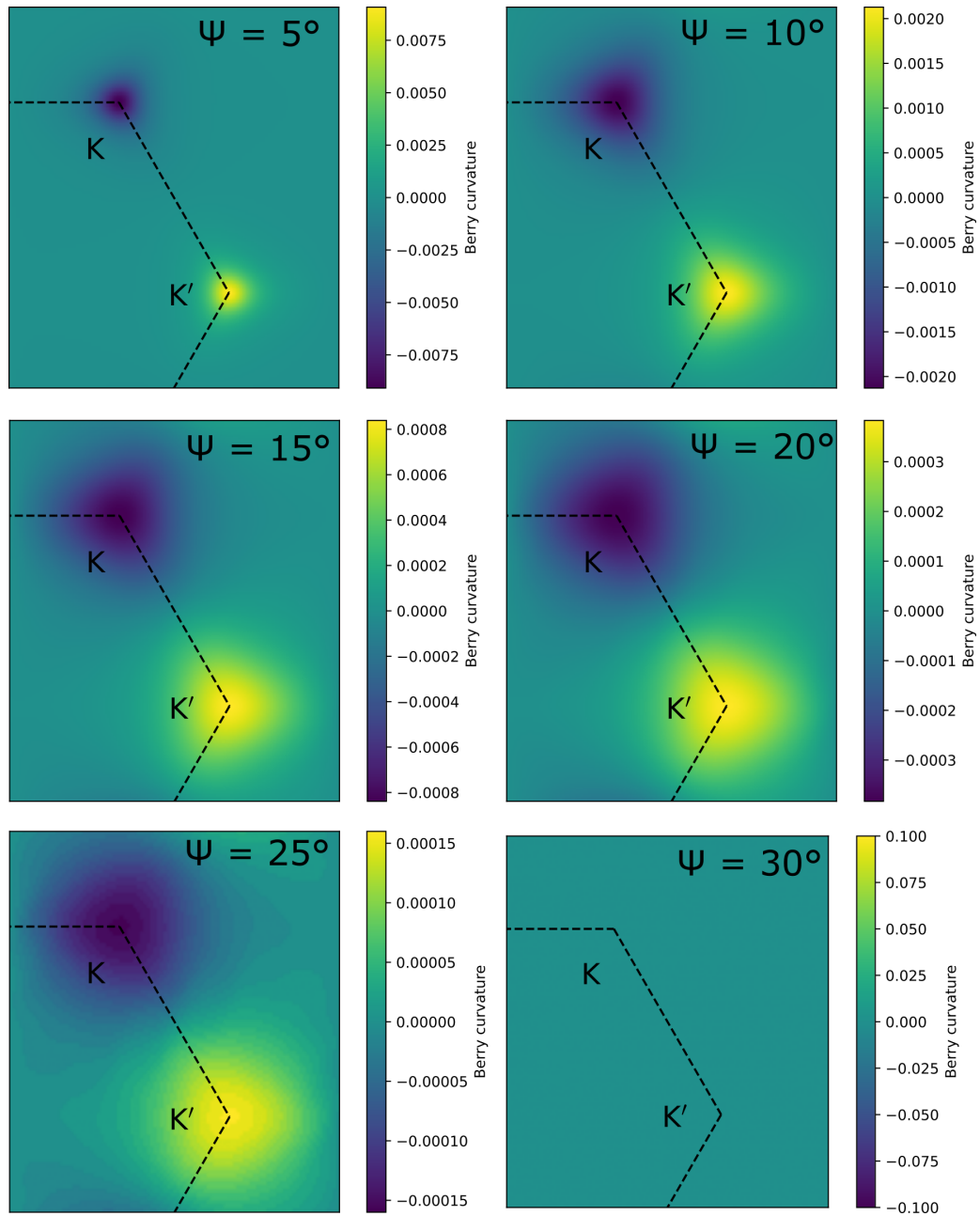


Fig. 31 | Evolution of the Berry curvature. The evolution of the Berry curvature as a function of angle Ψ is presented. The calculations used a $N \times N$ grid with $N = 100$.

5.6 Discussion of the results in ErBr₃

Graphene is the most commonly used example to feature Dirac cones in its electronic band structure at the corners of the Brillouin zone. Dirac cones come from the linear dispersion at the band crossing close to the K -point that is understood to behave like the dispersion of a relativistic and massless particle [118]. The magnetic equivalent to the electronic Dirac cones was predicted in the spin-waves of Heisenberg ferromagnets [119, 120]. Another magnetic Dirac material is the quasi-two-dimensional honeycomb ferromagnet CrBr₃ that contain topological magnons in the form of Dirac massless bosons [45]. Symmetry-protected topological magnons with magnetic Dirac cones in their spin-wave dispersion were also found in the 3D antiferromagnets Cu₃TeO₆ [122, 123, 124] and CoTiO₃ [47] that feature magnetic Dirac cones in their spin-wave dispersion. However, not all honeycomb systems exhibit Dirac cones. The spin-waves in CrI₃ show an anti-crossing with a spin gap at the zone boundary caused by the Dzyaloshinskii-Moriya interactions between next-nearest neighbors [125]. In magnetic materials, the DM interactions play the same role as the spin-orbit coupling in graphene and prevent the formation of Dirac cones in magnetic insulators. Essential is the bulk-edge correspondence [42] that allows an unobstructed and uni-directional propagation of the magnons along the surface/edges of magnetic topological insulators.

The previous section has shown that spin-waves for $\Psi \neq n \times 60^\circ$ (where n is an integer) in ErBr₃ have a similar topology as the electronic structure in graphene with broken inversion symmetry [126]. It appears that the invariance of the magnetic structure under combined time-reversal and inversion symmetry is necessary for the existence of Dirac cones as in Cu₃TeO₆ [122, 123, 124]. Dirac cones in the van der Waals crystal ErBr₃ originate solely from long-range dipolar interactions.

If the combined time-reversal and inversion symmetry of the magnetic structure is broken by changing Ψ , then a non-zero Berry curvature appears around the corners of the Brillouin zone. A finite Berry curvature with opposite signs appears at the K and K' points. Hence, the topology is trivial with a Chern number $C = 0$ when the Berry curvature is integrated over the whole Brillouin zone. However, the neighboring corners of the Brillouin zone contribute $C = \pm 1/2$, each corner having alternating sign. Neighboring peaks in Berry curvature with opposite sign are the origin of the quantum valley Hall effect [127, 128]. Magnon valley transport was already proposed for honeycomb ferromagnets mediated by a non-trivial Berry curvature [129, 130]. When the Chern number at K and K' changes sign and the spin gap closes for $\Psi = 0$, there is a topological phase transition in ErBr₃. In addition, the domain interface is expected to support the propagation of topological magnons since the Berry

curvature is anti-symmetric with respect to the transition point [131].

There is a Berezinsky-Kosterlitz-Thouless transition in ErBr₃ with a transition temperature $T_{BKT} = 270\text{-}280$ mK. Below the transition temperature, the magnetic structure factor is described by the Fourier-transform of a power-law function and the exponent η reaches the predicted value of $\eta(T_{BKT}) = 1/4$. Above the transition temperature, the Fourier-transform of an exponential function becomes appropriate to describe the neutron scattering data and the temperature dependence of the correlation length follows the expected exponential function with $b \approx 1.5$ as predicted by Kosterlitz [112]. In addition, the temperature of the peak in the specific heat at $T = 330$ mK that is higher than T_{BKT} in agreement with the theoretical predictions. The softening of spin-waves creates an in-plane anisotropy (see Fig. 27) and the continuously degenerate ground state changes to a ground-state with a six-fold discrete symmetry, which corresponds to the transition from the XY-model to the six-fold clock model both of which support the BKT transition [132].

In summary, ErBr₃ is a two-dimensional dipolar magnet on a honeycomb lattice with topological properties. This magnetic compound is particularly remarkable for the BKT transition and for its direct relationship between the Berry curvature and the continuous degeneracy of the magnetic ground-state defined by Ψ . The acoustic and optical branches form magnetic Dirac cones for specific vortex structures that evolves to a topological phase with non-trivial Berry curvature by modifying Ψ . Two different different topological phase transitions are found in ErBr₃. One is a phase transition that happens when the sign of the Berry curvature changes for different spin structures.

Future experiments on ErBr₃ may take advantage of the fact that the crystal can be easily cleaved. Another interesting possibility could be to create artificial lattices consisting of dipolar nano-magnets to create model systems to study interactions between spin domains. The specific relation between spin structure and magnetic excitations potentially allows to engineer magnonic devices with specific magnon band structures [133, 134] and could be explored with artificial systems.

5.7 ErBr₃: Experimental details

The single crystal of ErBr₃ was synthesized according to the method described in Ref [135]. The magnetic susceptibility was measured with a MPMS-5XL SQUID system (Quantum Design). The elastic scattering of ErBr₃ in the HL -plane was measured on the thermal neutron triple-axis diffractometer ZEBRA at PSI. The area detector was used together with a wavelength $\lambda = 1.1 \text{ \AA}$. The CEF splitting was determined with the thermal-neutron spectrometer Eiger at the SINQ spallation source. The spectrometer was operated in the constant final energy mode with $k_f = 2.662 \text{ \AA}^{-1}$. To maximize the intensity the monochromator was focused vertically and the analyzer was horizontally focused. With this configuration the energy resolution is about $\Delta E = 0.8 \text{ meV}$ at the elastic position. Contamination by higher-order neutron wavelengths was eliminated by a PG002-filter installed in the scattered beam. The dispersion of the magnetic excitations was measured with the cold-neutron three-axis spectrometer IN14 at the Institut Laue-Langevin. The spectrometer was operated in a similar configuration as for the previous measurements albeit with $k_f = 1.15 \text{ \AA}^{-1}$ which resulted in an improved energy resolution of 70 \mu eV . A cold Be-filter, that scatters off neutrons with wavevectors longer than $k_f = 1.55 \text{ \AA}^{-1}$, was used to reduce the background and avoid spurious scattering. For these measurements a single crystal of approximately 0.5 cm^3 was mounted inside a dilution refrigerator and cooled down to the base temperature of $T = 80 \text{ mK}$ which is well below the ordering temperature of the Er³⁺ moments. The investigation of the BKT phase transition was performed on the cold neutron triple-axis spectrometer TASP at SINQ (PSI). The instrument was operated with $k_i = 1.5 \text{ \AA}^{-1}$ and in diffraction mode. A cold Be-filter was installed in the beam to eliminate contamination by higher-order wavelengths. Collimators were used to improve the q resolution. For measurements at temperature mainly below T_{BKT} , the collimators were of 20° before the analyzer and 80° before the detector. For measurements above T_{BKT} , the collimator before the analyser was replaced with a 80° collimator.

6 YbBr₃: a 2D van der Waals system with partially disordered magnetic ground-state

Many modern technologies are based on quantum mechanical effects that hold further opportunities to develop future technologies like coherent quantum electronics [136]. In particular magnetic phenomena are inherently quantum in nature and possess potential for technological applications [51]. Promising research systems are two dimensional materials that may exhibit novel magnetic phenomena due to, in general, stronger quantum fluctuations than three-dimensional materials. If the quantum fluctuations are exceedingly strong, a disordered magnetic state with long-range quantum entanglement can appear that is highly sought after to be used in quantum communications [56, 137] and fault-tolerant quantum computing [69, 137].

Frustration between interactions in a magnetic system can be at the origin of enhanced quantum fluctuations that push the system towards complex and more exotic ground-states compared to static magnetic structures. Among the theoretically possible ground-states are incommensurate magnetic phases [138, 139, 140, 141, 142], locally ordered quantum states [142], called valence bond solids, as well as different types of quantum spin liquids [69, 138, 140, 141, 143, 144]. A related prediction is a special type of quantum phase transition, that is induced by frustration, where the magnons fractionalize in deconfined spinons [145, 146]. Competing interactions can significantly influence the dynamics of the spin excitations. The $S = 1/2$ frustrated antiferromagnetic square lattice is an example for a modification of the spin-waves by quantum dimer-type fluctuations that arise through the competition between nearest and next-nearest neighbor interactions [147]. These quantum fluctuations resemble the resonant valence bond (RVB) fluctuations that are predicted in the frustrated triangular lattice [53]. RVB states represent a type of quantum spin liquid which is expected to have a connection to high-temperature superconductivity [148].

Quantum spin liquids remain an elusive type of state since it is not only difficult to experimentally identify but also to find and understand appropriate model systems. Antiferromagnetic spin chains are one-dimensional quantum spin liquids due to the strongly reduced dimensionality and the thereby increased quantum fluctuations. Examples are the spin chains in KCuF₃ [149] and Cu(C₆D₅COO)₂ · 2D₂O [150]. Sufficiently strong quantum fluctuations are not present in higher dimensional systems without the support from frustration to form a quantum spin liquid state. There are different possible types of frustration in two- and three-dimensions. One is the geometric frustration inherent to the lattice that prevents a long-range ordering at low temperatures since not all bonds can be satisfied simultaneously. Geometric frustration is observed in kagome [151], triangular [152], spinel [153] and pyrochlore [154]

lattices. If the frustration does not arise from the geometry of the lattice, then another origin for the frustration can be the interactions. Not only the competition between interactions can increase quantum fluctuations but also if the interactions are anisotropic. Quite recently, the honeycomb lattice attracted a lot of attention due to the exactly solvable model of Kitaev that predicts a quantum spin liquid ground-state with bond-dependent anisotropic interactions [69]. α -RuCl₃ [71], Li₂IrO₃ [155] and H₃LiIr₂O₆ [156] are promising candidates to realize a Kitaev-type quantum spin liquid. There are other predictions that propose different types of quantum spin liquids in the honeycomb lattice commonly originating from frustration but the nature of the novel phases is still under discussion. The opinions vary between a type of quantum spin liquid [140, 141] to a plaquette valence bond state [142, 143, 144] with a variety of different magnetic excitations like spinons [142], rotons [144] and plaquette fluctuations [146].

The following part of my thesis details the investigation of the rare-earth trihalide YbBr₃ that belongs to the two-dimensional van der Waals compounds. YbBr₃ is a $S = 7/2$ antiferromagnet with an undistorted honeycomb lattice. Below $T \approx 3$ K, the system develops short-range correlations with a length comparable to the diameter of the honeycomb plaquette at $T = 100$ mK. Well-defined spin-wave excitations are observed in the inelastic neutron experiments although the correlation length is very short. In addition, a continuum was revealed above the well-defined excitations with the highest intensity at the Brillouin zone boundaries. The observations provide evidence for a quantum spin liquid state in YbBr₃ that is related to spin fluctuations on the honeycomb plaquette.

6.1 Magnetic structure, diffuse scattering and correlation length

The magnetic structure of YbBr₃ was measured on DMC at the temperatures $T = 100$ mK. This data set was subtracted by a data set measured at $T = 10$ K so that only the magnetic contribution is left. Fig. 32 shows a cut along $\vec{Q} = (h, 0, 0)$ through the representative magnetic structural peak $(1, 0, 0)$. The magnetic peak is broader than the experimental resolution of the instrument. The Full-Width at Half-Maximum (FWHM) is obtained by fitting a resolution-convoluted Lorentzian to the neutron intensity $I \propto \kappa^2/(q^2 + \kappa^2)$ where κ is the FWHM. The resulting correlation length is $\xi = 1/\kappa \approx 10$ Å at $T = 100$ mK what corresponds to the fourth nearest-neighbor distance of 10.66 Å or about 1.25 times the diameter of the Yb₆-hexagon plaquette [157]. Hence, the elastic neutron scattering data shows short-range magnetic order of the Yb³⁺ magnetic moments at $T = 100$ mK.

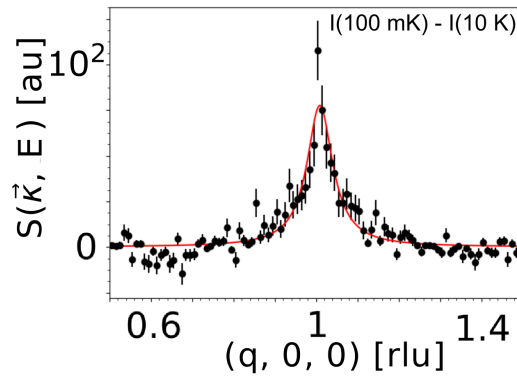


Fig. 32 | Magnetic diffuse scattering and correlation length. a, Cut through the diffuse scattering along the $(h, 0, 0)$ direction. The line is a fit to the data with a Lorentzian function convoluted with the instrumental resolution approximated by a Gaussian. (Note that the presence of paramagnetic scattering at 10 K leads to a negative background in the 100 mK data after subtraction) The Figure is adapted from Ref. [157].

Fig. 33a presents the experimental diffraction pattern of the diffuse magnetic scattering. There are no magnetic Bragg peaks observable demonstrating the absence of magnetic long-range order down to at least $T = 100$ mK..

The diffuse magnetic scattering is located at the center of the Brillouin zone corresponding to $(1, 0, 0)$ or equivalent vectors and the magnetic ordering vector is therefore $\vec{Q}_0 = (0, 0, 0)$, in agreement with mean-field calculations presented in Section 4.4. However, the correlations do not create intensity at all positions of Brillouin zone centers but lie on a larger honeycomb lattice where certain zone centers have no intensity like $(1, 1, 0)$. Possible spin structures are limited by \vec{Q}_0 to ferromagnetic (FM) and antiferromagnetic (AFM) ordering in 2D and 3D. As discussed in Section 4.4, the alignment of the spins depends on the competing influences of the dipolar interactions and easy-plane anisotropy. Therefore, this section takes in-plane

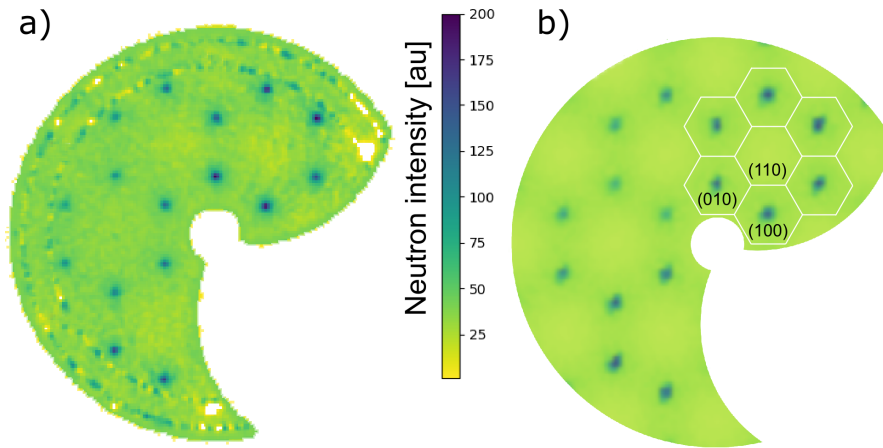


Fig. 33 | Magnetic structure and diffuse scattering. **a**, Magnetic diffuse scattering in YbBr₃ in the $[h, k, 0]$ plane at $T = 100$ mK, after subtraction of the nuclear Bragg contribution. **b**, Simulation of the magnetic scattering assuming a Néel antiferromagnetic ground-state where the spins are orthogonal to the c -axis. The calculations are based on the spin-wave-model considering exchange and dipolar interactions presented below. The Figure is adapted from Ref. [157].

as well as out-of-plane Néel order into account to investigate if the intensity distribution reveals information about the spin alignment. First, the spins are considered to be aligned parallel to the c -axis of the crystal and the corresponding magnetic structure factors as well as magnetic structures are presented in Fig. 34. It is obvious that the distribution of intensity is vastly different for the three-dimensional spin structures compared to the measured intensity distribution. A 3D FM shows a more sparse intensity pattern. Similarly, the 3D AFM does not reproduce the observed intensity distribution. Most striking is that the $(H, K, 0)$ plane has no intensity whatsoever and intensity only appears in the $(H, K, 1)$ plane (see inset of Fig. 34). The 2D FM ordering contains high intensity peaks where no intensity is observed in the experiment like $(1, 1, 0)$. Lastly, 2D AFM ordering reproduces the observed intensity distribution.

The same considerations are performed for the spins aligned orthogonal to the c -axis with the addition of spin domains differing by an angle of 120° between each other. Qualitatively, the results are the same as the previous ones for the magnetic structure with spins along the c -axis. Again, only the 2D AFM reproduces the correct distribution of magnetic Bragg peaks as shown in Fig. 33 and 34. Therefore, it is not possible to determine the spin direction from the intensity distribution alone.

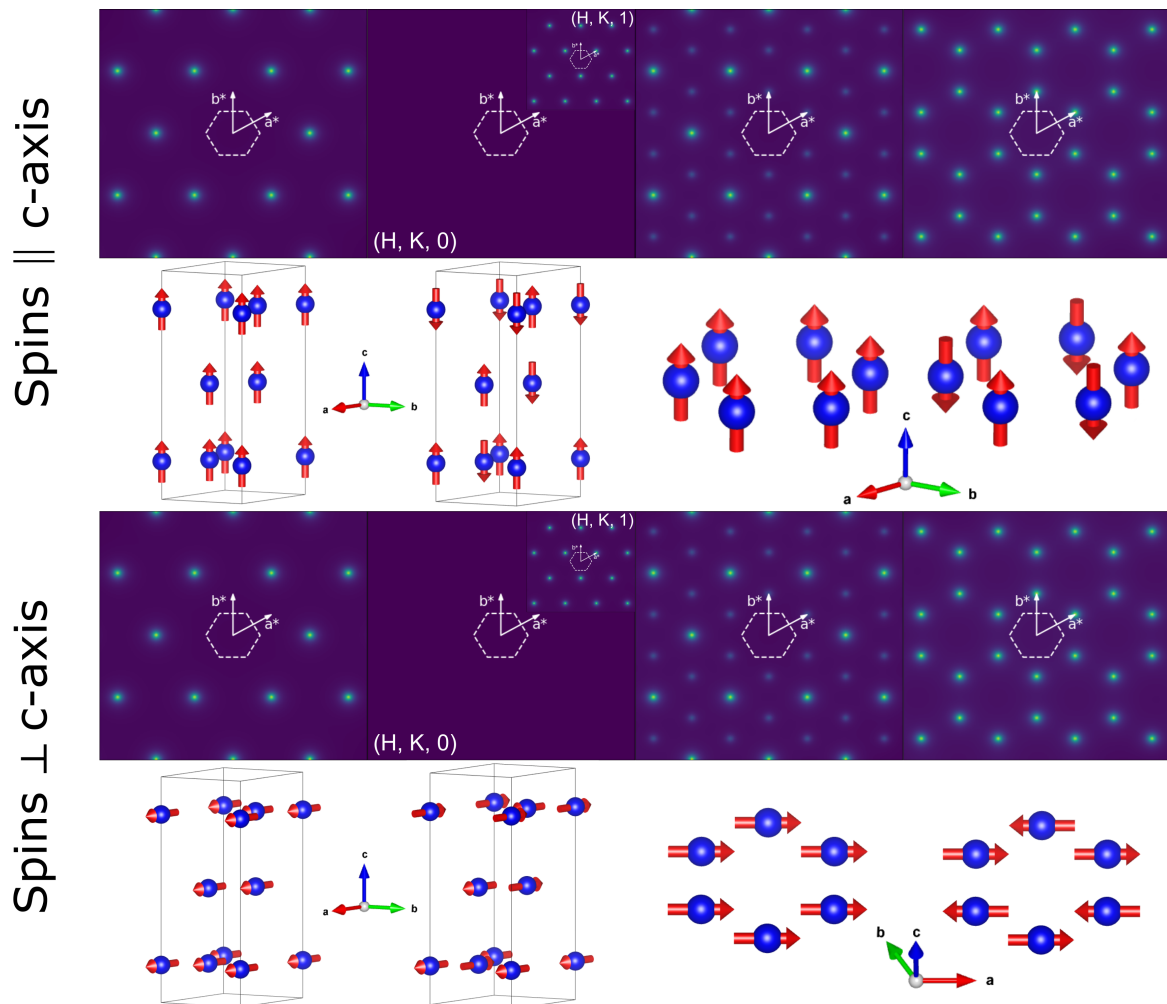


Fig. 34 | Calculated magnetic structure factor for different spin structures || and \perp c -axis. The normalized magnetic structure factors and magnetic structures are shown for the 3D FM, 3D AFM, 2D FM and 2D AFM magnetic ordering (left to right). The spins are aligned orthogonal to the c -axis of the crystal. **Upper row**, Simulation of the magnetic structure factor in the $(H, K, 0)$ plane. **Lower row**, Magnetic structure used in the simulation. Note that three spin domains are included in the calculations for spins || c -axis.

6.2 Inelastic neutron scattering and magnetic excitations

Inelastic neutron measurements were performed on a large YbBr₃ single-crystal on TASP at the SINQ of PSI. Three high-symmetry directions of the reciprocal honeycomb lattice were investigated at the temperature $T = 250$ mK. The directions are equivalent to the two reciprocal directions that transverse the M point of the Brillouin zone and the direction trailing along the edge of the Brillouin zone through the corner points K . Fig. 35 presents the spin-wave dispersions along the three high-symmetry cuts in the hexagonal plane. Along all three directions, there is only a single spin-wave branch observed of the two possible branches of YbBr₃.

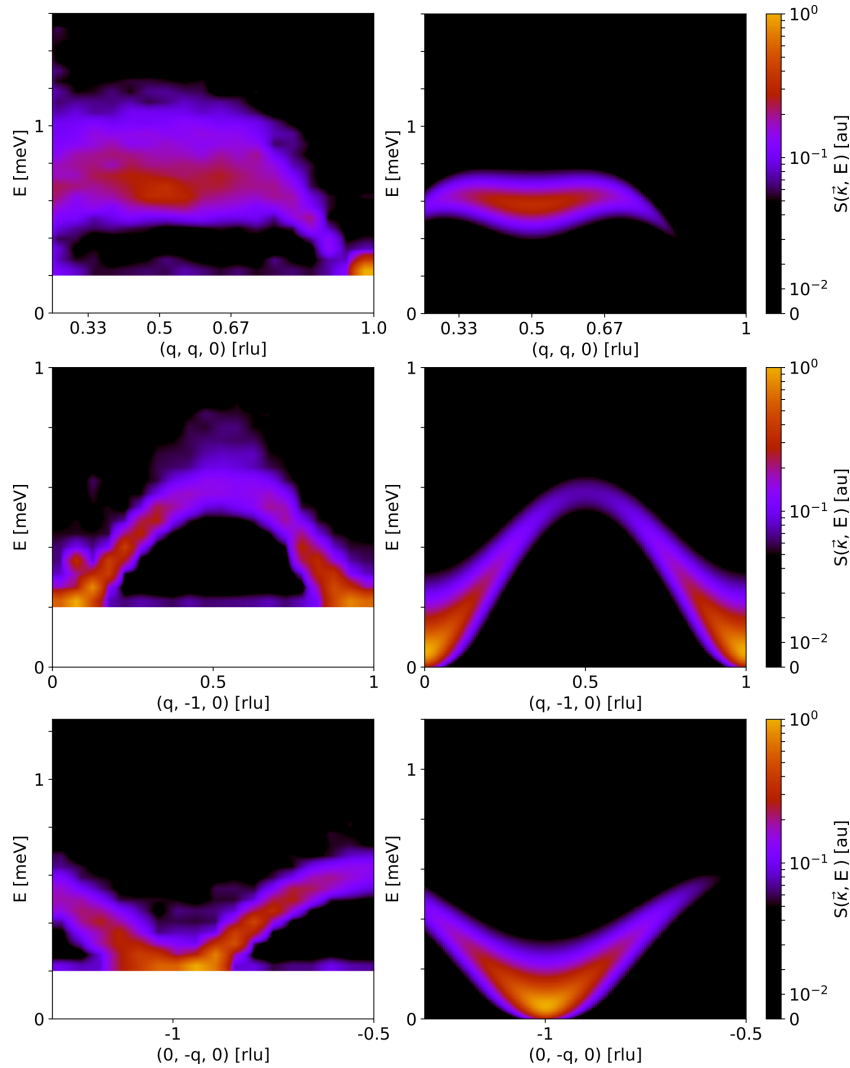


Fig. 35 | Magnetic excitations along high symmetry directions. False color plot of the observed (left) and calculated (right) inelastic neutron cross section of the magnetic excitations in YbBr₃ at $T = 250$ mK [157]. The intensity is shown on a logarithmic scale. Note the existence of a continuum of excitations around $(0.5, 0.5, 0)$ and $(0.5, -1, 0)$ which is not described by the spin-wave model.

Also, no spin gap could be detected at the zone center within experimental resolution.

Excitations at low energies are well-defined in energy and \vec{k} as shown in Fig. 35 and Fig. 36. Unexpected is the observation of the broadening of the high-energy excitations at the zone boundaries.

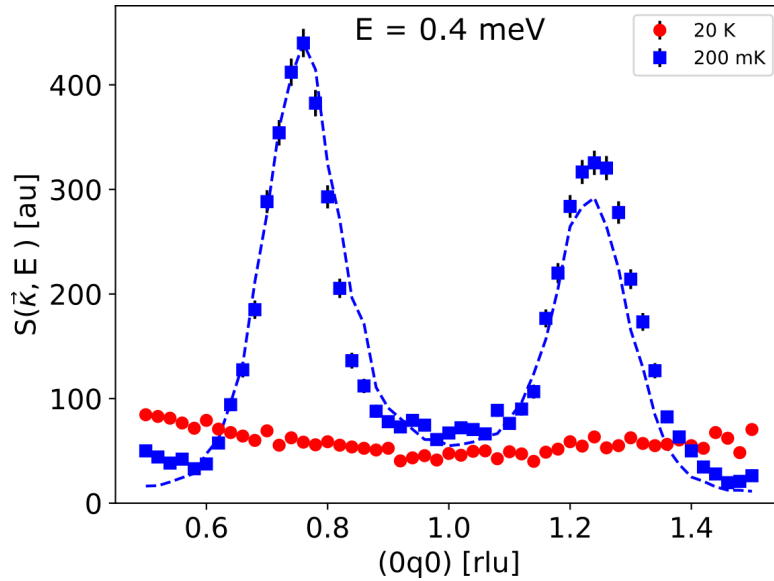


Fig. 36 | Excitations in the Brillouin zone center. Constant energy scan along the $(0, q, 0)$ direction at $E = 0.4$ meV. The dotted blue line is the resolution-convoluted simulation of the inelastic neutron intensity with the spin-wave model described in the text. The measurement at $T = 20$ K is shown in red as comparison.

6.3 Parameters of the model Hamiltonian

This section details the determination of the parameters of the Hamiltonian for YbBr₃. There is only a single spin-wave branch observable in the measurements (see Fig. 35). Hence, I assume initially that the model to describe the dispersion of the magnetic excitations is isotropic. The Heisenberg exchange parameters are obtained by a least-square fit of the spin-wave dispersions with the linear spin-wave theory model for the honeycomb antiferromagnet with nearest and next-nearest neighbor Heisenberg interactions (see Section 7.4). In the Néel ground-state, the ratio between the exchange interactions J_1 and J_2 is limited to $J_2/J_1 < 1/6$. The ratio J_2/J_1 measures the degree of frustration between the exchange interactions. Generally, frustration does not lift the degeneracy of the two spin-wave branches and there is also no spin gap opening with increasing frustration. However, the slope of the dispersion close to the Brillouin zone centers is strongly affected and changes from linear to quadratic behavior for larger ratios. It is noteworthy that the dispersions of the spin-waves are the same independent of the orientation of the spins, be it in-plane or out-of plane. The least-square fit provides the values $g^2 J_1 = -0.69 \pm 0.02$ meV and $g^2 J_2 = -0.09 \pm 0.02$ meV for the exchange interactions where g is the Landé-factors of the Yb³⁺ ion. With the exchange parameters, the spin-wave excitations are calculated with the MF-RPA and the Hamiltonian in Eq. 6 including the dipolar interactions and easy-plane anisotropy. Section 4.4 has shown that the dipolar interactions align the spins parallel to the c -axis on the honeycomb lattice without easy-plane anisotropy [84, 85]. Whereas dipolar interactions and easy-plane anisotropy result in an in-plane spin alignment if the easy-plane anisotropy is strong enough. Note that the magnetic susceptibility finds a strong easy-plane anisotropy in YbBr₃.

Fig. 37a presents the MF-RPA calculations of the energy gap size at Γ for different easy-plane anisotropies. Above $g_z/g_x = \Delta_{crit} = 0.985$, the spins are aligned along the c -axis and rotate into the hexagonal plane below this value. There is a spin gap expected for $g_z/g_x \geq \Delta_{crit}$ that closes at Δ_{crit} . Fig. 37b shows that there is no spin-gap observable within resolution and the linear fit of the dispersion finds 0 ± 0.021 meV as the size of the gap. Since there is no spin gap present, the easy-plane anisotropy has a lower bound of Δ_{crit} . However, there is also no optical branch observable and therefore, the easy-plane anisotropy has an upper bound close to Δ_{crit} as shown in Fig. 37a. Overall, the obtained parameters describe the low-energy excitations of YbBr₃ very well, qualitatively and quantitatively. But the easy-plane anisotropy obtained from the spin-waves is significantly smaller than expected from magnetic susceptibility and CEF measurements as can be seen from Fig. 38. Another open question is the origin of the continuum of spin excitations that is observed at the zone boundary.

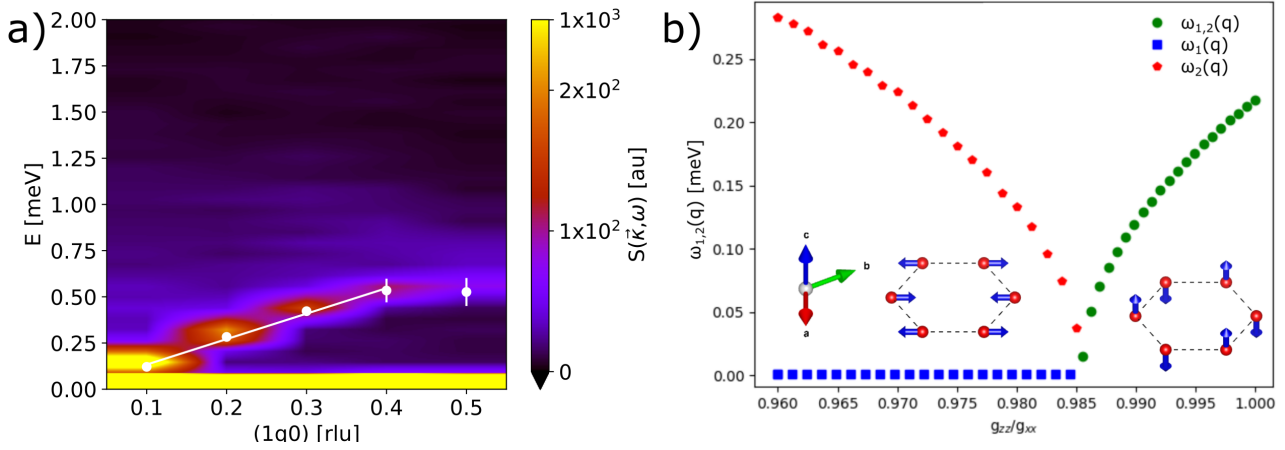


Fig. 37 | Investigation of a possible spin gap in the Brillouin zone center. **a**, Above a critical anisotropy $\Delta_{crit} = 0.985$, the calculated branches $E_1(\Gamma)$ and $E_2(\Gamma)$ are degenerate while for $g_z/g_x < \Delta_{crit}$ the two spin-wave branches split. All points are calculated with a precision of ~ 0.005 meV. The magnetic configurations shown in the Figure correspond to a Néel antiferromagnet with spins aligned along the c -axis for $g_z/g_x > 0.985$ and in the hexagonal plane for $g_z/g_x < 0.985$. **b**, map along $(1, q, 0)$ measured with $k_f = 1.15 \text{ \AA}^{-1}$. The line is a linear fit to the spin-wave and no gap is found with a calculated gap size of 0 ± 0.021 meV.

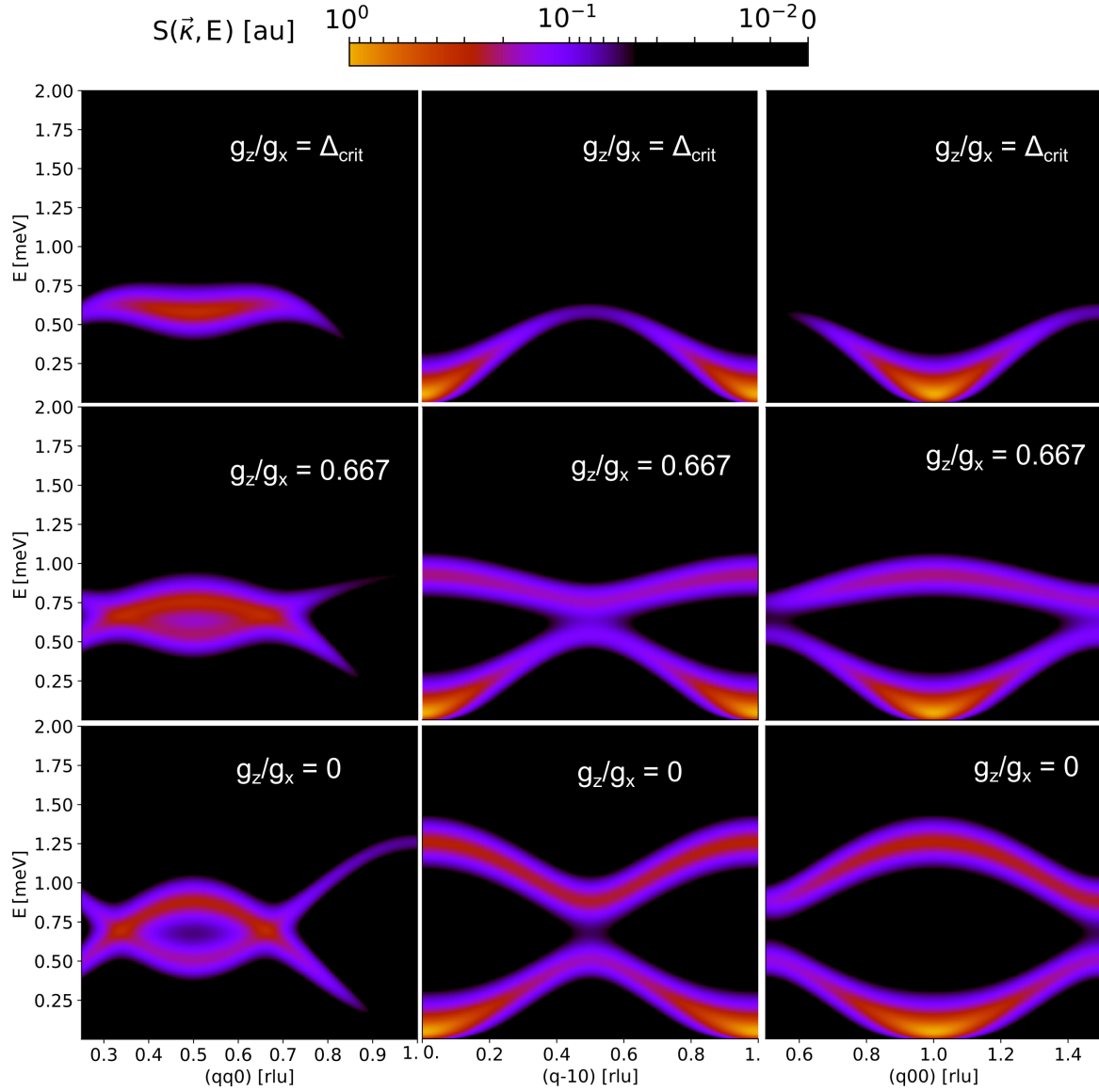


Fig. 38 | Influence of the easy-plane anisotropy on the spin-wave dispersion. Simulations of the measured inelastic neutron scattering along the high symmetry directions with the same exchange parameters as in Fig. 35 but with different anisotropies. **upper row**, $g_z/g_x = \Delta_{crit}$. **middle row**, $g_z/g_x = 0.667$. **lower row**, $g_z/g_x = 0$.

6.4 Continuum of excitations and its distribution

Broad excitations were observed along the $(q, q, 0)$ and $(q, -1, 0)$ direction in the inelastic neutron scattering measurements (see Fig. 35). In particular, the $(q, q, 0)$ direction features strong and broad excitations between the two corners of the Brillouin zone K and K' in reciprocal space. The magnetic excitations form a continuum that extends to about twice the energy of the well-defined magnetic excitations at the zone boundary. The continuum of excitations is observed near the M points at $(0.5, 0.5, 0)$ and $(0.5, -1, 0)$ where the magnetic excitations are present between $0.8 - 1$ meV. A different situation is observed at the M point along the $(0, -q, 0)$ direction, where it is difficult to distinguish broad excitations from the background. The continuum is weaker and less pronounced. All things considered, it is a surprising distribution of the continuum that warranted further investigation.

To study the continuum and its distribution in more detail, the inelastic neutron scattering was measured at a set of M points distributed over the extended Brillouin zone. Two sets of measurements were made at $T = 300$ mK and $T = 20$ K, respectively, to subtract the background in order to better determine the lineshape of the magnetic excitations. Fig. 39 presents the background subtracted INS at different M points. There is a significant amount of paramagnetic scattering present at $T = 20$ K and a direct subtraction of the high temperature measurements is not possible (see Fig. 39 insets). Hence, the background is assumed to be linear and was derived from the scattering above $E = 1.6$ meV and $T = 20$ K. All background subtractions were performed in this fashion. Nonetheless, the continuum is observable at all M points but with a significant reduction of intensity of about 20% for specific points as shown in Fig. 40a and its inset. Surprisingly, there appears to be two distinct kinds of M points with differing intensities that form a regular pattern in the extended Brillouin zone as shown in Fig. 40b. The pattern suggests that there are two types of Brillouin zones where one type only contains M points with weak intensity whereas the other type also contains M points with higher intensity alternating with weak intensity points along the edge of the zone.

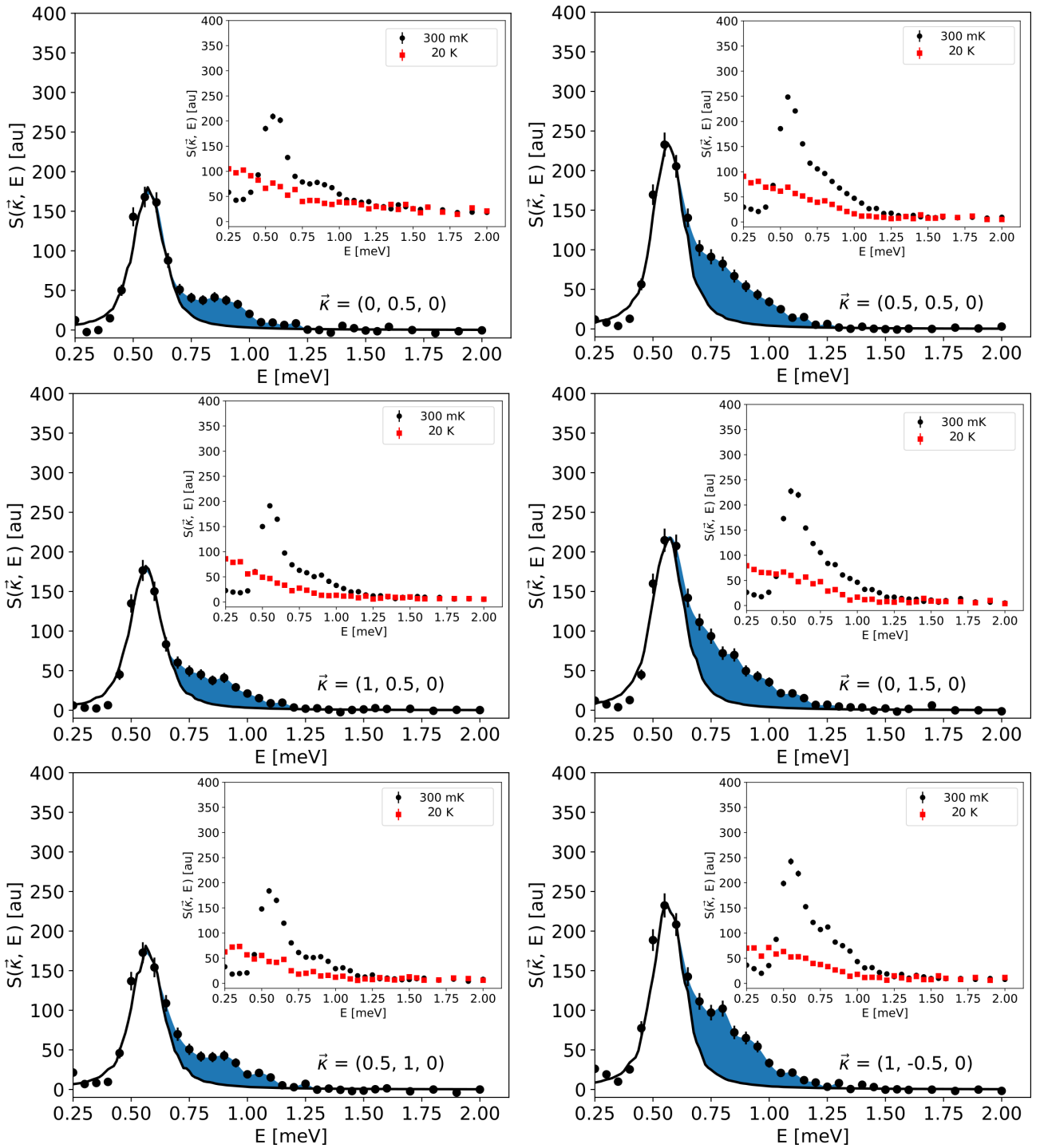


Fig. 39 | Continuum at M points spread over the extended Brillouin zone. The Figure presents the INS scattering at different M points. A linear background was subtracted from the $T = 250$ mK data by fitting the scattering of the $T = 20$ K data above $E = 1.6$ meV. The insets show the respective $T = 300$ mK and $T = 20$ K measurements. The lines are fits to the data with RPA-lineshape convoluted with the instrumental resolution. An intrinsic line-width of 0.1 meV was used for the simulation. The shaded area indicates the continuum of excitations.

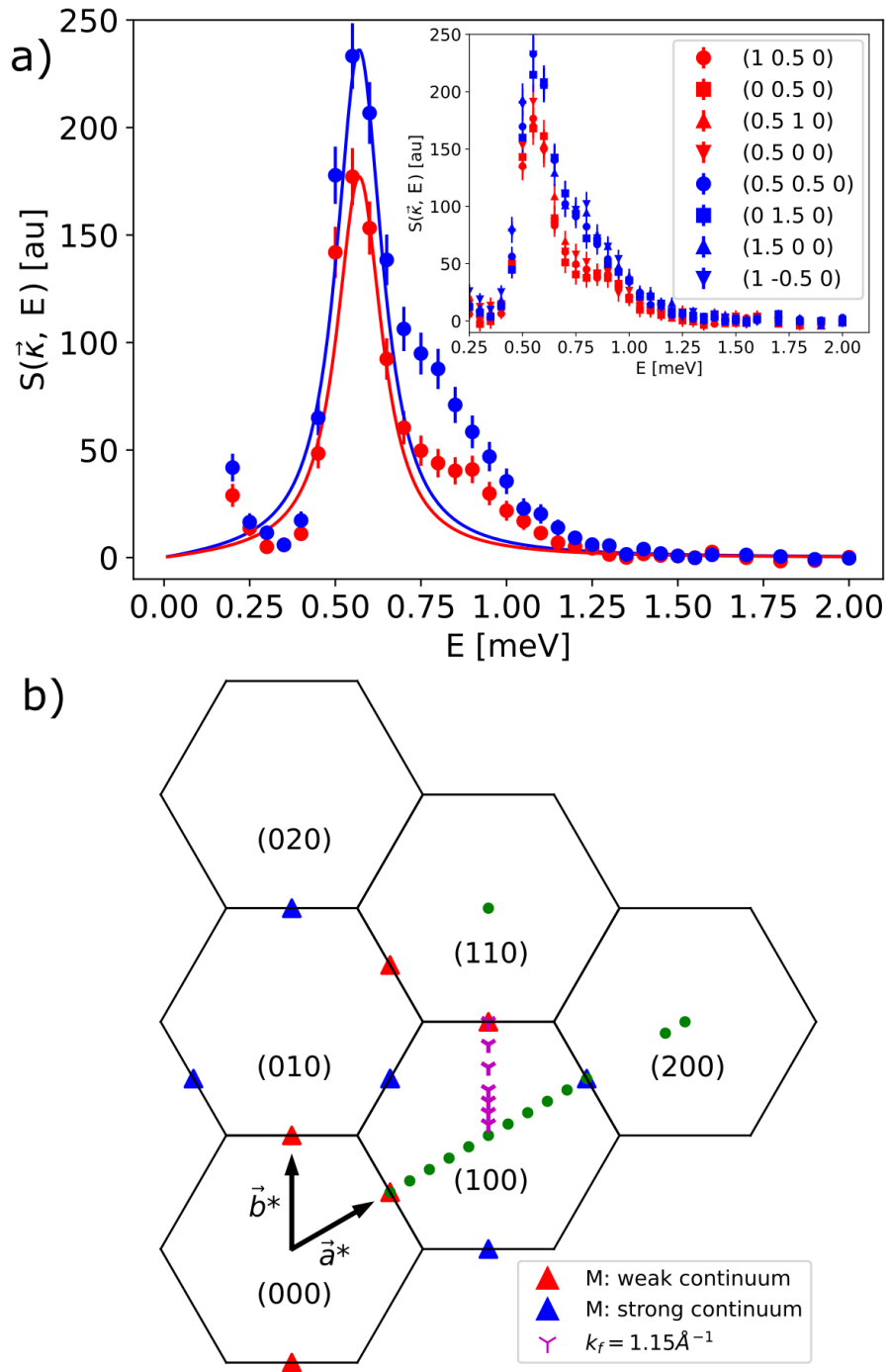


Fig. 40 | Continuum intensity at different M points. **a**, Average over equivalent M points for the two distinct types with different intensities. The lines are simulations of the spin-wave model explained in the text. The inset shows the M points used in the averages. **b**, Schematic of the extended Brillouin zone. The different M points are indicated in red (strong) and blue (weak). Green and magenta indicate measurements aimed to investigate the Brillouin zone center. The measurements were performed with $k_f = 1.3 \text{ \AA}^{-1}$ if not indicated otherwise.

So far, the continuum of excitations was mainly observed at the Brillouin zone boundaries. In order to investigate the q -dependence of the spin continuum, measurements were performed along high-symmetry direction $(q, 0, 0)$ from one end of the $(1, 0, 0)$ Brillouin zone to the other end as indicated in Fig. 40b. Above the sharp excitation, there is a broad continuum of spin excitations present across the whole Brillouin zone as shown in Fig 41a. The spin continuum extends to about 1.25 meV in energy. It has the highest intensity at the M points. However, there is a difference in intensity at different M points (see Fig. 42). In particular, the continuum is much weaker at the zone center as shown in Fig. 43 and has a similar magnitude and distribution as the measurements $T = 20$ K. Additionally, there is no spin continuum observable around Γ in a constant energy scan along the $(0, q, 0)$ direction at $E = 0.4$ meV. The lineshape of magnetic excitations is well reproduced by the simulation of the spin-wave model that takes into account the resolution of the instrument as shown in Fig. 36.

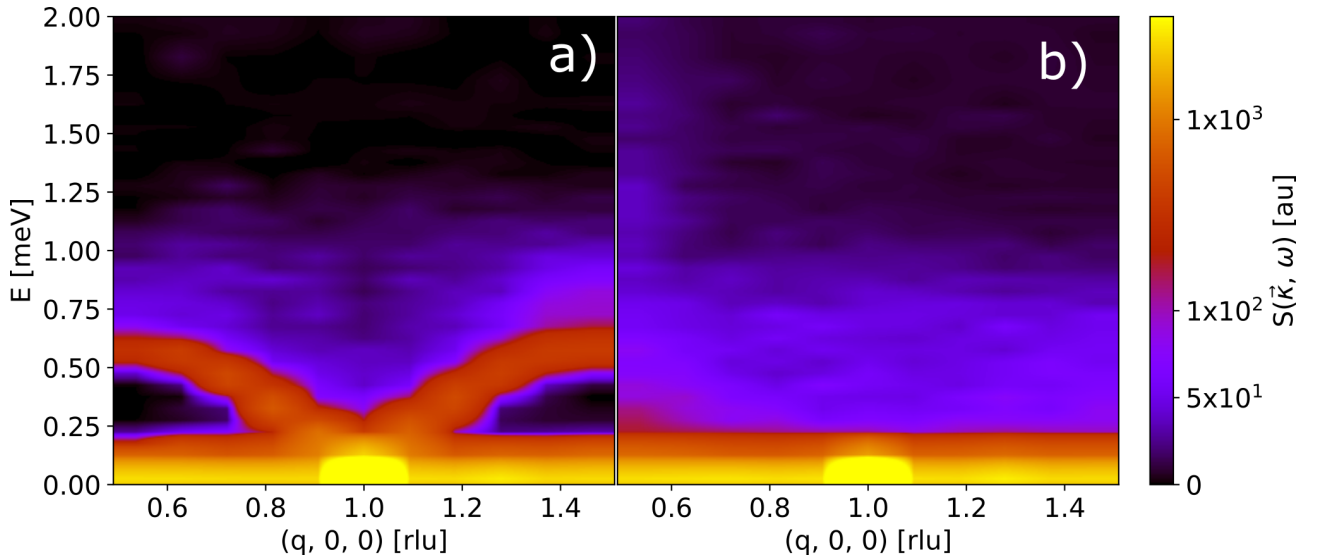


Fig. 41 | Continuum and paramagnetic scattering along $(q, 0, 0)$. **a**, Inelastic neutron scattering measured at $T = 300$ mK. A linear background was subtracted from the measurements as described in the text. **b**, Inelastic neutron scattering measured at $T = 20$ K. There is paramagnetic scattering present at all wave-vectors \vec{k} .

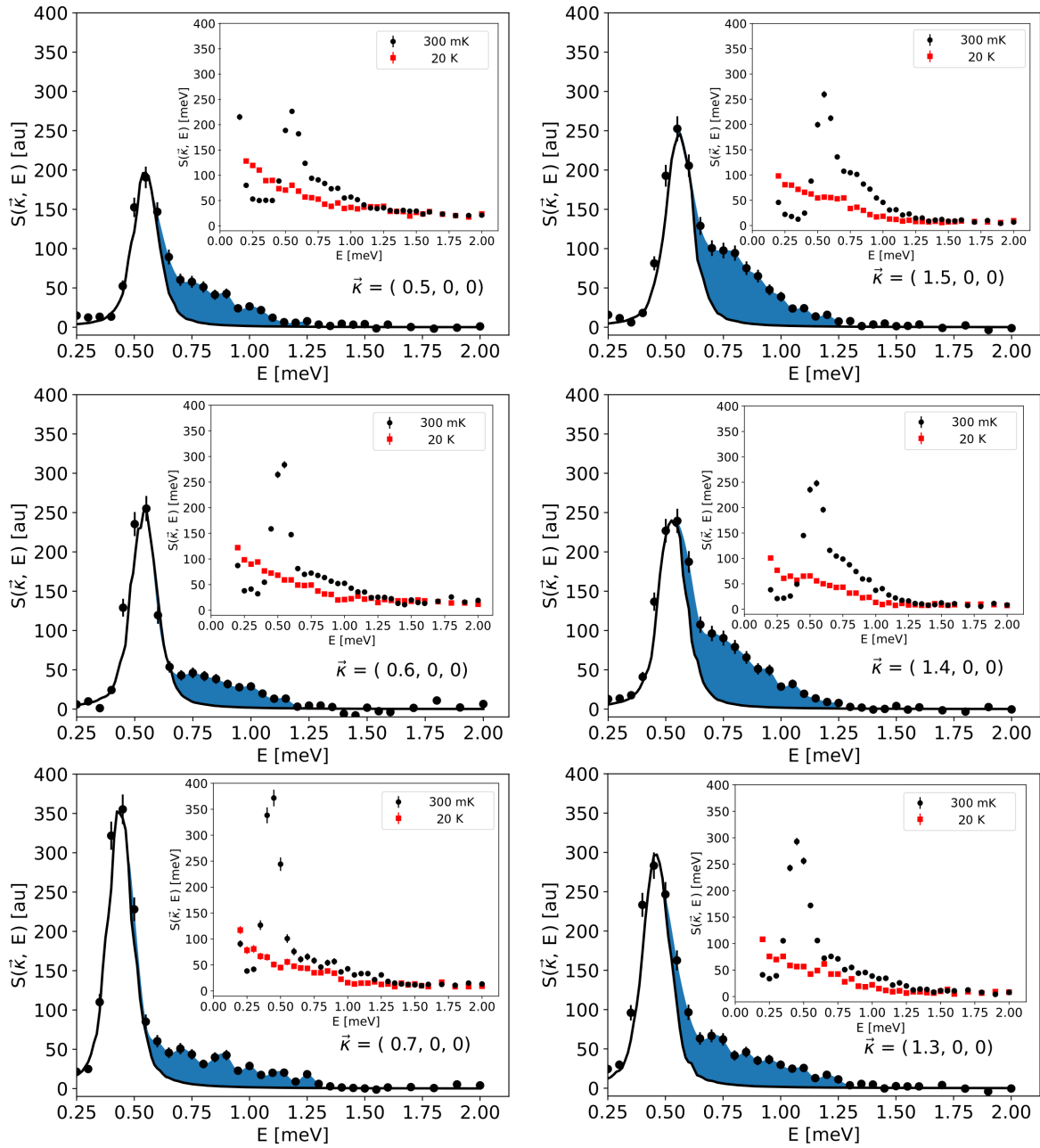


Fig. 42 | Inelastic neutron scattering along $(q, 0, 0)$. Background subtracted measurements along $(q, 0, 0)$ are presented together with similar fits as in Fig. 39. The insets show the respective $T = 300$ mK and $T = 20$ K measurements. The blue shaded area highlights the difference between measurement and fit.

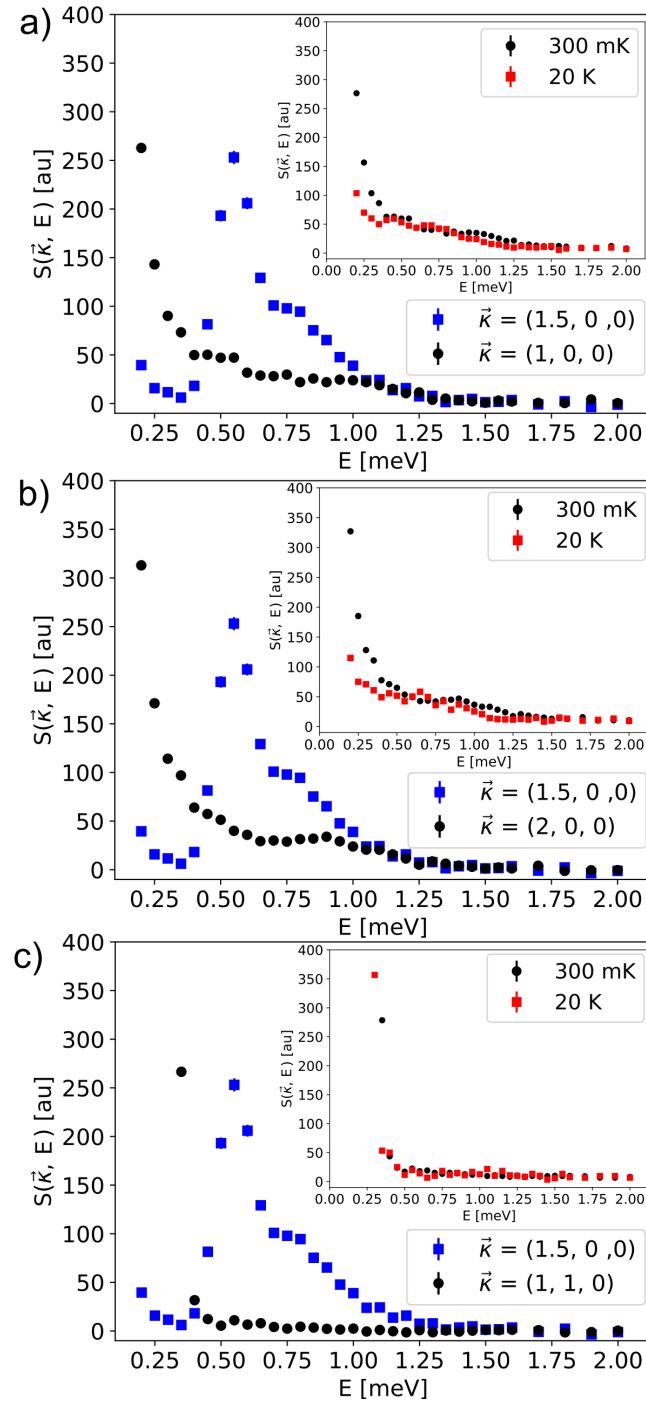


Fig. 43 | Continuum at the Brillouin zone center. Inelastic neutron scattering taken at $T = 300$ mK at the Γ points **a**, $(1, 0, 0)$, **b**, $(2, 0, 0)$ and **c**, $(1, 1, 0)$. The linear background was subtracted as discussed in the text. The insets show the respective measurements at $T = 300$ mK and 20 K without subtraction.

6.5 Possible origins of the spin continuum

This section aims to discuss different theories that provide possible explanations for the continuum excitations observed in YbBr₃. The instrumental resolution can broaden the lineshape of the excitations. To investigate this possibility, the convolution of experimental resolution with the spin-wave model was simulated with the Takin software utilizing the Popovici method [158]. Fig. 39 and 42 show the simulated lineshapes together with the difference to the measured intensity highlighted in blue. It is unambiguous that the lineshape of the inelastic neutron scattering data cannot be explained by the instrumental resolution.

Two-magnon decay may lead to a broadening of the lineshape of the magnon lineshape. But such a decay requires cubic anharmonicities that are not present in collinear magnets [159] and therefore cannot be responsible for the spin continuum observed in YbBr₃. There are also two-magnon excitations that create a continuum of excitations like it was observed in YbCl₃ [160]. A major difference to the observed excitations in YbBr₃ is the continuum in the zone center (see Fig. 44). YbCl₃ features a strong continuum at the Γ point. In contrast to the results of YbBr₃ which show sharp spin-wave excitations for wavevectors close to the zone center.

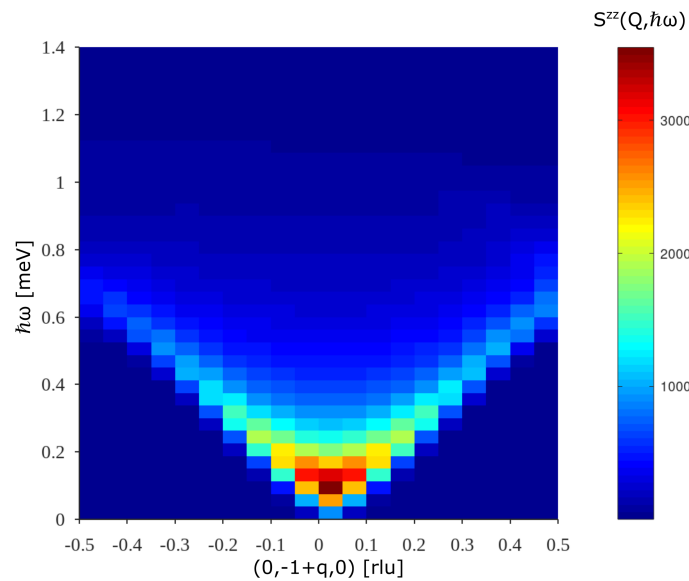


Fig. 44 | Two-magnon cross-section. The Figure shows the two-magnon cross-section of an Heisenberg Hamiltonian on the honeycomb lattice. An arbitrary cutoff is introduced in the dispersion to avoid the divergence of the two-magnon cross-section at the zone center. The Figure is taken from Ref. [157].

The exactly solvable Kitaev model [69] is a prominent theory for the honeycomb lattice to explain quantum spin liquids. However, YbBr₃ does not show any evidence for anisotropies in the exchange interactions that are essential for the Kitaev model. Therefore, it is not applicable in YbBr₃.

Schwinger-Boson [140, 161] and modified spin-wave [164] theory result in a disordered ground-state, in contrast to linear spin-wave theory, by enforcing a net-zero staggered magnetization to fulfill the Mermin-Wagner theorem at finite temperature. The results for the two theories are equivalent on the mean-field level [165, 166]. Both theories renormalize the exchange parameters and predict the same magnetic neutron cross-section that consists of two-magnon excitations (see Fig. 44). The two-magnon intensity at the zone center is calculated to be high but the observed intensity in YbBr₃ is weak at these wavevectors.

The spin fluctuations on the honeycomb plaquette are probably essential to understand the magnetic properties of YbBr₃ since the ground-state is only short range-correlated. In that respect, the approach of interacting honeycomb plaquettes appears interesting [143]. The ground-state is predicted to be the plaquette resonating valence bond state that has characteristic peaks in the structure factor at the M points of the smaller plaquette Brillouin zone. However, such peaks were not observed in the excitations of YbBr₃ at the corresponding wavevectors of the honeycomb Brillouin zone.

The inelastic neutron measurements in YbBr₃ show similarities with Monte-Carlo calculations for the frustrated honeycomb lattice with competing exchange interactions J_1 and J_2 [144]. The dynamical structure factor has an enhanced intensity due to a deconfined two-spinon continuum resulting from the proximity to a quantum critical point [167]. At the transition point itself, a quantum spin liquid phase is present. The Brillouin zone center at the Γ point shows a weak continuum that extends to twice the maximum of the spin-wave dispersion. There are different intensities predicted for the Γ and Γ' points where the latter does not exhibit a continuum. Along the edges of the Brillouin zone the continuum is predicted to have the highest intensity similar to what is observed in YbBr₃. The calculations in Ref. [144] predict a roton minimum in the magnetic excitations for large ratios J_2/J_1 that was not observed in the measurement of YbBr₃.

Here, I want to note that present theories neither include dipolar interactions nor easy-plane anisotropy what may be relevant to understand the spectrum of magnetic excitations of YbBr₃.

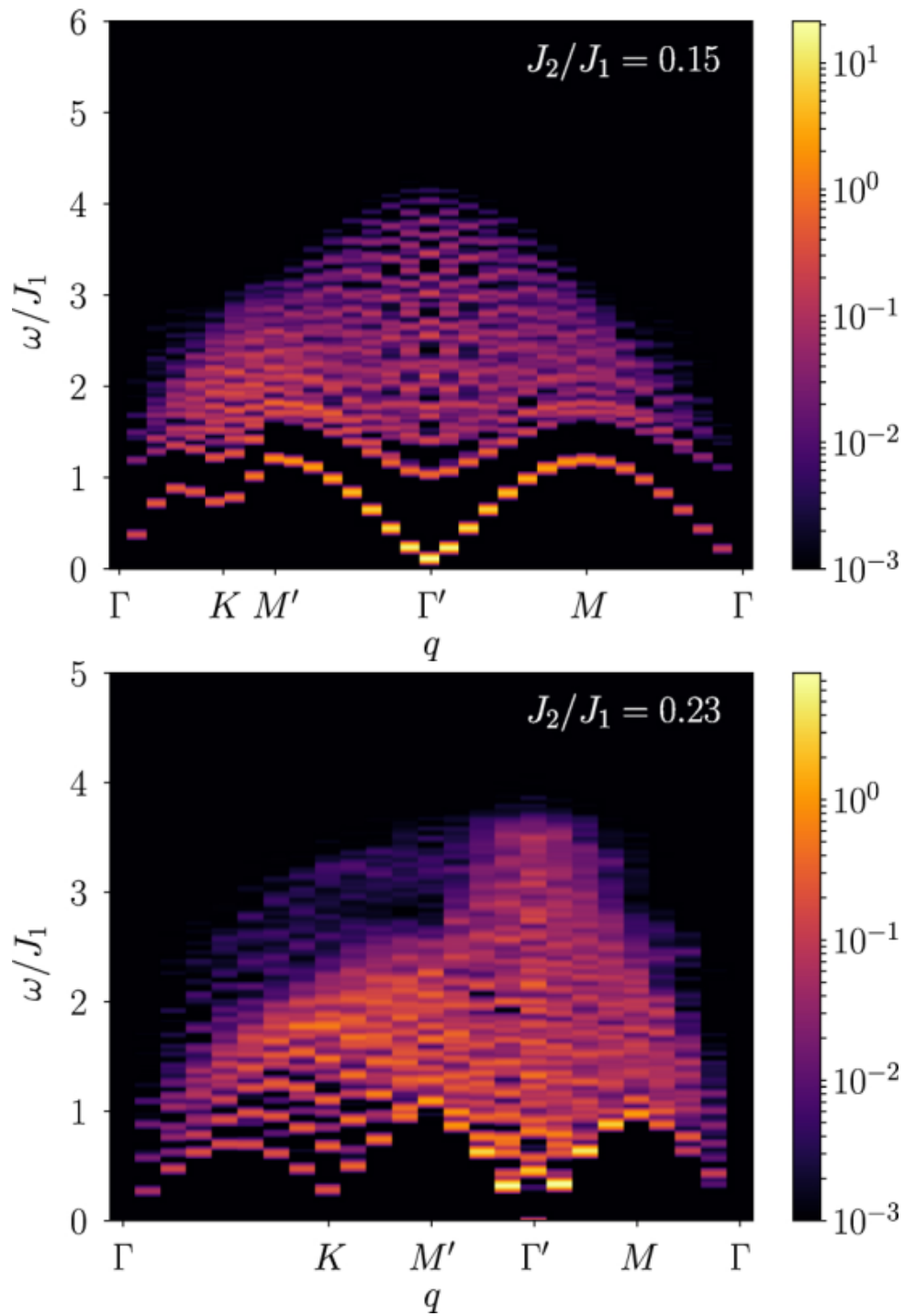


Fig. 45 | Dynamical structure factor simulation. The dynamical structure factor is shown for two different frustration ratios J_2/J_1 . $J_2/J_1 = 0.15$ corresponds to the Néel phase and $J_2/J_1 = 0.23$ is the value of the quantum critical point in this model. The smaller ratio is comparable to the value found in YbBr₃. The Figure is taken from Ref. [144].

6.6 Discussion of YbBr₃

YbBr₃ has a spin-wave dispersion that is well-described by a spin-1/2 Heisenberg Hamiltonian with frustration arising from the competition between nearest and next-nearest neighbors. The frustration ratio $J_2/J_1 \approx 0.13 \pm 0.03$. The extracted frustration is close to $J_2/J_1 \approx 0.16$ where the Néel phase becomes unstable [139]. Furthermore, quantum fluctuations inhibit long-range Néel order at the nearby ratio $J_2/J_1 \approx 0.1$ according to linear spin-wave theory [138, 164]. Larger ratios of J_2/J_1 are predicted by other theories, which would allow for a stable Néel phase up to the critical value of $J_2/J_1 \approx 0.2$. Those theories include the Schwinger boson approach [140], variational wave functions [144, 167] and exact diagonalization [142]. The absence of static magnetism in YbBr₃ indicates that the system is in close proximity to a quantum phase transition [157], but the models available in the literature do not include dipolar interactions and CEF anisotropy.

Dipolar interactions cannot be neglected in YbBr₃ since the magnetic moment is large. The spin-wave dispersion is gapped by the dipolar interactions with a spin gap size of $\sim 200 \mu\text{eV}$ [84] if there is no easy-plane anisotropy present. Additionally, the dipolar interactions align the spins along the c -axis. With increasing anisotropy, the spin gap size reduces and closes at the critical value $g_z/g_x = \Delta_{crit} \approx 0.985$. The spins align in the honeycomb plane for $g_z/g_x < \Delta_{crit}$. Consequently, the easy-plane anisotropy and dipolar interactions compete. Since the dispersion does not show a spin gap, the strength of the easy-plane anisotropy must be large enough to compensate for the effect of the dipolar interactions. In this region, quantum fluctuations are expected to be enhanced. This competition places YbBr₃ in the proximity of quantum critical point towards a QSL on the honeycomb lattice in terms of the easy-plane anisotropy [157].

Furthermore, the interplay between frustrated interactions and single-ion anisotropy is relevant for the order of the magnetic ground-state. The two-dimensional XY antiferromagnets on the square [162] and honeycomb [163] lattice are predicted to undergo a quantum phase transition towards a quantum disordered phase with increasing single-ion anisotropy as function of the frustration ratio. Interestingly, there is also a Berezinsky-Kosterlitz-Thouless transition predicted for antiferromagnets on the square lattice [162]. The critical temperature T_{BKT} depends on the interplay between frustration and single-ion anisotropy. A larger single-ion anisotropy leads to smaller T_{BKT} since the quantum fluctuations out of the XY plane increase. Hence, it is possible that YbBr₃ could support a BKT transition but the interplay between frustration and anisotropy places the system already in the disordered phase.

A central result for YbBr₃ is the observation of an excitation continuum above the well-defined spin-wave excitations in YbBr₃. However, there is no theory available that explains both the continuum and the observed short-range order. The correlation length between the magnetic moments in YbBr₃ is of the order 10 Å at $T = 100$ mK. Although, the Mermin-Wagner theorem only allows an ordered state at $T = 0$ K with an infinite correlation length in two-dimensional systems with short-range interactions [64], there is a finite correlation length at finite temperature. However, the correlation length measured in YbBr₃ is by two orders of magnitude smaller than the calculated correlation length at $T = 100$ mK for the unfrustrated ($J_1 = -0.69$ meV, $J_2 = 0$) Heisenberg model [166, 168]. As indicated by the short-range correlations, it is reasonable to assume that the fluctuations on the honeycomb plaquette play an important role. More evidence is provided by an RPA calculation for a hexamer plaquette that reproduces the intensity modulation of the continuum as shown in Fig. 46.

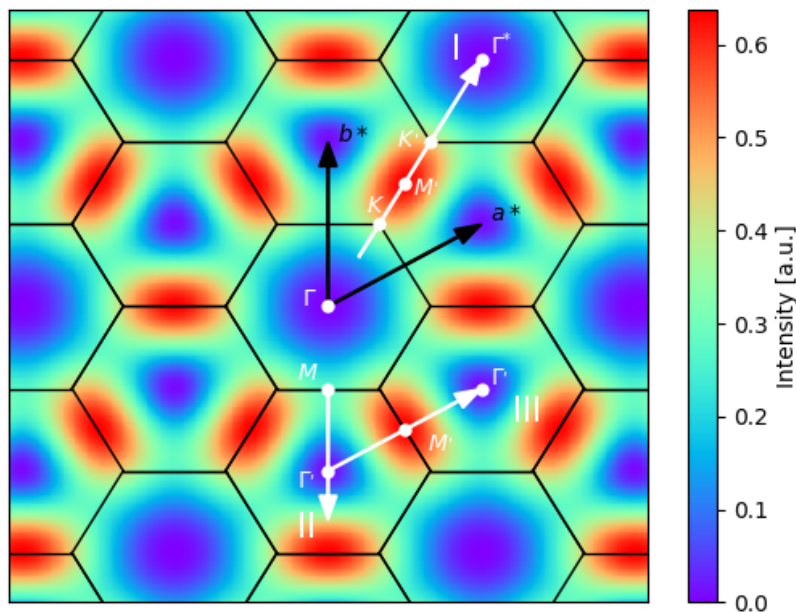


Fig. 46 | Calculated neutron form factor for a plaquette. The neutron form factor of an Yb₆ hexagon calculated within the random-phase approximation and assuming Néel order on the plaquette. The directions of the neutron measurement are indicated by white arrows: cut I corresponds to $(q, q, 0)$, cut II is $(0, -q, 0)$ and cut III is $(q, -1, 0)$. High-symmetry points are labeled similar to Fig. 35. Basis vectors of the reciprocal lattice are denoted as \mathbf{a}^* , \mathbf{b}^* . The Figure is adapted from Ref. [157].

Furthermore, this conclusion is supported by an analogous calculation of the magnetic susceptibility for a honeycomb hexamer based on the exchange parameters determined by inelastic neutron scattering. It shows a broad maximum at $T \simeq 4$ K similar to the measured magnetic susceptibility (see Fig. 47) [157]. These calculations provide evidence for local spin excitations in YbBr₃ at temperatures well below the maximum of the magnetic susceptibility.

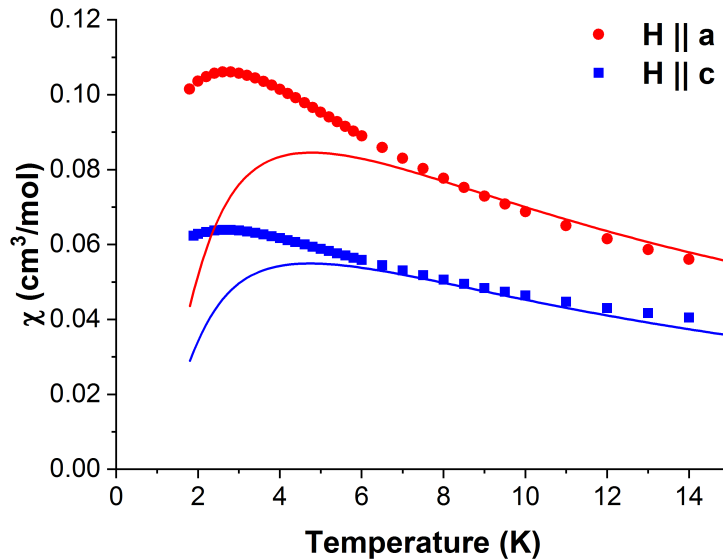


Fig. 47 | Calculated susceptibility for a Yb₆ hexamer. The measured low-temperature magnetic susceptibility is shown together with the calculation (solid lines) for a single plaquette with $S = 1/2$, and the Hamiltonian including Heisenberg exchange, dipolar interactions and easy-plane anisotropy. Error bars are standard deviations but are smaller than the data points. The Figure is adapted from Ref. [157].

In conclusion, YbBr₃ exhibits only a short-range Néel ordered ground-state well below the maximum of the static susceptibility. The observed continuum is evidence for a quantum spin liquid phase in YbBr₃. The origin of the observed continuum is linked to local plaquette fluctuations in the frustrated honeycomb lattice. The existence of a deconfined quantum critical point is plausible in this picture and supported by results from coupled cluster methods, density matrix renormalization group calculations and Monte-Carlo simulations [143, 144, 169]. YbBr₃ is a case of a QSL on the honeycomb lattice without the assistance of Kitaev-type interactions.

6.7 Outlook

An unsolved problem is that the value of the easy-plane anisotropy Δ_{crit} is far from the value $g_z/g_x \approx 0.67$ calculated from the CEF and magnetic susceptibility. Within linear spin-wave theory, $g_z/g_x \approx 0.67$ lifts the degeneracy of the acoustic and optical branch and manifests in an observable splitting of the two magnon branches (see Fig. 37a). However, there is no evidence found for the presence of the optical branch. Still, it is possible that the continuum is the residue of the missing optical branch. In any case, the distribution of the continuum in YbBr₃ is currently not well understood and requires more experimental as well as theoretical studies.

One approach for further investigations is the application of a magnetic field and observe the change of the spin-wave excitations. In LSWT, a field applied perpendicular to the hexagonal plane lifts the degeneracy of the spin-wave branches in the honeycomb antiferromagnet while it cants the spins out of the hexagonal plane. The corresponding Hamiltonian is [170]

$$\mathcal{H} = J \sum_{(ij)} (\vec{S}_i \cdot \vec{S}_j - (1 - \Delta) S_i^z S_j^z) - H \sum_i S_i^z$$

where (ij) runs over the nearest-neighbor bonds, J is the Heisenberg exchange, $0 \leq \Delta \leq 1$ is the easy-plane anisotropy and H the external magnetic field parameter. By enforcing the separation of the acoustic and optical branch, it is possible to clarify the relation between the continuum of magnetic excitations and optical branch (see Fig. 48). In addition, the study of the spin-wave excitations under magnetic field allows to more precisely determine the exchange parameters as well as the easy-plane anisotropy.

Beyond LSWT, it is predicted that the spin-waves on a honeycomb lattice decay under an applied magnetic field parallel to the c -axis and the optical branch is damped over a broad range in momentum [170]. It is possible that the optical branch is already damped in YbBr₃ under zero field due to the competition between the single-ion anisotropy and dipolar interactions. There is also the intriguing possibility that quantum fluctuations may be enhanced under magnetic field since easy-plane anisotropy and magnetic field compete with each other, similar to easy-plane anisotropy and dipolar interactions. Another possibility is to apply the magnetic field in the hexagonal plane which may enhance the quantum fluctuations. In the QSL-candidate system α -RuCl₃, the magnetically ordered state is suppressed by an in-plane magnetic field and the system transitions into a quantum spin liquid state [171, 172].

Furthermore, the temperature dependence of the spin-wave excitations in YbBr₃ is also an interesting topic to study. It appears that the continuum persists to higher

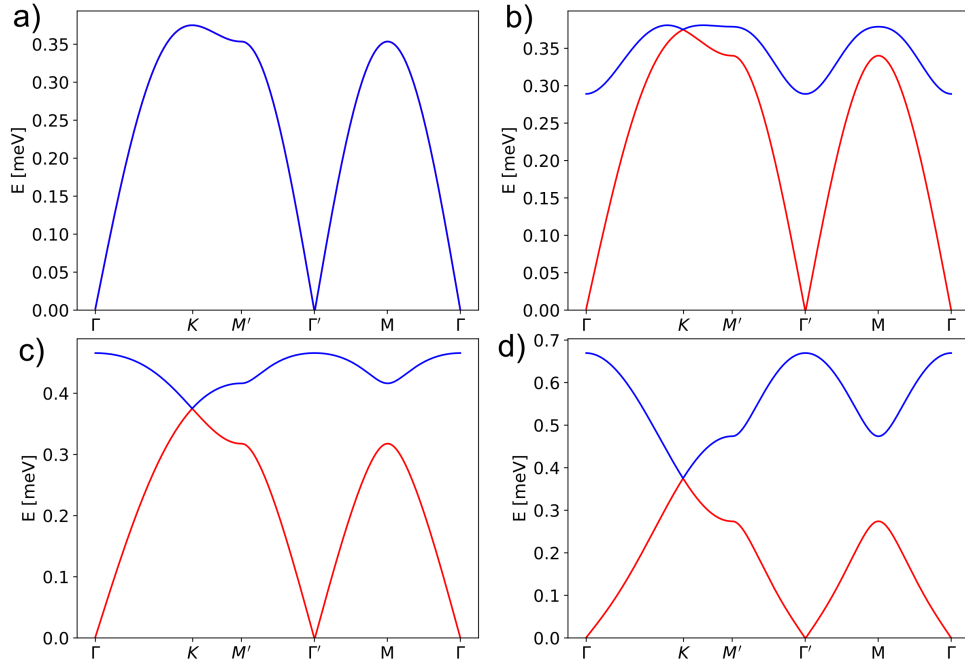


Fig. 48 | Spin-wave dispersion under magnetic field along the c -axis. The spin-wave dispersion of the nearest-neighbor Heisenberg model on the honeycomb lattice with easy-plane anisotropy under magnetic field is shown for different parameter sets. **a**, $J = 0.25$ meV, $\Delta = 1$ and $B = 0$ T. **b**, $J = 0.25$ meV, $\Delta = 1$ and $B = 10$ T. **c**, $J = 0.25$ meV, $\Delta = 0.6$ and $B = 10$ T. **d**, $J = 0.25$ meV, $\Delta = 0$ and $B = 10$ T.

The anisotropy Δ is isotropic for $\Delta = 1$ and at its maximum for $\Delta = 0$.

at least $T = 250$ mK as shown in Fig. 49. While the low-energy excitations lose intensity, the broad excitations remain largely unaffected. Additionally, there is significant paramagnetic scattering present at $T = 20$ K that extends up to ~ 1 meV (see Fig.41b) that is not studied in detail in this thesis.

Hence, the investigation of the magnetic field and temperature phase diagram of YbBr₃ can provide further insights into the nature of the spin-wave excitations of the two-dimensional frustrated honeycomb antiferromagnet with easy-plane anisotropy and dipolar interactions.

Exfoliation is also an intriguing method to use on the van der Waals system YbBr₃ with its natural layer structure. Two-dimensional monolayers can be investigated with different methods compared to three dimensional samples [173]. For example, the layer-dependent ferromagnetism of CrI₃ was investigated with the magneto-optical Kerr effect [174]. Another possibility is to use electrical means to probe the system. Electron tunneling was used to detect the magnetic ground-state of CrI₃ [175].

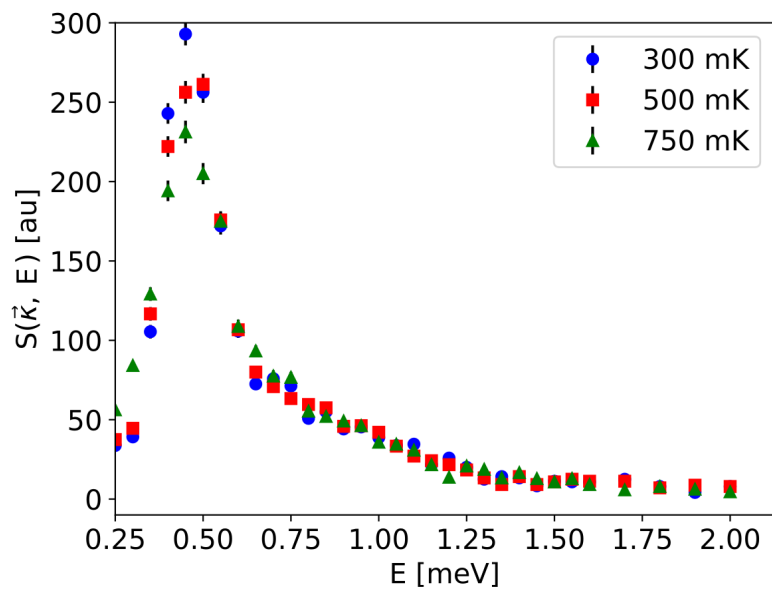


Fig. 49 | Temperature dependence of the spin-waves. Spin-waves and continuum at $(1.3, 0, 0)$ at $T = 300$ mK, 500 mK and 750 mK, respectively. Displayed are background subtracted measurements. All measurements were taken at $T = 250$ mK and the background was measured at $T = 20$ K.

6.8 YbBr₃: Experimental details

An YbBr₃ single crystal of cylindrical shape (15 mm diameter, 18 mm height) was grown from the melt in a sealed silica ampoule by the Bridgman method, as previously described for ErBr₃ [72]. YbBr₃ was prepared from Yb₂O₃ (6N, Metall Rare Earth Ltd.) by the NH₄Br method [176] and sublimed for purification. All handling of the hygroscopic material was done under dry and O-free conditions in glove boxes or closed containers.

The magnetic susceptibility was determined with a MPMS SQUID system (Quantum Design).

The neutron experiments were performed at the Swiss Spallation Neutron Source (SINQ) utilizing different instruments. On all instruments filters were used to reduce contamination of the beam by higher-order neutron wavelengths.

The crystal structure of YbBr₃ was refined using diffraction data collected with the high-resolution powder diffractometer HRPT at the wavelength of $\lambda = 1.494 \text{ \AA}$ at room temperature. The crystal structure and lattice parameters were refined with Fullprof [73].

The magnetic ground-state was investigated with the multi-counter diffractometer DMC at the wavelength $\lambda = 2.4576 \text{ \AA}$ which integrates fluctuations up to a maximum of $\sim 13.5 \text{ meV}$. The measured neutron intensity is proportional to the equal time spin-spin correlation function.

The crystal-field splitting of the Yb³⁺ ions was determined on the thermal three-axis spectrometer EIGER operated in the constant final-energy mode with $k_f = 2.662 \text{ \AA}^{-1}$ at $T = 1.5 \text{ K}$ and $|\vec{k}| = 1.5 \text{ \AA}^{-1}$. With that configuration the energy resolution is 0.8 meV at the elastic position.

The dispersion of the magnon excitations is bound by $E(\mathbf{q}) < 1 \text{ meV}$ in YbBr₃ which required the use of cold neutrons that provide an improved energy resolution. Therefore the measurements of the spin-waves were performed with the cold-neutron three-axis spectrometer TASP using $k_f = 1.3 \text{ \AA}^{-1}$ which resulted in an energy-resolution of $80 \mu\text{eV}$. To maximize the intensity, the measurements were performed without collimators in the beam and the analyzer was horizontally focusing.

7 Appendix

7.1 Instruments

This section describes the two types of neutron instrument used in this thesis, the triple-axis spectrometer (TAS) and diffractometer as well as the equipment used in neutron scattering experiments. Both instruments consist of several parts that are commonly mounted on hover-pads to allow movement and the selection of different angles between the parts.

Diffractometer

Fig. 50 presents the typical schematic layout of a neutron diffractometer.

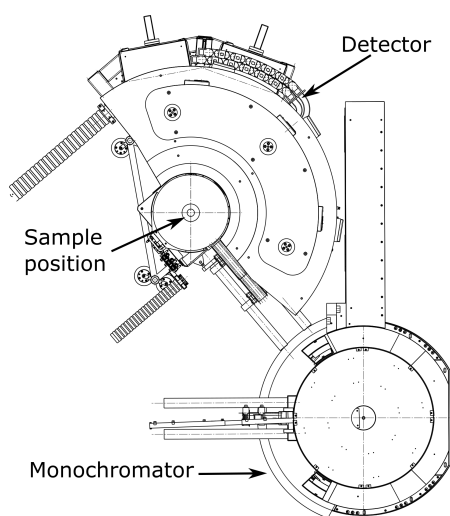


Fig. 50 | Schematic of a diffractometer. The Figure shows the layout of the DMC instrument at SINQ. The Figure was provided by P. Keller and adapted.

The neutron beam reaches the monochromator through neutron guides from the spallation or fission source after passing through a moderator [177]. At the monochromator, the energy of the neutron beam is selected by Bragg diffraction of neutrons with $E = 2.072k^2$. The sample scatters the single-energy neutrons under an exchange of energy and momentum with its nuclei and electron spins. Afterwards, the scattered neutrons are directly measured by an detector. The detector is commonly an array of detector tubes that is capable of detecting neutrons in a certain angular range [177]. Diffractometers measure the elastic neutron scattering and are often used to determine the nuclear and magnetic structure factor of powder samples. This is a central method for the investigation of the chemical and magnetic structures of crystals in crystallography.

Triple-axis spectrometer

Fig. 51 presents the typical schematic layout of a triple-axis spectrometer (TAS). Instead of directly measuring the scattered neutrons after the sample, TAS use an analyzer to select a specific energy that is detected by a single detector tube [177]. The analyzer works similar to the monochromator by Bragg diffraction on a single-crystal to select neutrons with $\hbar\vec{k}_f$.

Summarized, the TAS allows for an energy and momentum resolved investigation of excitations with inelastic neutron scattering in the physically accessible 4D-space with high resolution [177]. Neutrons are scattered three times in a TAS to select the correct energy and momentum by adapting the respective angles between the parts of the instrument. This is also the name-giving characteristic of TAS. Commonly, TAS are used to study magnetic and structural excitations in single crystals.

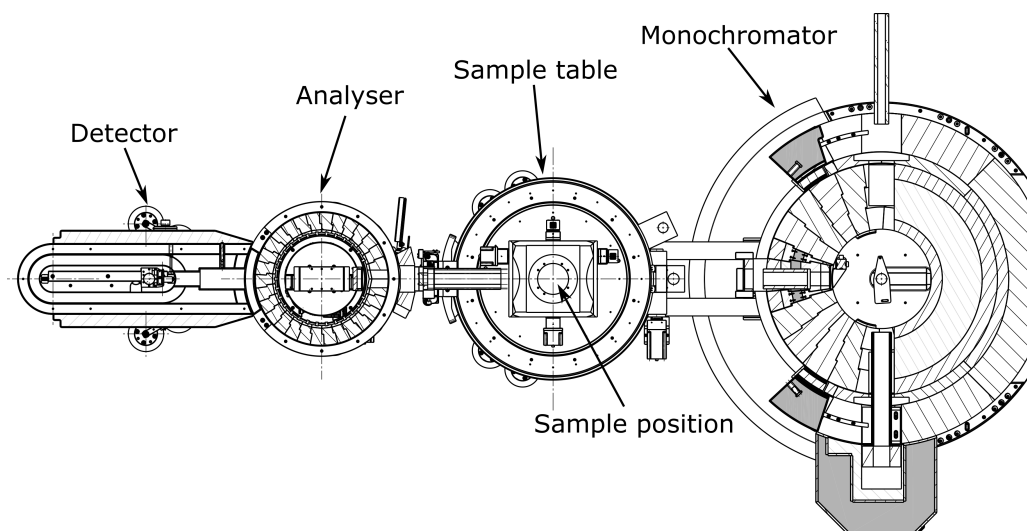


Fig. 51 | Schematic of a triple-axis spectrometer. The Figure shows the layout of the TASP instrument at SINQ. The Figure was provided by P. Keller and adapted.

Further equipment

Filter

Filters are used to remove neutrons with larger wavelengths λ_{har} , more specifically $n \times \lambda_0$. These so-called higher harmonics contaminate the monochromatic or single-energy neutron beam since they also fulfill Bragg's law. The principle behind the filters is that the scattering rate for neutrons changes with their wave-lengths so that unwanted neutrons are scattered away from the detector [177]. Be-filters allow neutrons to be transmitted only below a critical wavevector $k_f = 1.55 \text{ \AA}^{-1}$. For specific wave-lengths, graphite filters transmit the first harmonic but scatter the higher harmonics what provides not contaminated neutron beams at these wave-lengths.

Collimators

Collimators consist of two types of alternately stacked plates that strongly absorb neutrons and hardly affect neutrons, respectively [177]. Neutrons can only pass through if their momentum is parallel to the plates and therefore, the neutron beam is collimated. The neutron flux is reduced as a trade-off but the \vec{q} -resolution is significantly improved.

Sample environment - Cryostat

Many experiments require specific sample environments, in particular for magnetic systems. Low temperatures are among the most common requirements and are achieved by placing the sample into a cryostat. Cryostats can cool samples down to temperature in the milli-Kelvin range [178]. Liquid helium and liquid nitrogen are utilized as coolants. The evaporation of helium allows to achieve temperatures of about 1 K [178]. Lower temperatures require complex cooling processes that involve the admixture of different helium isotopes [178]. It is also possible to combine magnetic field, pressure and low temperature in a single experiment. Specialized cryostats and equipment allow to define a wide range of experimental parameters.

Resolution function

The resolution of neutron instruments is determined by the collimation of the beam and the finite mosaic spread of the monochromator and analyser crystals. And so, there is always a small probability of less likely neutrons to end up in the detector from a range $\delta\vec{\kappa}$ and δE around the chosen $\vec{\kappa}$ and E . This leads to a 4-dimensional resolution ellipsoid since the spread in $\Delta\kappa$ and ΔE are different. This can lead to non-physical line broadening and asymmetrical lineshapes that need to be corrected

by convoluting the neutron cross-section with the resolution function of the spectrometer. This problem has been addressed by many theoretical works and has been implemented in softwares like Takin that was used in this thesis. [158, 179, 180, 181].

7.2 Ewalds's summation

Ewald's summation or method is used to transform a slowly converging lattice sum into two rapidly converging lattice sums, one in real space and the other in reciprocal space [78]. The procedure can be summarized as follows. First, the sum of a function f is expressed as an integral with the help of the δ -function. Then, the integral is split into two parts by adding zero in the form of an appropriate function so that one part converges rapidly.

$$\sum_i f(x_i) = \int \rho(x) dx = \int \rho(x) \Phi(x) dx + \int \rho(x) [1 - \Phi(x)] dx$$

where $\rho(x) = \sum_i f(x_i) \delta(x - x_i)$ and Φ is a rapidly converging function. The first part now rapidly converges in real space through Φ . The latter term is then Fourier-transformed (FT) with Parseval's formula [182] and, if Φ was correctly chosen, will also rapidly converge in reciprocal space. The complement of the errorfunction $Errfc$ is often chosen as Φ since it rapidly converges as well as $FT\{1 - Errfc\}$.

7.3 Efficient formula for the calculation of the dipolar interactions

This section presents the results of the calculation of the Fourier-transform of the dipolar interactions (DI) in a rapidly converging lattice sum. Formulas were obtained for the Bravais lattice in 2D and 3D as well as non-Bravais lattices. The inter-lattice interactions are required to describe non-Bravais lattices with multiple ions in the unit cell like the honeycomb lattice. The calculations presented here follow the calculations of Bonsall and Maradudin [183].

Here, I use the discrete Fourier transformation (FT) of the double derivative of $1/|\vec{r} - \vec{r}_l|$ in the limit $\vec{r} \rightarrow 0$ that can be derived to be the same as the discrete FT of the dipolar interactions

$$\begin{aligned} & \lim_{r \rightarrow 0} \sum_{l \neq 0} \left[\frac{3(\vec{r} - \vec{r}_l)_\alpha (\vec{r} - \vec{r}_l)_\beta}{|\vec{r} - \vec{r}_l|^5} - \frac{\delta_{\alpha\beta}}{|\vec{r} - \vec{r}_l|^3} \right] e^{i\vec{q} \cdot \vec{r}_l} \\ &= \lim_{r \rightarrow 0} \sum_{l \neq 0} \frac{\delta^2}{\delta_\alpha \delta_\beta} \frac{e^{-i\vec{q} \cdot \vec{r}_l}}{|\vec{r} - \vec{r}_l|} \\ &= \lim_{r \rightarrow 0} \sum_l \frac{\delta^2}{\delta_\alpha \delta_\beta} \left(\underbrace{e^{-i\vec{q} \cdot \vec{r}} e^{-i\vec{q} \cdot (\vec{r} - \vec{r}_l)}}_{I} \frac{1}{|\vec{r} - \vec{r}_l|} - \underbrace{\frac{1}{|\vec{r}|}}_{II} \right) = I + II. \end{aligned}$$

where \vec{r} is a position vector, \vec{r}_l is the position of the l lattice site and \vec{q} is the wave-vector. I is then written in the integral representation and the integral is split into two parts

$$\begin{aligned} I &= \lim_{r \rightarrow 0} \sum_l \frac{\delta^2}{\delta_\alpha \delta_\beta} \frac{e^{-i\vec{q} \cdot (\vec{r}_l)}}{|\vec{r} - \vec{r}_l|} \\ &= \lim_{r \rightarrow 0} \frac{1}{\sqrt{\pi}} \sum_l \frac{\delta^2}{\delta_\alpha \delta_\beta} \int_0^\infty t^{-0.5} e^{-t|\vec{r} - \vec{r}_l|^2 - i\vec{q} \cdot \vec{r}_l} dt \\ &= \lim_{r \rightarrow 0} \frac{1}{\sqrt{\pi}} \sum_l \frac{\delta^2}{\delta_\alpha \delta_\beta} \left[\underbrace{\int_0^\Theta}_{i} + \underbrace{\int_\Theta^\infty}_{ii} \right] t^{-0.5} e^{-t|\vec{r} - \vec{r}_l|^2 - i\vec{q} \cdot \vec{r}_l} dt. \end{aligned} \tag{19}$$

where Θ is the Ewald parameter. A proper choice of the Ewald parameter ensures a rapid convergence of the lattice sums. Both integrals, i and ii , are then reexpressed by the Misra functions, $\varphi_n(t) = \int_0^\infty t^n e^{-tx} dx$, through variable substitution. The same procedure is performed for the second term II and one obtains a rapidly converging formula for the Fourier-transform of the dipolar interactions. It is important

to notice that the Fourier-transform has different results in two and three dimensions. The formulas for the Ewald summation of the FT of the DI for the different cases are presented below.

Bravais lattice in 3D

$$\begin{aligned}
D_{AA}^{\alpha\beta} &= \lim_{r \rightarrow 0} \sum_{l \neq 0} \left[\frac{3(\vec{r} - \vec{r}_l)_\alpha (\vec{r} - \vec{r}_l)_\beta}{|\vec{r} - \vec{r}_l|^5} - \frac{\delta_{\alpha\beta}}{|\vec{r} - \vec{r}_l|^3} \right] e^{i\vec{q} \cdot \vec{r}_l} \\
&= \frac{-\pi}{V\Theta} \sum_{\vec{G}} (\vec{q} + \vec{G})_\alpha (\vec{q} + \vec{G})_\beta \varphi_0\left(\frac{|\vec{q} + \vec{G}|^2}{4\Theta}\right) + \frac{4\Theta^{1.5}}{3\sqrt{\pi}} \delta_{\alpha\beta} \\
&\quad + \sqrt{\frac{\Theta}{\pi}} \sum_{l \neq 0} e^{-i\vec{q} \cdot \vec{r}_l} [4\Theta^2 (\vec{r}_l)_\alpha (\vec{r}_l)_\beta \varphi_{1.5}(\Theta|\vec{r}_l|^2) - 2\Theta \delta_{\alpha\beta} \varphi_{0.5}(\Theta|\vec{r}_l|^2)]
\end{aligned}$$

where \vec{G} is a reciprocal lattice vector and V is the volume of the unit cell. Θ is the Ewald parameter that has to be chosen such that the sum converges rapidly.

Interaction between two Bravais lattice in 3D

$$\begin{aligned}
D_{AB}^{\alpha\beta} &= \frac{-\pi}{V\Theta} \sum_{\vec{G}} e^{i\vec{G} \cdot \vec{\tau}_{AB}} (\vec{q} + \vec{G})_\alpha (\vec{q} + \vec{G})_\beta \varphi_0\left(\frac{|\vec{q} + \vec{G}|^2}{4\Theta}\right) \\
&\quad + \frac{1}{\sqrt{\pi}} \sum_{\vec{r}_B} e^{-i\vec{q} \cdot (\vec{\tau}_{AB} + \vec{r}_B)} [4(\vec{\tau}_{AB} + \vec{r}_B)_\alpha (\vec{\tau}_{AB} + \vec{r}_B)_\beta \Theta^{2.5} \varphi_{1.5}(\Theta|\vec{\tau}_{AB} + \vec{r}_B|^2) \\
&\quad - 2\delta_{\alpha\beta} \Theta^{1.5} \varphi_{0.5}(\Theta|\vec{\tau}_{AB} + \vec{r}_B|^2)]
\end{aligned}$$

where $\vec{\tau}_{AB}$ is the vector connecting the two sublattices A and B . *Bravais lattice in 2D*

$$\begin{aligned}
D_{AA}^{\alpha\beta} &= \lim_{r \rightarrow 0} \sum_{l \neq 0} \left[\frac{3(\vec{r} - \vec{r}_l)_\alpha (\vec{r} - \vec{r}_l)_\beta}{|\vec{r} - \vec{r}_l|^5} - \frac{\delta_{\alpha\beta}}{|\vec{r} - \vec{r}_l|^3} \right] e^{i\vec{q} \cdot \vec{r}_l} \\
&= -\frac{\sqrt{\pi}}{S\sqrt{\Theta}} \sum_{\vec{G}} (\vec{q} + \vec{G})_\alpha (\vec{q} + \vec{G})_\beta \varphi_{-0.5}\left(\frac{|\vec{q} + \vec{G}|^2}{4\Theta}\right) + \frac{4\Theta^{1.5}}{3\sqrt{\pi}} \delta_{\alpha\beta} \\
&\quad + \sqrt{\frac{\Theta}{\pi}} \sum_{l \neq 0} e^{-i\vec{q} \cdot \vec{r}_l} [4\Theta^2 |\vec{r}_l|_\alpha |\vec{r}_l|_\beta \varphi_{1.5}(\Theta|\vec{r}_l|^2) 2\Theta \delta_{\alpha\beta} \varphi_{0.5}(\Theta|\vec{r}_l|^2)]
\end{aligned}$$

where S is the area of the unit cell.

Ewald summation for the Fourier transform of the dipolar interactions between non-Bravais lattices in 2D

$$\begin{aligned}
D_{AB}^{\alpha\beta} &= \lim_{r \rightarrow 0} \sum_{\vec{r}_{AB}} \frac{\delta^2}{\delta_\alpha \delta_\beta} \frac{e^{-i\vec{q} \cdot \vec{r}_{AB}}}{|\vec{r} - \vec{r}_{AB}|} \\
&= -\frac{\sqrt{\pi}}{S\sqrt{\Theta}} \sum_{\vec{G}} e^{i\vec{G} \cdot \vec{r}_{AB}} (\vec{q} + \vec{G})_\alpha (\vec{q} + \vec{G})_\beta \varphi_{-0.5}\left(\frac{|\vec{q} + \vec{G}|^2}{4\Theta}\right) \\
&\quad + \frac{1}{\sqrt{\pi}} \sum_{\vec{r}_B} e^{-i\vec{q} \cdot (\vec{r}_{AB} + \vec{r}_B)} [4(\vec{r}_{AB} + \vec{r}_B)_\alpha (\vec{r}_{AB} + \vec{r}_B)_\beta \Theta^{2.5} \varphi_{1.5}(\Theta|\vec{r}_{AB} + \vec{r}_B|^2) \\
&\quad - 2\delta_{\alpha\beta} \Theta^{1.5} \varphi_{0.5}(\Theta|\vec{r}_{AB} + \vec{r}_B|^2)]
\end{aligned}$$

7.4 Linear spin-wave theory

Linear spin-wave theory (LSWT) allows to calculate the spin-wave dispersions with equivalent results to the MF-RPA method. To verify the results of MF-RPA, the dispersion of the spin-waves was calculated in LSWT.

The Hamiltonian in Eq. 6 is simplified by excluding the DI and setting $g = 1$ to calculate the spin-wave dispersion for the antiferromagnet on the honeycomb lattice with spins in the hexagonal plane. The spin-operators are rotated into a local coordinate system with the rotation matrix in Eq. 10 where $\theta = 0$, $\phi = \pi$ for all i on the A sublattice and $\theta = \pi/2$, $\phi = \pi$ for all i on the B sublattice. This ensures that the quantification axis is aligned with the spin direction in the local coordinate system. It follows that the Hamiltonian is

$$\begin{aligned}
\mathcal{H} = & -\frac{1}{2} \sum_{ij \in A} J_{ij}^{AA} [s_i^z s_j^z + s_i^y s_j^y + s_i^x s_j^x] \\
& -\frac{1}{2} \sum_{i \in A, j \in B} J_{ij}^{AB} [-s_i^z s_j^z - s_i^y s_j^y + s_i^x s_j^x] \\
& -\frac{1}{2} \sum_{i \in B, j \in A} J_{ij}^{BA} [-s_i^z s_j^z - s_i^y s_j^y + s_i^x s_j^x] \\
& -\frac{1}{2} \sum_{ij \in B} J_{ij}^{BB} [s_i^z s_j^z + s_i^y s_j^y + s_i^x s_j^x]
\end{aligned} \tag{20}$$

where \vec{s} the spin-operators in the local frame and J the exchange interactions. A, B label the sublattice.

Then the Holstein-Primakoff transformation [184] is applied

$$\begin{aligned}
s_A^x(i) &= \frac{\sqrt{2S}}{2} (a_i + a_i^\dagger), & s_A^y(i) &= \frac{\sqrt{2S}}{2i} (a_i - a_i^\dagger), & s_A^z(i) &= S - a_i^\dagger a_i = S - \langle n \rangle \\
s_B^x(j) &= \frac{\sqrt{2S}}{2} (b_j + b_j^\dagger), & s_B^y(j) &= \frac{\sqrt{2S}}{2i} (b_j - b_j^\dagger), & s_B^z(j) &= S - b_j^\dagger b_j = S - \langle n \rangle
\end{aligned} \tag{21}$$

The resulting Hamiltonian is Fourier transformed with

$$\begin{aligned}
J(\vec{\kappa}) &= \frac{1}{N} \sum_{ij} J_{ij} \exp(-i\vec{\kappa} \cdot (\vec{R}_i - \vec{R}_j)) \\
a(\vec{\kappa}) &= \frac{1}{\sqrt{N}} \sum_{ij} a_i \exp(-i\vec{\kappa} \cdot \vec{R}_i), \quad a^\dagger(\vec{\kappa}) = \frac{1}{\sqrt{N}} \sum_{ij} a_i^\dagger \exp(i\vec{\kappa} \cdot \vec{R}_i) \\
b(\vec{\kappa}) &= \frac{1}{\sqrt{N}} \sum_{ij} b_i \exp(-i\vec{\kappa} \cdot \vec{R}_i), \quad b^\dagger(\vec{\kappa}) = \frac{1}{\sqrt{N}} \sum_{ij} b_i^\dagger \exp(i\vec{\kappa} \cdot \vec{R}_i)
\end{aligned} \tag{22}$$

resulting in

$$\begin{aligned}
\mathcal{H} &= \frac{S}{4} \sum_k \{ 4J_0^{NN} (a_k^\dagger a_k + b_k^\dagger b_k) - 2J_k^{NN} (a_{-k} a_{-k}^\dagger + a_k^\dagger a_k + b_{-k} b_{-k}^\dagger + b_k^\dagger b_k) \\
&\quad - 4J_0^N (a_k^\dagger a_k + b_k^\dagger b_k) + 2J_k^N (a_{-k} b_k + a_k^\dagger b_{-k}^\dagger + b_{-k} a_k + b_k^\dagger a_{-k}^\dagger) \}
\end{aligned} \tag{23}$$

where $J_{\vec{\kappa}}^\delta = j^\delta \sum_{\vec{\delta}} e^{i\vec{\kappa} \cdot \vec{\delta}}$ for nearest ($\delta = N$) and next-nearest ($\delta = NN$) neighbors with interaction strength j . The Hamiltonian can be diagonalized by the general transformation [77]

$$\alpha_{\vec{\kappa}}(i) = u_{\vec{\kappa}}(i) a_{\vec{\kappa}} - l_{\vec{\kappa}}(i) a_{-\vec{\kappa}}^\dagger + v_{\vec{\kappa}}(i) b_{\vec{\kappa}} - m_{\vec{\kappa}}(i) b_{\vec{\kappa}}^\dagger \tag{24}$$

where $i = 1, 2$ is the label for the two sublattices and α is a Boson operator. To obtain the spin-wave dispersion, the Heisenberg equation of motion needs to be solved

$$i\hbar \frac{d\alpha_{\vec{\kappa}}(i)}{dt} = -[\mathcal{H}, \alpha_{\vec{\kappa}}(i)] = E(\vec{\kappa}). \tag{25}$$

Eq. 25 results in a linear system of equations that must be solved for $E(\vec{\kappa})$. The spin-wave dispersion is given by

$$E_{1,2}(\vec{\kappa}) = +\sqrt{A_{\vec{\kappa}}^2 - |C_{\vec{\kappa}}|^2}$$

where $A_{\vec{\kappa}} = \frac{S}{2} (J_{\vec{\kappa}}^{NN} + J_{-\vec{\kappa}}^{NN} - 2J_0^{NN} + J_0^N + J_0^N)$, $C_{\vec{\kappa}} = \frac{S}{2} (J_{\vec{\kappa}}^N + J_{-\vec{\kappa}}^N)$.

The spin-wave dispersion for the antiferromagnet on the honeycomb lattice with easy-plane anisotropy including nearest-and next-nearest neighbor interactions is calculated in a similar way with the Hamiltonian

$$\mathcal{H} = -\frac{1}{2} \sum_{ij} \mathcal{J}_{\alpha\beta}(i, j) S_i^\alpha S_j^\beta - (1 - \Delta) S_i^z S_j^z$$

where i, j are positions of the i and j ion, respectively, J_{ij} are the nearest and next-nearest neighbor Heisenberg exchange interactions and Δ is the easy-plane anisotropy. The spin-wave dispersion is calculated to follow

$$E_{1,2}(\vec{k}) = +\sqrt{A_{\vec{k}}^2 - |C_{\vec{k}}|^2 - D_{\vec{k}}^2 + |E_{\vec{k}}|^2} \pm \sqrt{4(C_{\vec{k}}D_{\vec{k}} - A_{\vec{k}}E_{\vec{k}})(C_{\vec{k}}^*D_{\vec{k}} - A_{\vec{k}}E_{\vec{k}}^*)}$$

where $*$ is the complex-conjugate, $A_{\vec{k}} = \frac{S}{4}((J_{\vec{k}}^{NN} + J_{-\vec{k}}^{NN})(\Delta + 1) - 2J_0^{NN} + 2J_0^N)$, $C_{\vec{k}} = \frac{S}{4}(J_{\vec{k}}^N + J_{-\vec{k}}^N)(\Delta + 1)$, $D_{\vec{k}} = \frac{S}{4}(J_{\vec{k}}^{NN} + J_{-\vec{k}}^{NN})(\Delta - 1)$, $E_{\vec{k}} = \frac{S}{4}(J_{\vec{k}}^N + J_{-\vec{k}}^N)(\Delta - 1)$ and Δ the easy-plane anisotropy with $0 \leq \Delta \leq 1$. $\Delta = 1$ represents the isotropic case. For any value of Δ , the acoustic branch has no spin gap.

The major difference between the two spin-wave dispersions is that the easy-plane anisotropy lifts the degeneracy between the two spin-wave branches. Without anisotropy, the two spin-wave branches are always degenerate. On the other hand, the spin-waves are always degenerate at the K points for any value of easy-plane anisotropy.

7.5 Berry phase, Berry curvature and Chern number: relation and calculation

Topological systems are a topic of interest in condensed matter physics since they feature states that are stable against perturbations. A non-zero value for the Chern number shows that the system is topologically non-trivial. The starting point to determine the Chern number is the Berry phase γ that is a phase picked up by the wave function during the adiabatic movement along a closed path \mathcal{C} in momentum space.

$$\gamma_n = i \oint_{\mathcal{C}} \vec{A}_n(\vec{k}) d\vec{k} = -\Im \int_S \vec{\Omega}_n(\vec{k}) dS$$

where $\vec{A}_n(\vec{k}) \equiv \langle \Psi_n(\vec{k}) | \partial_{\vec{k}} \Psi_n(\vec{k}) \rangle$ is the Berry connection and $\vec{\Omega}_n(\vec{k}) = \vec{\partial} \times \vec{A}_n(\vec{k})$ is the Berry curvature for the n th mode of the excitations [29, 30]. The integral of the Berry curvature over the whole Brillouin zone gives the Chern number C_n for the n th mode and whether the system is topologically trivial or not

$$C_n = -\frac{1}{2\pi} \sum_n \int_{BZ} \vec{\Omega}_n(\vec{k}) dS.$$

There is an algorithm to efficiently calculate the Berry curvature $\Omega(\vec{\kappa})$ over the Brillouin zone with the constraint that it is only applicable to non-degenerate branches of the spin-wave dispersion. The method to efficiently calculate the Berry curvature is presented in the References [121, 185]. One defines a grid in momentum space covering the Brillouin zone with the unit vectors \hat{e}_1, \hat{e}_2 . Each point α of the grid is identified by $\vec{\kappa}_\alpha$. The Berry curvature is calculated as

$$\Omega(\vec{\kappa}_\alpha) = \ln \left(\frac{\mathcal{U}_1(\vec{\kappa}_\alpha) \mathcal{U}_2(\vec{\kappa}_\alpha + \hat{e}_1)}{\mathcal{U}_1(\vec{\kappa}_\alpha + \hat{e}_2) \mathcal{U}_2(\vec{\kappa}_\alpha)} \right) \quad (26)$$

with the link variable $\mathcal{U}_x = \frac{\langle u(\vec{\kappa}_\alpha) | u(\vec{\kappa}_\alpha + \hat{e}_x) \rangle}{|\langle u(\vec{\kappa}_\alpha) | u(\vec{\kappa}_\alpha + \hat{e}_x) \rangle|}$ where $x = 1, 2$ and $u(\vec{\kappa}_\alpha)$ is the eigenvector of the Hamiltonian with the vector $\vec{\kappa}_\alpha$ [185].

This implies that one needs to calculate the eigenstates of the Hamiltonian in the MF-RPA to obtain the Berry curvature. The eigenvectors were determined by solving the matrix equation [186]

$$\{\bar{\mathbb{1}} - \bar{\chi}_0(E) \bar{\mathcal{J}}(\vec{\kappa}_\alpha)\} |u(\vec{\kappa}_\alpha)\rangle = 0$$

with a *svd* algorithm. $\bar{\chi}_0$ is the single-ion susceptibility and $\bar{\mathcal{J}}$ the interaction tensor. The energy E of the magnon dispersion at a certain momentum is obtained by calculating the equation [186]

$$\det[\bar{1} - \bar{\chi}_0(E)\bar{\mathcal{J}}(\vec{k})] = 0.$$

8 Acknowledgments

My research would not have been possible without the collaborative effort of many people. Without the discussions and support of many more people, I would not have been able to finish this thesis. Therefore, I want to acknowledge their contributions as well as express my gratitude and thanks to all of them:

To my *Doktorvater* Prof. Dr. Michel Kenzelmann and my supervisor Dr. Bertrand Roessli who gave me the opportunity to do my thesis with them. They always gave their all in teaching and supporting me in my work and experiments. Without their guidance, I would have struggled to reach the point I am at right now.

To my collaborators on the rare-earth trihalide experiments: Dr. Karl Krämer, Dr. Bertrand Roessli, Dr. Benjamin Braun, Dr. Uwe Stuhr, Dr. Denis Cheptiakov, Dr. Lukas Keller, Dr. Bernard Delley, Dr. Andrew Wildes, Prof. Dr. Oliver Waldmann and Prof. Dr. Michel Kenzelmann Without their help, support and teachings, I could not have achieved the results I have.

To the technicians, secretaries and other people at the Paul Scherrer Institut that make experiments and works like mine possible and a great experience.

To my fellow Phd students, current and former, who I had the fortune to get to know and become friends with. In particular, Alexandra who taught me to pronounce *parameter* and did a great job improving my English.

To my friends who were there for me and patiently listened to me explaining my work giving me an outside perspective.

To my family who are firm pillars for me to lean on: My grandparents who always believe in me. My parents who are always there for me. My brother who always makes me laugh.

Thank you!

9 Bibliography

References

- [1] E. Du Trémolet de Lacheisserie, D. Gignoux & M. Schlenker; *Magnetism: Fundamentals*. Springer (2005).
- [2] W. Gilbert; *Tractatus, sive physiologia nova de magnete, magneticisque corporibus et de magno magnete tellure. Sex libris comprehensus*. English translation: S.P. Thompson, Chiswick Press, London, (1900).
- [3] H.C. Oersted; Experiments on the effect of a current of electricity on the magnetic needles. *Annals of Philosophy* **16**, 273 (1820).
- [4] A.K.T. Assis & J.P.M.C. Chaib; *Ampere's electrodynamics*. Aperion (2015).
- [5] M. Faraday; *Experimental researches in chemistry and physics*. Richard Taylor and William Francis, London (1859).
- [6] J.C. Maxwell; A dynamical theory of the electromagnetic field. *Philosophical Transactions of the Royal Society of London* **155**, 459–512 (1865).
- [7] P. Weiss; L'Hypothese du champ moleculaire et de la propriete ferromagnetique. *J. de Phys.* **6**, 661-690 (1907).
- [8] P. Curie; *Œuvres de Pierre Curie*. Publiées par les soins de la Société française de physique. Paris: Gauthier–Villars (1908).
- [9] L. Néel; Magnetic properties of ferrites: ferrimagnetism and antiferromagnetism. *Ann. Phys.* **3**, 137-198 (1948).
- [10] S. Blundell; *Magnetism in condensed matter*. Oxford Press (2001).
- [11] E. Ising; Beitrag zur Theorie des Ferromagnetismus. *Zeitschrift für Physik* **31**, 253–258 (1925).
- [12] W. Heisenberg; Zur Theorie des Ferromagnetismus. *Zeitschrift für Physik* **49**, 619-636 (1928)
- [13] W. Meissner & R. Ochsenfeld; Ein neuer Effekt bei Eintritt der Supraleitfähigkeit. *Naturwissenschaften* **21**, 787-788 (1933).
- [14] E.H. Hall; On a new action of the magnet in electric currents. *American Journal of Mathematics* **2**, 3, 287-292 (1879).
- [15] K. Klitzing; The quantized Hall effect. *Rev. Mod. Phys* **58**, 519 (1986).
- [16] G.L. Squire; *Introduction to the theory of thermal neutron scattering*, Dover Publications, INC (1996).
- [17] F. Bloch; Über die Quantenmechanik der Elektronen in Kristallgittern. *Zeitschrift für Physik* **52**, 555–600 (1929).

-
- [18] T. Chatterji; *Neutron scattering from magnetic materials*. Elsevier Science (2006).
- [19] K.S. Novoselov *et al.*; Electric field effect in atomically thin carbon films. *Science* **306**, 666-669 (2004).
- [20] K. S. Novoselov *et al.*; Two-dimensional atomic crystals. *Proc. Natl. Acad. Sci.* **102**, 10451–10453 (2005).
- [21] A.K. Geim & K.S. Novoselov; The rise of graphene. *Nature Materials* **6**, 183–191 (2007).
- [22] J. Cayssol; Introduction to Dirac materials and topological insulators. *C. R.Physique* **14**, 760–778 (2013).
- [23] The Nobel Prize in Physics 1933. NobelPrize.org. Nobel Prize Outreach AB 2022. Tue. 11 Jan 2022. <https://www.nobelprize.org/prizes/physics/1933/summary/>
- [24] Paul A.M. Dirac – Facts. NobelPrize.org. Nobel Prize Outreach AB 2022. Tue. 11 Jan 2022. <https://www.nobelprize.org/prizes/physics/1933/dirac/facts/>
- [25] A. Einstein; Zur Elektrodynamik bewegter Körper. *Ann. d. Phys.* **10**, 891-921 (1905).
- [26] Press release. NobelPrize.org. Nobel Prize Outreach AB 2022. Sun. 2 Jan 2022. <https://www.nobelprize.org/prizes/physics/1985/press-release/>
- [27] E.H. Hall; On a new action of the magnet on electric currents. *American Journal of Mathematics* **2**, 3, 287-292 (1879).
- [28] Klaus von Klitzing – Nobel Lecture. NobelPrize.org. Nobel Prize Outreach AB 2022. Sun. 2 Jan 2022. <https://www.nobelprize.org/prizes/physics/1985/klitzing/lecture/>
- [29] A.T. Costa *et al.*; Topological magnons in CrI₃ monolayers: an itinerant fermion description. *2D Mater.* **7**, 045031 (2020).
- [30] M.V. Berry; Quantal phase factors accompanying adiabatic changes. *Proceedings of the Royal Society A*, **392**, 45-57 (1984).
- [31] S. Michalakis; Why is the Hall conductance quantized? *Nature Reviews Physics* **2**, 392–393 (2020).
- [32] B. Simon; Holonomy, the quantum adiabatic theorem, and Berry’s phase. *Phys. Rev. Lett.* **51**, 2167 (1983).
- [33] The Nobel Prize in Physics 2016. NobelPrize.org. Nobel Prize Outreach AB 2022. Sun. 16 Jan 2022. <https://www.nobelprize.org/prizes/physics/2016/press-release/>
- [34] J.E. Avron, D. Osadchy & Ruedi Seiler; A topological look at the quantum Hall effect. *Physics Today* **568**, 8, 38 (2003).
-

-
- [35] K.N. Novoselov *et al.*; Two-dimensional gas of massless Dirac fermions in graphene. *Nature* **438**, 197-200 (2005).
- [36] K.I. Bolotin *et al.*; Observation of the fractional quantum Hall effect in graphene. *Nature* **462**, 196–199 (2009).
- [37] The Nobel Prize in Physics 1998. NobelPrize.org. Nobel Prize Outreach AB 2022. Mon. 3 Jan 2022. (<https://www.nobelprize.org/prizes/physics/1998/summary/>)
- [38] R. Sashikanth; Super-fluids and quantum-fluids – A brief review. *The Journal of Physics* **113**, 2018, 253-259 (2018).
- [39] K. Hatsuda *et al.*; Evidence for a quantum spin Hall phase in graphene decorated with Bi₂Te₃ nanoparticles. *Sci. Adv.* **4**, 1-6 (2018).
- [40] K. v. Klitzing *et al.*; 40 years of the quantum Hall effect. *Nature Reviews Physics* **2**, 397-401 (2020).
- [41] C.L. Kane & E.J. Mele; Quantum spin Hall effect in graphene. *Phys. Rev. Lett.* **95**, 226801 (2005).
- [42] M.Z. Hasan & C.L. Kane; Colloquium: Topological insulators. *Rev.Mod. Phys.* **82**, 3045-3065 (2010).
- [43] A. Hirohata *et al.*; Review on spintronics: Principles and device applications. *JMMM* **509**, 166711 (2020).
- [44] J.G. Park; Opportunities and challenges of 2D magnetic van der Waals materials: magnetic graphene? *J. Phys.: Condens. Matter* **28**, 301001 (2016).
- [45] A.S. Pershoguba *et al.*; Dirac magnons in honeycomb ferromagnets. *Phys. Rev. X* **8**, 011010 (2018).
- [46] R.S. Fishman, J. A. Fernandez-Baca & T. Rõõm. *Spin-wave theory and its applications to neutron scattering and THz spectroscopy*. Morgan & Claypool Publishers (2018).
- [47] B. Yuan *et al.*; Dirac magnons in a honeycomb lattice quantum XY Magnet CoTiO₃. *Phys. Rev. X* **10**, 011062 (2020).
- [48] L. Chen *et al.*; Massless Dirac magnons in the two dimensional van der Waals honeycomb magnet CrCl₃. *2D Mater.* **9**, 015006 (2022).
- [49] K. Nakata, J. Klinovaja & D. Loss; Magnonic quantum Hall effect and Wiedemann-Franz law. *Phys. Rev. B* **95**, 125429 (2017).
- [50] K.H. Lee *et al.*; Magnonic quantum spin Hall state in the zigzag and stripe phases of the antiferromagnetic honeycomb lattice. *Phys. Rev. B* **97**, 180401 (R) (2018).
- [51] V.V. Kruglyak *et al.*; Magnonics. *J. Phys. D: Appl. Phys.* **43**, 264001 (2010).
- [52] V. Kalmeyer & R.B. Laughlin; Equivalence of the resonating-valence-bond and fractional quantum Hall states. *Phys. Rev. Lett.* **59**, 2095 (1987).
-

- [53] P.W. Anderson; Resonating valence bonds: a new kind of insulator? *Mat. Res. Bull.* **8**, 153-160 (1973).
- [54] L. Balents; Spin liquids in frustrated magnets. *Nature* **464.**, 199-208 (2010).
- [55] P.W. Anderson; The resonating valence bond state in La_2CuO_4 and superconductivity. *Science* **235**, 1196 (1987).
- [56] C. Nayak *et al.*; Non-Abelian anyons and topological quantum computation. *Rev. Mod. Phys.* **80**, 1083 (2008).
- [57] L. Savary & L. Balents; Quantum spin liquids: a review. *Rep. Prog. Phys.* **80**, 016502 (2017).
- [58] C. Broholm *et al.*; Quantum spin liquids. *Science* **367**, 263 (2020).
- [59] G. Misguich; Quantum Spin Liquids and Fractionalization. In: C. Lacroix, P. Mendels & F. Mila (eds) ; *Introduction to Frustrated Magnetism*. Springer Series in Solid-State Sciences, vol 164. Springer, Berlin, Heidelberg.
- [60] B. Lake *et al.*; Quantum criticality and universal scaling of a quantum antiferromagnet. *Nature Materials* **4**, 329–334 (2005).
- [61] F. Duncan M. Haldane; *Nobel Lecture*. NobelPrize.org. Nobel Prize Outreach AB 2022. (<https://www.nobelprize.org/prizes/physics/2016/haldane/lecture/>)
- [62] H. Li & F.D.M. Haldane; Entanglement spectrum as a generalization of entanglement entropy: Identification of topological order in non-abelian fractional quantum Hall effect states. *Phys. Rev. Lett.* **101**, 010504 (2008).
- [63] X. Chen *et al.*; Symmetry protected topological orders and the group cohomology of their symmetry group. *Phys. Rev. B* **87**, 155114 (2013).
- [64] N.D. Mermin & H. Wagner; Absence of ferromagnetism or antiferromagnetism in one- or two-dimensional isotropic Heisenberg models. *Phys. Rev. Lett.* **17**, 1133 (1966).
- [65] V.L. Berezinsky; Destruction of long-range order in one-dimensional and two-dimensional systems possessing a continuous symmetry group. *Sov. Phys. JETP* **3**, 610-616 (1972).
- [66] J.M. Kosterlitz & D.J. Thouless; Long-range order and metastability in two-dimensional solids and superfluids. *J. Phys C: Solid State Phys.* **5**, L124-L126 (1972.)
- [67] J.M. Kosterlitz; Kosterlitz–Thouless physics: a review of key issues. *Rep. Prog. Phys* **79**, 026001 (2016).
- [68] M.H.W. Chan, A.W. Yanof & J.D. Reppy; Superfluidity of thin ^4He films. *Phys. Rev. Lett.* **32**, 1347 (1974).
- [69] A. Kitaev; Anyons in an exactly solved model and beyond. *Ann. Phys.* **321**, 2-111 (2006).

-
- [70] S.H. Chun *et al.*; Direct evidence for dominant bond-directional interactions in a honeycomb lattice iridate Na_2IrO_3 . *Nature Physics* **11**, 462-466 (2015).
- [71] A. Banerjee *et al.*; Proximate Kitaev quantum spin liquid behaviour in a honeycomb magnet. *Nature Materials* **15**, 733-740 (2016).
- [72] K.W. Krämer *et al.*; Noncollinear two- and three-dimensional magnetic ordering in the honeycomb lattices of ErX ($X = \text{Cl, Br, I}$). *Phys. Rev. B* **60**, R3724 (1999).
- [73] J. Rodríguez-Carvajal; Recent advances in magnetic structure determination by neutron powder diffraction. *Physica. B: Condensed Matter* **192**, 55-69 (1993).
- [74] D.J. Newman & B. Ng; *Crystal Field Handbook*. Cambridge, UK: Cambridge University Press, (2007).
- [75] K.W.H Stevens; Matrix elements and operator equivalents connected with the magnetic properties of rare earth ions. *Proc. Phys. Soc. A* **65**, 209 (1952).
- [76] E. Bauer & M. Rotter; *Magnetism of Complex Metallic Alloys: Crystalline Electric Field effects*, in: Book Series on Complex Metallic Alloys Vol. 2, ed. E. Belin-Ferr, World Scientific (2009).
- [77] E. Rastelli, *Statistical mechanics of magnetic excitations*. World Scientific (2013).
- [78] P.P. Ewald; Die Berechnung optischer und elektrostatischer Gitterpotentiale. *Ann. Phys.*, **3**, 253-287 (1921).
- [79] J.N. Reimers; Diffuse-magnetic-scattering calculations for frustrated antiferromagnets. *Phys. Rev. B* **46**, 193-202 (1992).
- [80] H. Kadowaki, Y. Ishii, K. Matsuhira & Y. Hinatsu; Neutron scattering study of dipolar spin ice $\text{Ho}_2\text{Sn}_2\text{O}_7$: Frustrated pyrochlore magnet. *Phys. Rev. B* **65**, 144421 (2002).
- [81] M. Enjalran & M.J.P. Gingras; Theory of paramagnetic scattering in highly frustrated magnets with long-range dipole-dipole interactions: The case of the $\text{Tb}_2\text{Ti}_2\text{O}_7$ pyrochlore antiferromagnet. *Phys. Rev. B* **70**, 174426 (2004).
- [82] V.M. Rozenbaum; Ground state and vibrations of dipoles on a honeycomb lattice. *Phys. Rev. B* **51**, 1290 (1995).
- [83] D.C. Johnston; Magnetic dipole interactions in crystals. *Phys. Rev. B* **93**, 014421 (2016).
- [84] C. Pich & F. Schwabl; Order of two-dimensional isotropic dipolar antiferromagnets. *Phys. Rev. B* **47**, 7957-7960 (1993).
- [85] C. Pich & F. Schwabl; Spin-wave dynamics of two-dimensional isotropic dipolar honeycomb antiferromagnets. *JMMM* **148**, 30-31 (1995).
-

-
- [86] J. Jensen & A.R. Macintosh; *Rare Earth Magnetism*. Clarendon Press, Oxford (1991).
- [87] J.M. Luttinger & L. Tisza; Theory of dipole interaction in crystals. *Phys. Rev.* **70**, 954 (1946).
- [88] Y.M. Malozovsk & V.M. Rozenbaum; Orientational ordering in two-dimensional systems with long-range interaction. *Physica A* **175**, 127 (1991).
- [89] G.O. Zimmerman, A.K. Ibrahim & F.Y. Wu; Planar classical dipolar system on a honeycomb lattice. *Phys. Rev. B* **37**, 2059 (1988).
- [90] M. Maksymenko, V.R. Chandra & R. Moessner; Classical dipoles on the kagome lattice. *Phys. Rev. B* **91**, 184407 (2015).
- [91] D. J. Bishop & J. D. Reppy; Study of the superfluid transition in two-dimensional ^4He films. *Phys. Rev. Lett.* **40**, 1727 (1978).
- [92] S. A. Wolf *et al.*; Two-dimensional phase transition in granular NbN films. *Phys. Rev. Lett.* **47**, 1071 (1981).
- [93] O. Johansen *et al.*; Current control of magnetism in two-dimensional Fe_3GeTe_2 . *Phys. Rev. Lett.* **122**, 217203 (2019).
- [94] C. Kane & J. Moore; Topological insulators. *Phys. World* **24**, 32 (2011).
- [95] M. König *et al.*; Quantum spin Hall insulator state in HgTe quantum wells. *Science* **318**, 766-770 (2007).
- [96] J.E. Moore & L. Balents; Topological invariants of time-reversal-invariant band structures. *Phys. Rev. B* **75**, 121306(R) (2007).
- [97] P. McClarty; Topological magnons: A review. arXiv:2106.01430v1 (2021).
- [98] S. Parkin *et al.*; Magnetically engineered spintronic sensors and memory. *Proc. IEEE* **91**, 661 (2003).
- [99] A. V. Chumak *et al.*; Magnon spintronics. *Nat. Phys.* **11**, 453 (2015).
- [100] X.S. Wang, H.W. Zhang & X.R. Wang; Topological magnonics: A paradigm for spin-wave manipulation and device design. *Phys. Rev. Applied* **9**, 024029 (2018).
- [101] A. Mook, J. Henk & I. Mertig; Edge states in topological magnon insulators. *Phys. Rev. B* **90**, 024412 (2014).
- [102] A. Mook *et al.*; Interaction-stabilized topological magnon insulator in ferromagnets. *Phys. Rev. X* **11**, 021061 (2021).
- [103] Y. Onose *et al.*; Observation of the magnon Hall effect. *Science* **329**, 297 (2010).
- [104] L. Zhang *et al.*; Topological magnon insulator in insulating ferromagnet. *Phys. Rev. B* **87**, 144101 (2013).
-

-
- [105] T. Moriya; Anisotropic superexchange interaction and weak ferromagnetism. *Phys. Rev.* **120**, 91 (1960).
- [106] R. Shindou *et al.*; Chiral spin-wave edge mode in dipolar magnetic thin films. *Phys. Rev. B* **87**, 174402 (2013).
- [107] K. Shen; Magnon spin relaxation and spin Hall effect due to the dipolar interaction in antiferromagnetic insulators. *Phys. Rev. Lett.* **124**, 077201 (2020).
- [108] E. Mengotti *et al.*; Real-space observation of emergent magnetic monopoles and associated Dirac strings in artificial kagome spin ice. *Nat. Phys.* **7**, 68-74 (2011).
- [109] J. Liu, L. Wang & K. Shen; Spin-orbit coupling and linear crossings of dipolar magnons in van der Waals antiferromagnets. *Phys. Rev. B* **102**, 144416 (2020).
- [110] J. Liu, L. Wang & K. Shen; Dipolar spin waves in uniaxial easy-axis antiferromagnets: A natural topological nodal-line semimetal. *Phys. Rev. Research* **2**, 023282 (2020).
- [111] C. Wessler *et al.*; Dipolar spin-waves and tunable band gap at the Dirac points in the 2D magnet ErBr₃. in preparation (2022).
- [112] J.M Kosterlitz; The critical properties of the two-dimensional xy model. *J. Phys. C: Solid State Phys.* **7**, 1046 (1974).
- [113] S.A. Solla & E.K. Riedel; Vortex excitations and specific heat of the planar model in two dimensions. *Phys. Rev. B* **11**, 6008 (1981).
- [114] F.G. Mertens *et al.*; Dynamical correlations from mobile vortices in two-dimensional easy-plane ferromagnets. *Phys. Rev. B* **39**, 591-602 (1989).
- [115] A.R. Völkel *et al.*; Dynamic correlations in the classical two-dimensional antiferromagnetic Heisenberg model with easy-plane symmetry. *Phys. Rev. B* **44**, 10066-10078 (1991).
- [116] K. de Bell *et al.*; Dipolar-induced planar anisotropy in ultrathin magnetic films. *Phys. Rev. B* **22**, 55 (1997).
- [117] S. Prakash & C.L. Henley; Ordering due to disorder in dipolar magnets on two-dimensional lattices. *Phys. Rev. B* **10**, 6574 (1990).
- [118] T.O. Wehling, A.M. Black-Schaffer & A.V. Balatsky; Dirac materials. *Adv. Physics* **63**, 1 (2014).
- [119] J. Fransson, A.M. Black-Schaffer & A.V. Balatsky; Magnon Dirac materials. *Phys. Rev. B* **94**, 075401 (2016).
- [120] D. Boyko, A.V. Balatsky, & J.T. Haraldsen; Evolution of magnetic Dirac bosons in a honeycomb lattice. *Phys. Rev. B* **97**, 014433 (2018).
- [121] T. Fukui, Y. Hatsugai & H. Suzuki; Chern numbers in discretized Brillouin zone: Efficient method of computing (spin) Hall conductances. *J. Phys. Soc. Jpn.* **74**, 1674 (2005).
-

-
- [122] K. Li *et al.*; Dirac and nodal line magnons in three-dimensional antiferromagnets. *Phys. Rev. Lett.* **119**, 247202 (2017).
- [123] S. Bao *et al.*; Discovery of coexisting Dirac and triply degenerate magnons in a three-dimensional antiferromagnet. *Nat. Commun.* **9**, 2591 (2018).
- [124] W. Yao *et al.*; Topological spin excitations in a three-dimensional antiferromagnet. *Nat. Phys.* **14**, 1011 (2018).
- [125] L. Chen *et al.* Topological spin excitations in honeycomb ferromagnet CrI₃. *Phys. Rev. X* **8**, 041028 (2018).
- [126] D. Xiao, W. Yao & Q. Niu; Valley-contrasting physics in graphene: magnetic moment and topological transport. *Phys. Rev. Lett.* **99**, 236809 (2007) .
- [127] W. Yao, S.A. Yang & Q. Niu; Edge states in graphene: From gapped flat-band to gapless chiral modes. *Phys. Rev. Lett.* **102**, 096801 (2009).
- [128] K. Qian *et al.*; Topology of the valley-Chern effect. *Phys. Rev. B* **98**, 2469 (2018).
- [129] D. Ghader; Valley-polarized domain wall magnons in 2D ferromagnetic bilayers. *Scientific Reports* **10**, 16733 (2020).
- [130] X. Zhai & Y.M. Blanter; Topological valley transport of gapped Dirac magnons in bilayer ferromagnetic insulators *Phys. Rev. B* **102**, 075407 (2020).
- [131] A. Mook, J. Henk & I. Mertig; Topologically nontrivial magnons at an interface of two kagome ferromagnets. *Phys. Rev. B*, **91**, 224411 (2015).
- [132] J.V. José *et al.*; Renormalization, vortices and symmetry-breaking perturbations in the two-dimensional planar model. *Phys. Rev. B* **3**, 1217 (1977).
- [133] R. Streubel *et al.*; Spatial and temporal correlations of XY macro spins. *Nano Lett.* **18**, 12, 7428-7434 (2018).
- [134] B. Lenk *et al.*; The building blocks of magnonics. *Physics Reports* **507**, 107-136 (2011).
- [135] G. Meyer; *Synthesis of lanthanide and actinide compounds*. Kluwer Academic Publishers, (1991).
- [136] J.P. Dowling & G.J. Milburn; Quantum technology: the second quantum revolution. *Phil. Trans. R. Soc. Lond. A* **361**, 1665-1674 (2003).
- [137] A.Y. Kitaev; Fault-tolerant quantum computation by anyons. *Ann. Phys* **303**, 2-30 (2003).
- [138] J.B. Fouet, P. Sindzingre & C. Lhuillier; An investigation of the quantum $J_1 - J_2 - J_3$ model on the honeycomb lattice. *Eur. Phys. J. B* **20**, 241-254 (2001).
- [139] A. Mulder, R. Ganesh, L. Capriotti & A. Paramekanti; Spiral order by disorder and lattice nematic order in a frustrated Heisenberg antiferromagnet on the honeycomb lattice. *Phys. Rev. B* **81**, 214419 (2010).
-

-
- [140] J. Merino & A. Ralko; Role of quantum fluctuations on spin liquids and ordered phases in the Heisenberg model on the honeycomb lattice. *Phys. Rev. B* **97**, 205112 (2018).
- [141] F. Wang; Schwinger boson mean field theories of spin liquid states on a honeycomb lattice: Projective symmetry group analysis and critical field theory. *Phys. Rev. B* **82**, 024419 (2010).
- [142] A.F. Albuquerque *et al.*; Phase diagram of a frustrated quantum antiferromagnet on the honeycomb lattice: Magnetic order versus valence-bond crystal formation. *Phys. Rev. B* **84**, 024406 (2011).
- [143] R. Ganesh *et al.*; Plaquette resonating valence bond state in a frustrated honeycomb antiferromagnet. *Phys. Rev. B* **87**, 054413 (2013).
- [144] F. Ferrari & F. Becca; Dynamical properties of Néel and valence-bond phases in the $J_1 - J_2$ model on the honeycomb lattice. *J. Condens. Matter Phys.* **32**, 274003 (2020).
- [145] T. Senthil *et al.*; Deconfined quantum critical points. *Science* **303**, 1490-1494 (2004).
- [146] R. Ganesh, J. van den Brink & S. Nishimoto; Deconfined criticality in the frustrated Heisenberg Hamiltonian honeycomb antiferromagnet. *Phys. Rev. Lett.* **110**, 127203 (2013).
- [147] N. Tsyrlin *et al.*; Quantum effects in a weakly frustrated $S = 1/2$ two-dimensional Heisenberg antiferromagnet in an applied magnetic field. *Phys. Rev. Lett.* **102**, 197201 (2009).
- [148] P.W. Anderson *et al.*; The physics behind high-temperature superconducting cuprates: the 'plain vanilla' version of RVB. *J. Phys.: Condens. Matter* **16**, R755-R769 (2004).
- [149] D.A. Tennant, T.G. Perring, R.A. Cowley & S.E. Nagler; Unbound spinons in the $S = 1/2$ antiferromagnetic chain KCuF_3 . *Phys. Rev. Lett.* **70**, 4003-4006 (1993).
- [150] D.C. Dender *et al.*; Direct observation of field-induced incommensurate fluctuations in a one-dimensional $S = 1/2$ antiferromagnet. *Phys. Rev. Lett.* **79**, 1750-1753 (1997).
- [151] P. Mendels & F. Bert; Quantum kagome frustrated antiferromagnets: One route to quantum spin liquids. *C. R. Physique* **17**, 455-470 (2016).
- [152] Y. Shimizu, K. Miyagawa, K. Kanoda, M. Maesato & G. Saito; Spin liquid state in an organic Mott insulator with a triangular lattice. *Phys. Rev. Lett.* **91**, 107001 (2003).
- [153] J. Villain; Insulating spin glasses. *Z. Physik B* **33**, 31-42 (1979).
- [154] B. Canals & C. Lacroix; Pyrochlore antiferromagnet: A three-dimensional spin liquid. *Phys. Rev. Lett.* **80**, 2933-2936 (1998).
-

-
- [155] Y. Singh *et al.*; Relevance of the Heisenberg-Kitaev model for the honeycomb lattice iridates $A_3\text{IrO}_3$. *Phys. Rev. Lett.* **108**, 127203 (2012).
- [156] K. Kitagawa *et al.*; A spin-orbital-entangled quantum liquid on a honeycomb lattice. *Nature* **554**, 341-345 (2018).
- [157] C. Wessler *et al.*; Observation of plaquette fluctuations in the spin-1/2 honeycomb lattice. *npj Quant. Mater.* **5**, 85 (2020).
- [158] T. Weber, R. Georgii & P. Böni; Takin: An open-source software for experiment planning, visualization, and data analysis. *SoftwareX* **5**, 121-126 (2016).
- [159] M.E. Zhitomirsky & A.L. Chernyshev; Colloquium: Spontaneous magnon decays. *Rev. Mod. Phys.* **85**, 219-243 (2013).
- [160] G. Sala *et al.*; Van Hove singularity in the magnon spectrum of the antiferromagnetic quantum honeycomb lattice. *Nature Communications* **12**, 17 (2021).
- [161] A. Mattsson *et al.*; Frustrated honeycomb Heisenberg antiferromagnet: A Schwinger-Boson approach. *Phys. Rev. B* **49**, 3997 (1994).
- [162] R.S. Lapa & A.S.T. Pires; Critical properties of the frustrated quasi-two dimensional XY-like antiferromagnet. *JMMM* **327**, 1-6 (2013).
- [163] A.S.T Pires; Quantum phase transition in the frustrated anisotropic honeycomb lattice. *Physica B* **4791**, 130-133 (2015).
- [164] E. Ghorbani, F. Shahbazi & H. Mosadeq; Quantum phase diagram of distorted J_1 - J_2 Heisenberg $S=1/2$ antiferromagnet in honeycomb lattice: a modified spin-wave study. *J. Phys.: Con. Mat.* **9**, 406001 (2016).
- [165] D.P. Avros & A. Auerbach; Functional integral theories of low-dimensional quantum Heisenberg models. *Phys. Rev. B* **38**, 316-333 (1988).
- [166] M. Takahashi; Modified spin-wave theory of a square-lattice antiferromagnet. *Phys. Rev. B* **4**, 2494 (1989).
- [167] F. Ferrari, S. Bieri & F. Becca; Competition between spin liquids and valence-bond order in the frustrated spin-1/2 Heisenberg model on the honeycomb lattice. *Phys. Rev. B* **96**, 104401 (2017).
- [168] S. Chakravarty, B.I. Halperin & D.R. Nelson; Low-temperature behavior of two-dimensional quantum antiferromagnets. *Phys. Rev. Lett.* **11**, 1057-1060 (1988).
- [169] R.F. Bishop *et al.*; Valence-bond crystalline order in the $s = 1/2$ J_1 - J_2 model on the honeycomb lattice. *J. Phys.: Condens. Matter* **25**, 306002 (2013).
- [170] P.A. Maksimov & A.L. Chernyshev; Field-induced dynamical properties of the XXZ model on a honeycomb lattice. *Phys. Rev. B* **93**, 014418 (2016).
- [171] J. Zheng *et al.*; Gapless spin excitations in the field-induced quantum spin liquid phase of α - RuCl_3 . *Phys. Rev. Lett.* **119**, 227208 (2017).
-

-
- [172] A. Banerjee *et al.*; Excitations on the field-induced quantum spin liquid state of α - RuCl_3 . *npj Quant. Mater.* **3**, 8 (2018).
- [173] K.F. Mak, J. Shan & D.C. Ralph; Probing and controlling magnetic states in 2D layered magnetic materials. *Nature Reviews Physics* **1**, 646–661 (2019).
- [174] B. Huang *et al.*; Layer- dependent ferromagnetism in a van der Waals crystal down to the monolayer limit. *Nature* **546**, 270–273 (2017).
- [175] D.R. Klein *et al.*; Probing magnetism in 2D van der Waals crystalline insulators via electron tunneling. *Science* **360**, 1218–1222 (2018).
- [176] G. Meyer; *Advances in the synthesis and reactivity of solids*. **2**, 1-26 (Elsevier science & technology, Oxford, 1994).
- [177] H. Schober; Neutron scattering instrumentation, in *Neutron Applications in Earth, Energy and Environmental Sciences*, Springer, US: Boston, 37-104(2009).
- [178] F. Pobell; *Matter and methods at low temperatures*. Springer, Berlin, Heidelberg (2007).
- [179] M.J. Cooper & R. Nathans; The resolution function in neutron diffractometry. *Acta Cryst.* **23**, 357 (1967).
- [180] M. Popovici; On the resolution of slow-neutron spectrometers. *Acta Cryst.* **31**, 507 (1975).
- [181] G. Eckold & O.Sobolev; Analytical approach to the 4D-resolution function of three axes neutron spectrometers with focussing monochromators and analysers. *Nuclear Instruments and Methods in Physics Research Section A* **752**, 54-64 (2014).
- [182] E.C. Titchmarsh; *Introduction to theory of Fourier integrals*, Oxford University Press (1948).
- [183] L. Bonsall & A.A. Maradudin; Some static and dynamical properties of a two-dimensional Wigner crystal. *Phys. Rev. B*, **15**, 4 (1977).
- [184] T. Holstein & H. Primakoff; Field dependence of the intrinsic domain magnetization of a ferromagnet. *Phys. Rev.* **58**, 1098 (1940).
- [185] M. Aidelsburger; *Artificial gauge fields with ultracold atoms in optical lattices*. Phd-thesis, Fakultät für Physik, Ludwig-Maximilians-Universität München (2014).
- [186] P. Thalmeier; Low-energy Nd spin waves in noncollinear Nd_2CuO_4 . *Physica C* **266**, 89-103 (1996).
-